# Oxygen Concentration Microgradients for Cell Culture

Jaehyun Park

Electrical Engineering and Computer Sciences
University of California at Berkeley

May 14, 2010

Oxygen Concentration Microgradients for Cell Culture

By

Jaehyun Park

A dissertation submitted in partial satisfaction of the
requirements for the degree of

Doctor of Philosophy

in

Engineering-Electrical Engineering and Computer Sciences

in the

Graduate Division

of the

University of California, Berkeley

Committee in charge:

Professor Michel M. Maharbiz, Chair
Professor Ming C. Wu
Professor Amy E. Herr

Spring 2010

Abstract

Oxygen Concentration Microgradients for Cell Culture

by

Jaehyun Park

Doctor of Philosophy in Electrical Engineering and Computer Science

University of California, Berkeley

Professor Michel M. Maharbiz

There is a growing need for technology that can control microscale oxygen gradients onto a tissue or culture sample *in vitro*. This dissertation introduces the oxygen microgradient chip (OMA), which employs electrolysis to generate oxygen microgradients within cell culture without forming bubbles. Dissolved oxygen generated at noble microelectrodes patterned on a chip surface diffuses through a gas-permeable silicone membrane and is dosed into cell culture. The amount of generated oxygen is directly proportional to a current flowing across the electrodes and thus can be controlled with high precision. By real-time modulation of the current, spatial profile of the oxygen concentration microgradient can be modified during an experiment. Distinct microgradients generated by different electrodes can be superimposed to pattern arbitrary and multi-dimensional oxygen concentration profiles with microscale resolution. Design of the OMA is based on simulation results of diffusion and physical considerations. Microfabrication, assembly process, and improvements of the early OMA are presented. Use of an oxygen-sensitive fluorophore film verifies that the measured microgradients in OMA match simulation results. Generation of reactive oxygen species during the electrolysis is also

considered and quantified. This technology enables the biological study of gradient-related effects. Three different, well-known biological models are introduced to demonstrate how the microtechnology enables new types of experiments. Lastly, we explore the effect of oxygen gradients on muscle progenitor cells having half-deficiency of superoxide dismutase-1 (SOD1) enzyme. Another type of oxygen gradient chip that utilizes atmospheric oxygen is developed and used in this experiment. Myotube formation of the SOD1 heterozygote myoblasts decreased significantly compared to that of wild-type myoblasts, indicating that the oxygen stress on SOD1 heterozygote myoblasts induces defective cellular function on differentiation.

부모님께...

To my parents…

Table of Contents

Chapter 3

Chapter 4

Chapter 5

List of Figures

List of Tables

List of Abbreviations

ALS   : Amyotrophic lateral sclerosis

ATP   : Adenosine triphosphate

bFGF   : Basic Fibroblast growth factor

BHF   : Buffered hydrofluoric acid

BSA   : Bovine serum albumin

DAPI   : 4'-6-diamidino-2-phenylindole

DHET : Dihydroethidium

DM   : Differentiation medium

DMEM : Dulbecco's modified Eagle medium

DP   : Differentiation potential

DRIE   : Deep reactive ion etching

ECL   : Entactin-collagen-laminin

FBS   : Fetal bovine serum

FI   : Fusion index

GM   : Growth medium

GPX   : Glutathione peroxidase

Hif   : Hypoxia inducible factor

HMDS : Hexamethyldisilazane

HRP   : Horseradish peroxidase

ITO   : Indium tin oxide

LB   : Luria-Betani

MHC   : Myosin heavy chain

NADP   : Nicotinamide adenine dinucleotide phosphate

OMA   : Oxygen microgradient array

PBS   : Phosphate-buffered saline

PCB   : Printed circuit board

PDMS   : Polydimethylsiloxane

ROS   : Reactive oxygen species

SOD   : Superoxide dismutase

Acknowledgements

Chapter 1

Introduction

1.1 Oxygen in Life

The human body is composed of 65% oxygen along with carbon (18%), hydrogen (10%), nitrogen (3%), and calcium (1.5%). Most of the oxygen in the human body is found as water, H_2O, consisting $65 - 90\%$ of cells [1]. It is molecular oxygen, O_2, which plays one of the most important roles in the metabolic energy transfer of the aerobic living organisms in the Earth.

Most land animals, including mammals, uptake oxygen from ambient air through specialized organs called lungs. During respiration, air passes into finer tubes called bronchioles and reaches a cluster of tiny air sacs called alveoli, where gas exchange occurs. Oxygen in the air entering alveoli dissolves through a membrane into blood vessels surrounding each alveolus, and then is transferred to tissues and organs by cardio-vascular system [2].

Dissolved oxygen is used by cells and tissues in most multi-cellular species for the oxidation of molecules during processes such as new tissue development, energy conversion from food, and disposal of by-products. Most importantly, oxygen is used in the electron transfer oxidase

system where it helps form phosphate bonds in ATP. Animals, especially mammals, critically depend on the continuous supply of oxygen for life. In humans, apnea for more than one minute occurs serious lack of oxygen in blood vessel, three minutes discontinuance of oxygen supply leads to permanent damage to brain. Therefore, molecular oxygen is a critical requirement for cellular function and aerobic metabolism is an essential process.

This chapter begins with the importance of oxygen concentration microgradients in tissue and culture. After describing the need for the ability to generate oxygen concentration microgradients in the laboratory, an overview of recent efforts to generate microgradients will be introduced.

1.2 Biological Microgradients

Biological microgradients are essential mechanisms in organism development in our body. On a cellular level, the potential energy harnessed by concentration gradients is a common motif [2][3]. While active transport utilizes ATP energy to power membrane pumps, the simplest transport method uses the potential energy inherent in a gradient, or spatial difference in concentration, a process called diffusion. Gases and small polar molecules such as water and ethanol are transported across cellular membrane by the principle of diffusion. These gradients can often be exploited as signals in tissues.

Chemokines and their receptors are a relevant example. During the wound-healing process, it is known that gradient of chemokines attract neutrophils and other leucocytes to the wound site. Chemokines are chemotactic cytokines having $8 - 10$ kilodalton size, and their structures and functions are defined by four conserved cysteine residues. These proteins activate neutrophil receptors and guide the migration of cells through the protein concentration gradient. Some homeostatic chemokines are involved in the immune system to localize T or B cells with antigen.

Other inflammatory chemokines generated by infected or damaged cells induce migration of leukocytes to the injured or infected site, or activate the cells to mount an immune response and initiate wound healing [4].

Chemical gradients have long been suspected to play a role in many developmental processes. Numerous patterns of skin on animals, such as our fingerprints or stripes on a zebrafish, can be explained as a result of chemical gradients generated by chemical reactions and diffusion at work doing developmental processes. A canonical example is the two-component reaction-diffusion system developed by Alan Turing in his seminal paper [5]. This mathematical model describes a chemical system that can generate chemical gradients spontaneously in the process of chemical noise. The elucidation of Turing mechanism in nature is an active area of research [6].

Tissue oxygenation and the intracellular machinery that responds to oxygen environments play critical roles in many human diseases including cancer, heart disease, stroke, arthritis, wound healing, and pulmonary disease [7][8][9][10]. Oxygen levels are known to affect cell's fate determination and induce angiogenesis via the pathway of Hif-1α, a transcription factor generated at low oxygen concentrations [10]. The importance on role of oxygen gradients has been increasingly recognized in development processes, regeneration and patterning of tissues, modulation of apoptosis and myofiber formation in myoblasts as well as stem cell migration [11]. Therefore, the generation and control of oxygen microgradients *in vitro* would allow the study one of nature's micro-patterning techniques and would be a powerful tool in understanding biological development and disease.

1.3 Oxygen Environment *in Vitro*

The delivery of precise and localized oxygen into tissues and organs is a recurring problem in

the engineering of *in vitro* culture systems. Oxygen levels in tissue are maintained by elaborate, highly conserved intracellular and organ-level feedback loops, since oxygen homeostasis is essential for normal cellular functioning. Average oxygen concentration at the tissue level in adults is about 3% (1.16 ppm). In contrast, atmospheric oxygen content is 20%. Despite the fundamental importance of a precisely regulated oxygen environment, virtually all the cell cultures are performed in 20% oxygen after isolation of cells from a living tissue because of its convenience (room air with 5% CO_2 results in 20% O_2 with 5% CO_2), historical precedence, and most critically, the lack of suitable methods to accurately vary the oxygen environment around cultured cells.

Monolayer culture has been used in most of *in vitro* experiments due to ease of growth. Ideally, one would like to measure and control oxygen levels *in vivo*. However these gradients are difficult to study because 1) interstitial diffusion is not present in monolayer cultures; 2) oxygen measurement in animal models [12] and in humans [13][14] requires invasive procedures; and 3) sensing and controlling oxygenation in these cases is not possible. In many eukaryotic tissues, it is not yet clear whether cells are aware of gradients *per se* or merely react to the different micro-environmental conditions established by those gradients [15]. The ability to investigate the genetic and epigenetic responses of cells in a spatially and temporally controllable oxygen environment may have far reaching implications for the study of developmental processes.

1.4 Previous Work on Generation of Oxygen Microgradients

Several methods have been developed to examine the effect of diffusible chemical gradients across cells and tissues *in vitro*. Of these, the Boyden and Dunn chambers have arguably been the most influential [16][17]. Neither of these methods, however, is suitable for establishing

gradients of diffusible gases on monolayer culture. Jeon and co-workers adapted a microfluidic technique developed by Dertinger and co-workers to pattern chemoattractant gradients for neutrophil chemotaxis studies [18][19]. This elegant system relies on the concatenation of numerous low Reynolds number (laminar) flows containing non-gaseous chemical concentrations to construct one-dimensional gradients across certain spans of a microfluidic channel. The standard experimental method for studying oxygen microgradients in microbial cultures is the capillary assay [20][21][22][23][24][25]. In this assay, one end of a small glass capillary contains an air bubble and the other is loaded with the cells of interest. The bubble assay works similarly but employs a small gas bubble trapped between a glass slide and cover-slip. In both cases a microgradient is established by oxygen bubble trapped in glass capillaries or cover-slips (in part due to the oxygen consumption of the cells themselves); cell responses such as taxis towards or away from the oxygen source can thus be studied by changing the composition of the gas phase [22]. However, oxygen concentration profile near the gas-liquid interface is non-linear, and the non-linear profile cannot be modified during experiment.

More recent work demonstrated a microscale, flat-plate perfusion reactor used to establish an oxygen gradient across rat liver cells [26]; a decreasing gradient was established by flowing oxygenated medium across cells on a surface between a fluid inlet and outlet. The Takayama lab also established a microfluidic device with pumps and valves to generate oxygen concentration gradient and to measure cellular oxygen consumption [27]. In those cases, the oxygen concentration profile is determined by the micro-channel geometry and the continuous liquid flow rate, and the profile is limited to one-dimension.

Chapter 2

OMA Design and Simulation

2.1 Proposed Oxygen Microgradient Array (OMA)

To overcome the disadvantages of previous techniques stated in section 1.4, this thesis presents a device that uses microscale electrolysis to generate precise doses of dissolved oxygen. The ability for the proposed device to control oxygen levels across a cell culture with microscale precision should enable researchers to examine oxygen-dependent behavior across an entire range of oxygen levels of interest with single experiments. Various oxygen concentration profiles such as linear, triangular and round shape can be constructed with wide range of concentration level (0 % ~ 40 % dO_2) within 1 mm × 1 mm culture area. Moreover, the oxygen profile can be two-dimensional (2-D) since the microgradient is formed on a surface of PDMS membrane, not inside a microfluidic channel. Another principal advantage of the technology is the ability to rapidly generate and alter oxygen gradients during the course of an experiment. This enables the research on the response of living tissues or microbes experiencing rapid change of oxygenation. In this section, the principle of operation of the proposed oxygen microgradient array will be

introduced, describing how the advantages listed above can be realized.

The oxygen microgradient array (OMA), employs water electrolysis to generate controlled amounts of dissolved oxygen from an array of noble metal microelectrodes embedded in a silicone electrolyte channel. Figure 2.1 is a conceptual illustration and cross-section of the device. The OMA consists of an array of microelectrodes patterned onto a glass substrate within a PDMS silicone electrolyte channel. Each micro-patterned electrode acts as a source of aqueous, dissolved oxygen and the current through each of these microelectrodes is independently controlled. This electrolyte channel is filled with aqueous electrolyte. The 'roof' of the electrolyte channel acts as a membrane separating the electrolyte from the cell culture medium. The dissolved oxygen generated by an array of microelectrodes diffuses up through the thin PDMS membrane and into the tissue or cell culture under analysis. Oxygen generation rates are never high enough to generate gas bubbles. By superimposing different doses generated at different microelectrodes in the array, many different gradients can be patterned onto monolayer culture. Since the current through any of the electrodes can be altered at any time, oxygen dosage and gradient profiles can be changed or regulated. An oxygen-sensitive fluorophore film (also silicone-based and gas-permeable) allows for 2-D mapping of the oxygen gradient using fluorescent microscopy. Since both the substrate and the applied layers (with the exception of the metal electrodes) are transparent, the cells in the device can be visualized with upright or inverted microscopy. I believe this technique will enable a new class of bio-devices capable of imposing 1-D and 2-D microgradients on tissue.
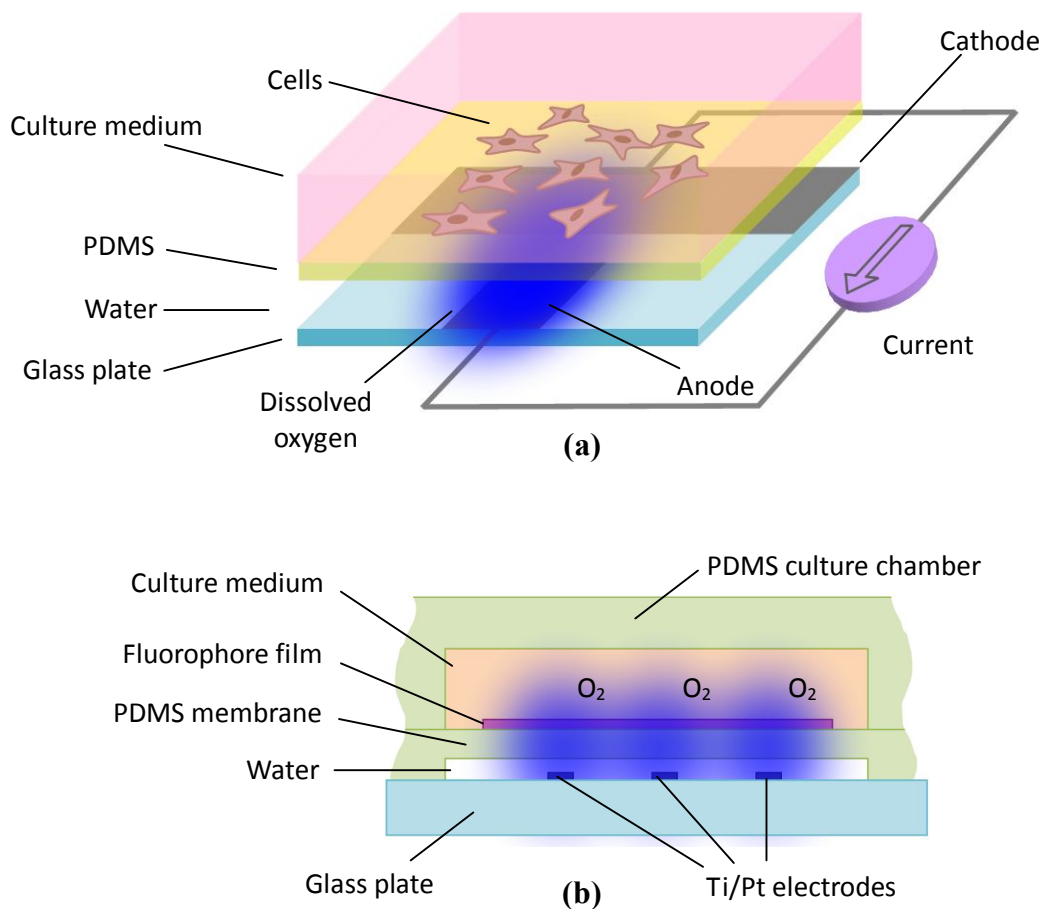
Figure 2.1 Basic concept of the oxygen microgradient array (OMA).

(a) 3-D illustration of operation. Note that blue cloud indicates dissolved oxygen, not bubbles. **(b)** Schematic cross-section of device. Oxygen generated at microelectrodes diffuses into the cell culture area. Each microelectrode in the array can be controlled independently. The fluorophore film is introduced when the oxygen microgradient profile is measured; it reports oxygen concentration and is imaged using upright microscopy.

It is important to stress that 1) the defined electrolyte (water) ensures oxygen generation, 2) the electrolyte and the cell medium are separated by a hydrophobic membrane and never come into contact, 3) the cells are not subject to significant electric fields since all the microelectrodes are coplanar and are separated from the cells by a liquid-impermeable membrane. These conditions help ensure that no toxic or unwanted by-products are generated at the microelectrode sites if operated within a well-defined applied potential. From the next section, detailed considerations on OMA design will be discussed with physical principles on electrolysis and diffusion, properties of PDMS, and simulations.

2.2 Electrolysis

Oxygen generation in OMA involves electrolysis of water. Electrolysis is a process of inducing a chemical reaction by applying electric current through an ionic liquid called electrolyte. In this section, the basic concepts of water electrolysis are presented. More details on concepts such as the half-cell, overpotential, and kinetics of potential across electrodes can be found in intermediate level chemistry textbooks [28].

2.2.1 Water Electrolysis

During the water electrolysis, the generation of oxygen (at the anode) and hydrogen (at the cathode) can be described by the following half reactions:

$$2\,H_2O \rightarrow O_2\,(g) + 4\,H^+\,(aq) + 4\,e^-\,(aq) \qquad E^{0a} = 1.23 \text{ V vs. SHE} \qquad (2.1)$$

$$4\,H_2O + 4\,e^-\,(aq) \rightarrow 2\,H_2\,(g) + 4\,OH^-\,(aq) \qquad E^{0c} = 0.83 \text{ V vs. SHE} \qquad (2.2)$$

The open circuit potentials of electrodes (E^{0a}, E^{0c}) can be calculated using Gibbs free energy as an electrolytic cell. Given reaction (2.1), it is evident that the amount of oxygen generated at the anode is directly proportional to the amount of current running between the anode and cathode; four electrons are required to generate one O_2 molecule. The oxygen dosed into the cell culture from the given microelectrode can thus be precisely controlled. It is important to note that these reactions are dominant only if the anode and cathode are well-separated and the electrolyte composition is carefully designed so as to eliminate competing reactions (e.g. the presence of Cl^- leads to competitive generation of chlorine from the anode, which is undesirable) [28]. A fraction of the current, for example, can lead to the generation of reactive oxygen species (see section 2.2.2). Assuming no such unwanted reactions, the relationship between applied current (i) and number of generated oxygen molecules ($e/4$) can be described as :

$$\frac{e}{4} \cdot \frac{q}{t} = i \quad [A] \tag{2.3}$$

Where e and q are number of electrons and elementary charge (1.6×10^{-19} C), respectively.

• **Electrolyte Reservoir**

Electrolyte reservoir is placed at one side of the OMA, and electrolyte channel needs to connect the reservoir and electrode array, while the PDMS membrane covers all the area of the array and channels. An open inlet can be made by cutting the membrane where the reservoir is placed.

Possible operation time could be limited by size of the electrolyte reservoir. Calculation

of reservoir size is based on 7 days of operation with maximum, possible values of parameters such as current density and electrode area. Oxygen molecules generated through electrode area A, during time t is :

$$m_{O_2} = \frac{j_{O_2} A t}{A_V} \quad \text{[mol]} \tag{2.4}$$

Where j_{O_2} is flux of oxygen molecules (molecules/mm^{2}s) and A_V is Avogadro's number (6.02×10^{23} mol^{-1}). Two H_2O molecules are required to generate one O_2 molecule, and molecular mass of H_2O is 18 g when water is used as electrolyte. Assuming that j_{O_2} is 10 times larger than the oxygen flux (1.65×10^{14} molecules/mm^{2}s) in section 2.5.2 and the entire design area (1 mm × 1 mm) is covered with electrode, total volume of water consumed by the electrolysis is 5.97 μL for 7 days of operation. This tiny volume does not make problem for reservoir size because the reservoir of fabricated OMA (in section 3.1.5) can hold 70 μL of water. However, water evaporation from the reservoir needs to be considered. The evaporation depends on humidity and temperature around the OMA. For example, continuous purging of the OMA in a gas control chamber with 95% N_2 and 5% CO_2 in 37 °C resulted in complete depletion of the 70 μL in reservoir within 12 hours. This limited operation time was enhanced by covering the top with a molded silicone piece, which was able to hold the water up to 3 days in the same condition. Moreover, operation can stay indefinite if the reservoir is refilled.

• Cathode Placement

Water electrolysis involves generation of hydrogen from cathode, which is proportional to current density on electrode surface, as shown in reaction (2.2). The effects of hydrogen to the cell culture can be neglected for several reasons. First, the cathode can be placed far (2 mm to 15 mm) from the 1 mm × 1 mm microgradient area. Second, cathode area is much larger than anode area in order to reduce the cathodic current density. The area of the on-chip cathode (18 mm × 1 mm) is at least 200× larger than anode areas (varied, e.g. 20 μm × 1 mm). The reduced current density on cathode eliminates possibility of localized high hydrogen flux which may affect the cell culture area near the cathode. Last, hydrogen diffuses faster than oxygen (diffusion coefficient of hydrogen in water : 4.5×10^{-3} mm^2/s [29]).

2.2.2 Reactive Oxygen Species Generation

Reactive oxygen species (ROS) are undesirable but possible by-products from the water electrolysis. Quantification of ROS is important since ROS are known to affect cell and tissue culture (see section 4.2.1). The ROS that concern us are ozone, hydrogen peroxide, hydroxyl radical, superoxide radical and singlet oxygen (Figure 4.4). Electrolytic ozone production has known to be strongly dependent on temperature and electrolyte composition [30][31][32]. Foller and Tobias performed the most comprehensive study of ozone generation at platinum (Pt) electrodes in aqueous electrolyte; possible competing reactions are [33]:

$$3\ H_2O \rightarrow O_3 + 6\ H^+ + 6\ e^- \qquad\qquad |E^{0a}| = 1.51\ \text{V vs. SHE} \qquad\qquad (2.5)$$

$$H_2O + O_2 \rightarrow O_3 + 2\,H^+ + 2\,e^- \qquad\qquad |E^{0a}| = 2.07\ \text{V vs. SHE} \qquad\qquad (2.6)$$

At the current densities employed in our device (≤ 1 mA/mm^2), this study found that polished Pt electrodes had ozone generation rates less than 0.1% of the total current in highly conductive electrolytes (5 M H_2SO_4) at low temperatures (0 °C) and the generation rates dropped precipitously with decreasing electrolyte concentrations and increasing temperature. Maharbiz *et al.* detected ~ 4ppb of ozone, which is close to the resolution limit of sensor, with applying 4 V (~ 20 mA/mm^2 of current density) into 0.1 M phosphate buffer electrolyte at room temperature [34]. Based on these data, it is highly unlikely that any ozone is produced or enters the cell culture area since our device employed pure water as an electrolyte and operated between 25 – 37 °C with much lower current. However, methods to measure tiny amount of produced ozone from the electrolysis of pure water needs to be developed for future iterations.

Hydroxyl ions (OH^-) are constantly generated at the cathode and as part of side reactions occurring near the anode, but these recombine quickly (1 nsec of half-life) and cannot diffuse through the hydrophobic membrane [35]. Singlet oxygen (O^-) and superoxide radical (O_2^-) are both strong oxidizers, but they have half-lives of $2 - 500$ μsec and 1 nsec, respectively [36]; additionally, their high half-cell potentials, make even more unlikely than ozone to be produced.

Conversely, hydrogen peroxide is readily produced by the reduction of oxygen at either a heavily basic (pH > 11) or an acidic (pH < 5) cathode [37]:

$$O_2 + 2\,H^+ + 2\,e^- \rightarrow H_2O_2 \qquad\qquad |E^0| = 0.682\ \text{V vs. SHE} \qquad\qquad (2.7)$$

$$2\ H_2O \rightarrow H_2O_2 + 2\ H^+ + 2\ e^- \qquad\qquad |E^0| = 1.776\ \text{V vs. SHE} \qquad\qquad (2.8)$$

This could occur only if oxygen diffused to the cathode is reduced to hydrogen peroxide and then the peroxide diffuses back towards the culture area. As part of the qualification of the OMA, we employed a standard colorimetric indicator for the hydrogen peroxide detection. For measurements and more discussions of the peroxide generation in OMA, refer to section 3.7.3.

2.3 Diffusion

Dissolved oxygen and hydrogen generated by electrolysis in the OMA passes through multiple layers (electrolyte channel, PDMS membrane, and culture medium) via diffusion [38]. Fick's first law describes the relationship between a concentration gradient and the flux of molecules in steady state:

$$J = -D\nabla C \tag{2.9}$$

Where J, D and C are diffusive flux (molecules/mm^{2}s), diffusion coefficient (mm^2/s) and concentration (molecules/mm^3), respectively. The minus sign means the flux proceeds from high to low concentration. In the OMA, oxygen microgradients were designed with an assumption that the generated microgradient reaches saturated, steady state. Therefore Fick's first law is governing equation for analysis and simulation of the microgradients.

Fick's second law derived from equation (2.9) explains how the diffusion proceeds with time. This describes transient state of oxygen diffusion and was used for the estimation of saturation time of the generated microgradient. Assuming diffusion coefficient is constant, the second law

is expressed as :

$$\frac{\partial C}{\partial t} = D\nabla^2 C$$

(2.10)

This second law is coupled with Michaelis-Menten kinetics for simulating the hydrogen peroxide - Amplex Red system to obtain estimates of hydrogen peroxide generation (see section 3.7.3).
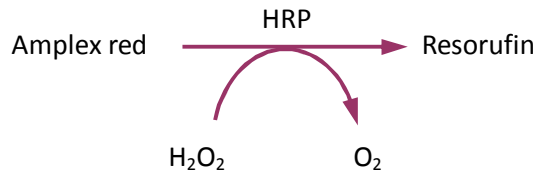
Figure 2.2 Catalytic generation of resorufin by horseradish peroxidase.

The generation of fluorescent resorufin by the HRP enzyme (Figure 2.2) was modeled by including Michaelis-Menten kinetics in the diffusion equation (2.9) in the cell culture domain.

$$D_{H_2O_2}\nabla^2\mathbf{C}_{H_2O_2} = \frac{\partial \mathbf{C}_{H_2O_2}}{\partial t} - \frac{V_{\max}[\mathbf{C}_{H_2O_2}]}{K_m + [\mathbf{C}_{H_2O_2}]}$$

(2.11)

$$D_{reso}\nabla^2\mathbf{C}_{reso} = \frac{\partial \mathbf{C}_{reso}}{\partial t} + \frac{V_{\max}[\mathbf{C}_{H_2O_2}]}{K_m + [\mathbf{C}_{H_2O_2}]}$$

(2.12)

A $V_{\max} = 1.9$ mM/min and $K_m = 1.55$ mM were used for the horseradish peroxidase enzyme [39][40]. This modeled the fact that the hydrogen peroxide concentration in the cell culture

chamber was determined not just by simple diffusion, but also by reaction with the Amplex Red enzymatic system.

2.4 Properties of PDMS

Elastic silicone rubber has been widely used in biological applications and microfluidics due to advantages of bio-compatibility, low-cost and ease of fabrication [41][42][43]. Silicon-based organic polymer is characterized by functional groups attached on silicon-oxygen backbone and it consists of repeating monomers cross-linked by siloxanes as in Figure 2.3.

$$
\left[\begin{array}{c} CH_3 \\ | \\ Si-O \\ | \\ CH_3 \end{array}\right]_n
$$
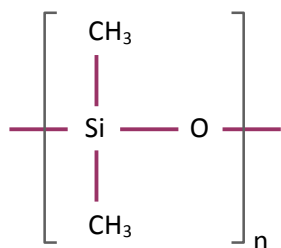
Figure 2.3 Chemical structure of PDMS.

n is repeating number of monomers, $SiO(CH_3)_2$, linked by siloxanes.

Polydimethylsiloxane (PDMS) is one of the most common silicone polymers and used as a gas-permeable membrane between the two liquid layers of electrolyte channel and cell culture area in OMA. Advantages of PDMS, which made the OMA possible to operate as desired, will be discussed in this section as well as disadvantages to be overcome or to reduce mal-effects to cell culture.

2.4.1 Transparency

Almost no optical loss exists in PDMS between 400 – 1000 nm wavelength of light, covering the range of visible wavelength to the human eye (400 – 700 nm) [44]. This high-transparency allows many microfluidic devices, including the devices in section 1.4, to image the fluidic channels inside PDMS easily. It is also required for the OMA since inverted microscopy is used for observation of cell culture by imaging through a glass substrate and PDMS membrane.

2.4.2 Bio-Compatibility

Avoiding cellular toxicity or adverse cell response is an issue with most instrumentation intended to work with cells [45][46]. Despite sometimes treated as a bio-compatible material in numerous application [47], PDMS has been reported the toxicity of its uncross-linked monomers [48]. Additionally, the PDMS surface needs to be functionalized to enhance cell adhesion in many cell types. Research on proper coating matrix to a specific cell type and optimization of the coating process is required. In this work, adhesion of myoblast cell was optimized with various coating matrices prior to loading them into the OMA.

• **Coating Matrix on PDMS**

Growth of various cell types on PDMS has previously been investigated [49][50], but optimal coating matrix depends on each cell type. Several coating materials were tested for differentiation of wild-type myoblasts to find out the best coating material. PDMS (Sylgard 184, Dow Corning) was prepared with 10:1 ratio of base and curing agent, and was then spun onto 0.5 mm thick glass substrate and cured on 100 °C hot plate for 20 minutes. The

PDMS coated glass was diced into 1.5 cm × 1 cm, then mounted on 60 mm dish with a mounting medium (Permount, SP15-100, Fisher Scientific). PDMS samples and control dishes were prepared as duplicate for each coating matrix.

After UV sterilization of the samples for 1 hour, surface was treated with four different cell matrices (Table 2.1); ECL (ECL Cell Attachment Matrix, 08-110, Millipore), fibronectin (F-1141, Sigma-Aldrich), gelatin (Gelatin 2%, G1393, Sigma-Aldrich) and collagen stock (section 4.2.5). Wild-type myoblasts were seeded in GM with density of 1×10^4 cells/cm^2, and grown for 2 days. Culture medium was switched to DM and differentiation was induced for 5 days. After MF20 staining (see section 4.3.2), images were taken as in Figure 2.4.

Table 2.1 Process conditions of four different surface coating matrices.

	Diluted concentration	Incubation time	Incubation temperature	Surface dry after coating
Collagen	0.1 mg/mL in 0.1N acetic acid + QH$_2$O	24 hours	37 °C	Yes
ECL	20 µg/mL in serum-free medium (DMEM)	1 hour	37 °C	No
Gelatin	0.1% in QH$_2$O	24 hours	37 °C	No
Fibronectin	10 µg/mL in PBS	1 hour	Room temperature	Yes
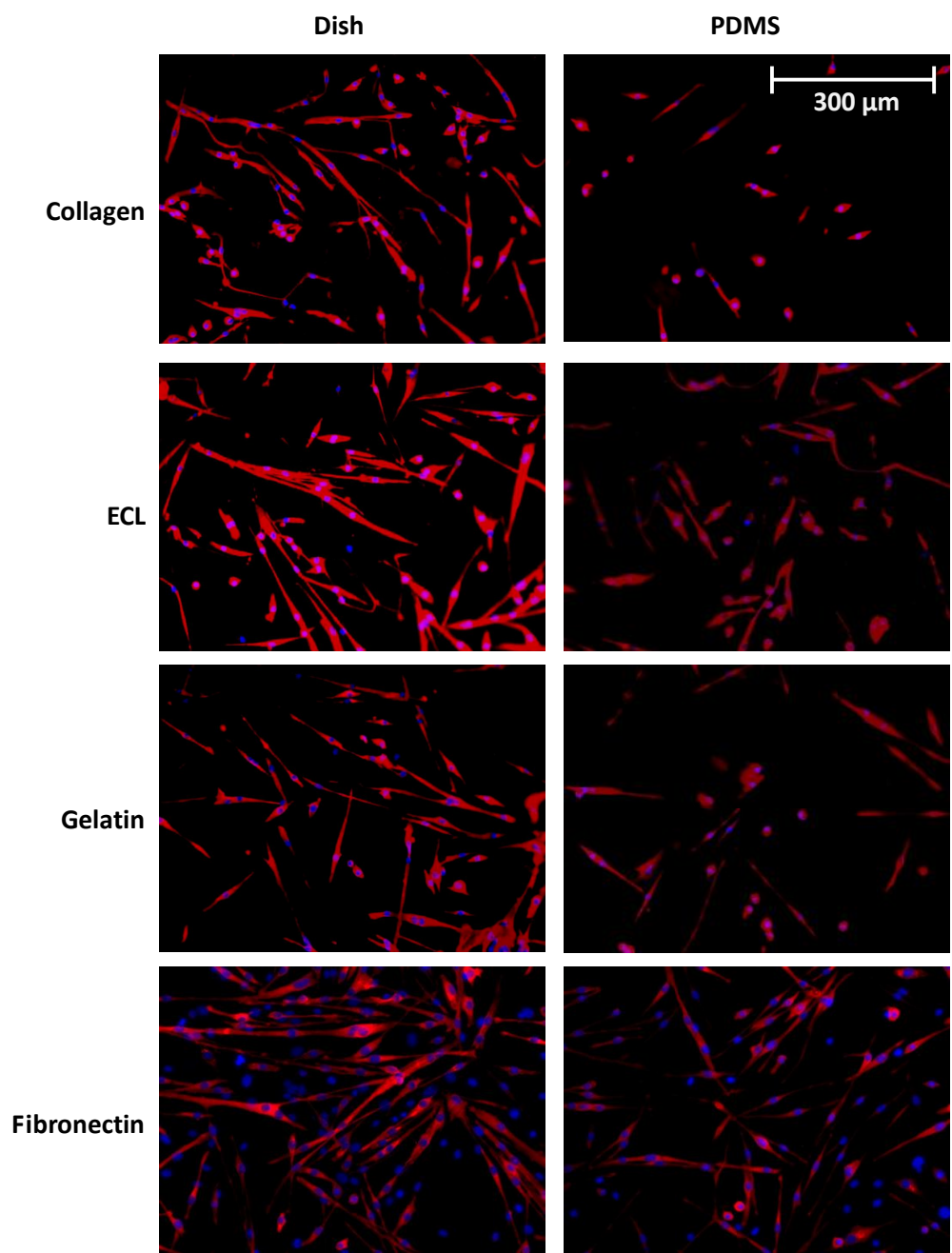
Figure 2.4 MHC immuno-stained myoblasts on dish and PDMS substrate with four different surface treatments.

Cell adhesion onto PDMS was found to be much less than that on culture dishes with any coating matrix. PDMS coated with collagen or gelatin showed significantly less differentiation than PDMS coated with fibronectin and ECL. Fibronectin and ECL were thus used for the OMA experiments in section 4.1 and 4.3.

2.4.3 Flexibility

PDMS has a Young's modulus (E) widely ranging from that of 870 kPa to 360 kPa with various mix ratio between monomer and cross-linker [51][52]. In normal preparation process with 10 : 1 mix ratio, Young's modulus of PDMS, $E \approx 750$ kPa [53] and 0.5 of Poisson's ratio (v) [54] can be used as typical values. Since a thin (10 μm) PDMS membrane sits over 5 μm height electrolyte channel, deflection of the membrane may cause a collapse of the channel by being stuck to the glass substrate. In order to prevent this possible deformation, arrays of posts were introduced into electrolyte channel. High flexibility and deformation of the membrane can also be a problem for cell culture. It is known that the adhesion onto flexible substrate influences the growth of normal cells [55][56] and is strongly cell-type dependent [57]. Therefore, optimal coating will also reduce the poor adhesion of cells on flexible substrates as well as increase of bio-compatibility stated in section 2.4.2.

• Post Array under PDMS Membrane

Due to flexibility of PDMS ($v = 0.5$, $E = 750$ kPa), deflection by its weight needs to be compensated. ANSYS^{TM} software was used to analyze the mechanical deflection, and 5 μm (half of actual thickness) was used for PDMS membrane with fixed boundaries. Maximum deflection at the center was 3.29 mm for 5 mm × 5 mm sheet. This means additional

structure is needed to support the membrane inside the electrolyte channel. Figure 2.5

shows effect of the array as fixed points placed every 0.5 mm, under 5 mm × 5 mm sheet.

Deflection was drastically reduced to 0.27 μm. Denser array was used in fabrication; 10 μm

× 10 μm square posts spaced by 50 μm were patterned (see Figure 3.5 (c)).
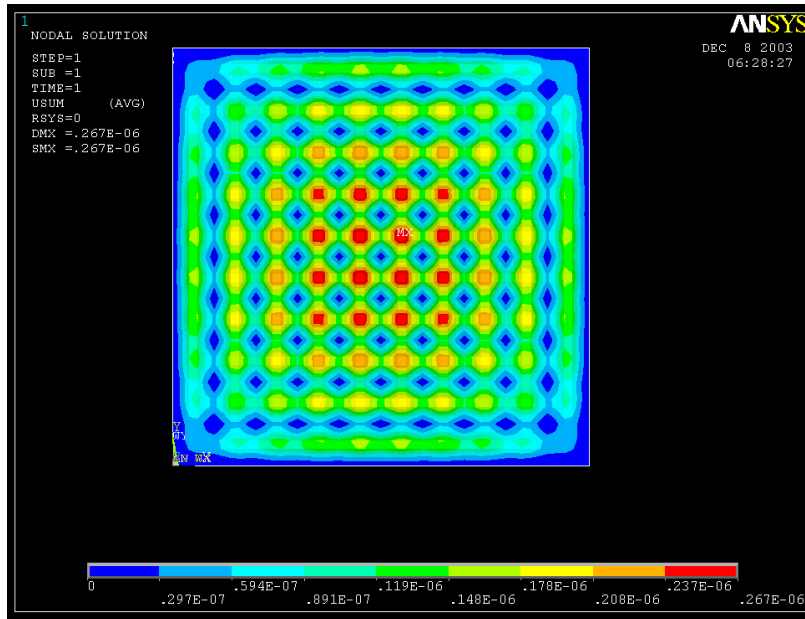
Figure 2.5 ANSYS simulation showing drastically reduced deflection of PDMS

membrane by post array.

• **More Issues on Cell Adhesion**

Despite the advantages of the OMA compared to the previous studies listed in section 2.1,

different culture conditions other than that in the OMA would be required for some cell

culture experiments. For example, in cases when biological results are highly affected by

conditions of culture substrate (e.g. adhesion problem as in section 2.4.2), careful approach

to the experimental condition seems required. Cell adhesion problem on the OMA occurred

during long-term experiments to observe differentiation of wild-type and SOD1 heterozygote myoblasts regardless of the selected coating matrix; warping of the PDMS membrane caused by contractile or traction forces between myoblasts during differentiation could result in poor adhesion of themselves eventually [58]. Migration and proliferation of myoblasts would be affected by the high flexibility of PDMS membrane as well [59]. Therefore, a simple oxygen gradient chip, utilizing a piece of culture dish as a substrate rather than the flexible PDMS membrane, was introduced for long-term experiments with SOD1 heterozygote myoblasts (see section 3.5).

2.4.4 Surface Hydrophobicity

Because of the hydrophobic methyl group (CH_3 in Figure 2.3), PDMS is a hydrophobic polymer. Surface treatment is required to make the channel hydrophilic so the electrolyte channel can be filled with water [60]. Many techniques have been developed to increase the surface energy of PDMS; of these, oxygen plasma treatment is the most commonly used [61][62]. Free radicals generated by oxygen plasma transform methyl group to hydroxyl group (OH) on PDMS surface. Other methods involve silanization [63][64], polymer coating [65], protein coating [66] and UV radiation [67]. Oxygen plasma treatment is used for the operation of OMA due to controllability on surface characteristics and its convenience. Openings on both sides of the electrolyte channel (reservoir site and furthest side from the reservoir) are made to introduce oxygen plasma used for making the channel hydrophilic, thus the electrolyte can flow inside. Cell culture chamber should not cover those openings, and the entire channel ($\sim cm^2$ area and 5 μm height) must be treated with oxygen plasma. Limits of the surface oxidation caused by dimension of the channel, as well as its solution, will be discussed in section 3.2.2 and 3.3.

• Diffusion of Culture Medium Components through PDMS

The non-polar PDMS is basically impermeable to ions, polar solvents and liquids but is permeable to gasses and non-polar organic solvents [42]. As in reaction (2.1) and (2.2), the water electrolysis in OMA involves generation of hydroxide (HO^-) at cathode and proton (H^+) at anode as well as oxygen and hydrogen molecules. Transfer of those produced ions to cell culture area is blocked by the PDMS membrane, eliminating possible pH change by the ions in cell culture medium.

Reliable information on the diffusion coefficients of culture medium components through PDMS is scarce [68][69]. However, Hatanaka *et al.* quantified the permeabilities of several common drugs through PDMS and compared them to the degree of lipophilicity (as PDMS is a highly non-polar, hydrophobic polymer) and molecular weight [69]. Diffusion rates correlated strongly with lipophilicity. Hydrophilic (non-lipophilic) compounds diffused slowly (D $\sim$ 10^{-6} − 10^{-12} mm^2/s); the highest diffusion coefficient for a hydrophilic compound was $\sim$ 10^{-6} mm^2/s for Nicorandil (measure of hydrophilicity: K_{ow} = -1.02). This diffusion coefficient is 10^3 times slower than that for oxygen ($\sim$$10^{-3}$ mm^2/s). Most components of culture medium, salts, sugars and metals, are at least weakly hydrophilic; limited diffusion would thus be expected. Strongly lipophilic drugs (e.g. ibuprofen, K_{ow} = 3.94) were found to diffuse faster (D $\sim$ 10^{-3} − 10^{-6} mm^2/s). Few compounds of this lipophilicity are expected to be available in the aqueous medium in any quantity capable of disturbing the electrolysis.

2.4.5 High Gas-Permeability

The high gas-permeability of PDMS plays a central role in the OMA. Gas diffuses in PDMS

faster than in water, and diffusivity of a gas depends on the size of gas molecule [70]. Various methods have been developed to measure gas-permeability in various conditions, showing different values ($16 - 3.55 \times 10^{-3}$ mm^2/s) of diffusion coefficient of oxygen [71][72][73] in PDMS. Note that the diffusion coefficient can vary more than an order of magnitude with degree of cross-linking of PDMS. Bake times and temperatures during the PDMS curing strongly determine stiffness and diffusion rates of gases through the polymer [74]. The diffusion coefficients used in section 2.5.1 were determined based on data for published cure recipes for our specific material [75][76].

• **Maximum Flux of Dissolved Oxygen**

The maximum oxygen flux delivered to cell culture area would be limited by the onset of gas bubble nucleation at the electrode. Gas bubbles occur when the concentration of oxygen at the electrode surface is high enough to favor the existence of an oxygen gas phase; this threshold is strongly dependent on electrode roughness, geometry and polarization history [77]. Once bubble nucleation occurs, the dissolved oxygen dosed to the cells is no longer directly dependent on the electrode current, but is now limited by the gas-liquid interface mass transfer resistance [78], causing increase of bubble size with the oxygen generation ratio. The bubble generation inside the electrolyte channel causes several problems for proper operation of the OMA. First, the generated bubble affects desired microgradient profile; all designs of the microgradients are well-defined and constructed with dissolved oxygen. Second, the pressure of the bubble can deform the flexible PDMS membrane, which gives poor cell adhesion and imaging. Lastly, during electrolysis a bubble grows to cover the entire anode or cathode, displacing electrolyte away from the electrodes.

• **Cellular Oxygen Demand**

An initial concern was whether the electrodes could generate dissolved oxygen at rates exceeding the oxygen demand of typical cells. In order to maintain desired oxygen gradients, the microelectrode array must be able to supply significantly more oxygen than that demanded by cells (i.e. if the oxygen dose to a cell equaled its oxygen consumption exactly, the local dissolved oxygen tension would be close to zero). A C2C12 cell under normoxic conditions consumes approximately 2.5 fmol O_2/min; as this demand decreases with oxygen tension, it can be considered an upper bound [79]. The surface area of a C2C12 cell ranges from $100 - 1000$ μm^2 depending on the confluence. This corresponds to ~2.5 × 10^{18} molecules $O_2/\mu m^2$min. Using equation (2.3), this oxygen flux can be converted to current density, yielding ~10 nA/mm^2. At the maximum current density, 1 mA/mm^2, applied in the OMA and does not nucleate oxygen bubble, is approximately 10^5 times larger than the flux required by cellular oxygen demand. The microelectrode array is thus able to generate significantly more oxygen than this without nucleating bubbles and maintain high oxygen concentrations in the face of cellular oxygen consumption.

2.5 Oxygen Microgradient Simulation

Finite element simulations were carried out to examine the oxygen concentration profile from a single electrode and how multiple electrodes could be used to construct arbitrary gradients. The key concept in forming arbitrary gradients is that each of the multiple electrodes generates distinct amounts of oxygen; these different sources superimpose to generate interesting microgradients. Additionally, finite element simulations of the cell culture environment were used to study the generation and concentration of hydrogen peroxide in section 3.7.3.

2.5.1 Finite Element Simulation Model

2-D diffusion simulations made use of COMSOL^{TM} 3.1. The geometry and boundary conditions are graphically summarized in Figure 2.6. The electrolyte channel, PDMS membrane, cell culture area, and top PDMS culture chamber have thickness of 5 μm, 10 μm, 150 μm, 500 μm, respectively. The device was modeled in 2-D, assuming it is 'infinitely' deep in y-axis and 3 cm wide. Diffusion coefficients of oxygen in PDMS and water (electrolyte) were set to 4×10^{-3} mm^2/s [71] and 2×10^{-3} mm^2/s [80], respectively.

Figure 2.6 FEM simulation model for oxygen microgradient.
(a) Geometric parameters for simulation. **(b)** Boundary conditions and diffusion coefficients. Oxygen concentration is zero at red boundary, no flux at blue boundary, and generated oxygen at electrode is modeled by applying input flux.

Oxygen enters the tissue culture from the microelectrodes and exits because of diffusion into the ambient; the device is assumed to sit in a defined, oxygen-free atmosphere (e.g. no oxygen outside the device). The lowest layer glass substrate was modeled as impermeable to oxygen (oxygen flux across the boundary is equal to zero). The cross-sectional area of the 150 nm thick oxygen-evolving electrode was modeled as a boundary condition having some inward flux of oxygen molecules. It was assumed there is no convective flow in the cell culture chamber (i.e. cells are grown as a batch culture with no continuous fluid flow).

2.5.2 Oxygen Concentration Microgradient from Single Electrode

Given only one oxygen source from a single microelectrode, a 2-D steady-state diffusion model predicts a sharp peak of oxygen concentration across the floor of the cell culture area (blue line in Figure 2.7 (b)). Oxygen gradient across the top of the medium layer showed similar shape but it had much lower level area (red line in Figure 2.7 (b)). Oxygen peak decreases as measuring height inside the area of culture medium increases thereby forming a shape of narrow Gaussian function, but we need to consider only the oxygen level just above the PDMS membrane because the cells of interest sit on the floor of the membrane.

Figure 2.7 Steady-state FEM simulation of single microgradient.

(a) Illustration of FEM model component. **(b)** Single and sharp oxygen concentration plots at both just above PDMS membrane and just below PDMS cover. **(c)** 2-D plot of oxygen concentration, **(d)** magnification around the oxygen source (electrode).

Saturation time was also calculated for dynamic change of microgradient. From the time-dependent solution, 95% saturation reached within 8 seconds, which will be short time enough for aerobic bacteria and mammalian cells to respond. 17.4% of oxygen peak in Figure 2.7 was calculated with 1.65×10^{13} molecules/mm^2 input flux. Assuming a 1 mm long electrode, current density will be 10.6 µA/mm^2. The shape of the narrow Gaussian function is advantageous. Since the oxygen microgradient generated by a single electrode is sharp, adjacent microelectrodes − each generating distinct, different amounts of oxygen − can be used to create arbitrary microgradient profiles in cell culture area (section 2.5.3).

• **Thickness of PDMS Membrane and Electrolyte Channel**

The effect of PDMS thickness on microgradient profile was considered as a part of microgradient design. Geometric conditions of 10 µm thickness of PDMS membrane and 5 µm thickness of electrolyte channel stated in this section were determined after multiple times of simulation and microfabrication. It would be advantageous to make arbitrary microgradient using multiple electrodes when a single microgradient generates sharper gradient profile. In other words, steepness of arbitrary microgradient is limited by that of single microgradient profile. In order to achieve sharp microgradient, height of electrolyte channel and thickness of PDMS membrane needs to be minimized to place the electrode (oxygen source) closer to the floor of PDMS membrane (cell culture layer). Moreover, higher peak of oxygen microgradient from single electrode is preferred for any desired oxygen microgradient because high oxygen peak is limited by the maximum current that avoids bubble nucleation.

Figure 2.8 Simulated effect of electrolyte channel and PDMS membrane geometries. Input flux is fixed and oxygen levels are measured 1 μm above the membrane by **(a)** varying thickness of PDMS membrane, with fixed 5μm electrolyte layer, and by **(b)** varying thickness of electrolyte layer, with fixed 10μm PDMS membrane.

As shown in Figure 2.8, higher and sharper microgradient was obtained with smaller thickness of electrolyte layer and PDMS membrane. Less than 5 μm electrolyte layer could be fabricated; however, it would be more difficult in loading electrolyte. The difficulties of filling electrolyte will be discussed in section 3.2.2, and design of OMA was modified not to increase the 5 μm channel height (section 3.3). Minimum thickness of PDMS membrane could be 6 μm (see Figure 3.3), but frequent failures of the 6 μm thickness membrane during microfabrication, such as being stuck to glass substrate by collapsed membrane or broken during the channel release process (section 3.1.3), were observed. Increased thickness to 10 μm solved those problems on the membrane failure. Therefore, 5 μm height of electrolyte channel and 10 μm thickness of PDMS membrane were chosen for electrolyte loading and various microgradient construction.

• **Joule Heating and Electrode Corrosion**

There will also be a Joule heating across the resistance of electrode and electrolyte, but the amount of the power is as low as the heating can be neglected. As an example, 2 μA across a typical electrode will generate ~ 3.5 V; so the power for Joule heating is 2 μA × 3.5 V = 7 μW. For the single electrode shown in section 2.5.2 (20 μm width × 1 mm long), heat flux density for 7 μW is 0.35 mW/mm^2. Figure 2.9 shows the simulation result of heat transfer from electrode to the OMA structure. Based on the simulation model in Figure 2.7, glass substrate (500 μm thick) under the electrolyte layer was modeled for this simulation. Thermal properties of water, PDMS, and glass are listed in Table 2.2.

Table 2.2 Properties of three materials used in COMSOL[TM] simulation.

Material	Thermal conductivity (W/m·K)	Density (kg/m³)	Heat capacity (kJ/kg·K)
Water	0.58	9.97×10^2	4.18
PDMS	0.15	9.2×10^2	1.46
Pyrex glass	1.05	2.23×10^3	0.84

Figure 2.9 Temperature increase in the OMA due to Joule heating by electrolysis.

Assuming that 10 times of the heating (3.5 mW/mm²) occurred on the anode area, the temperature elevation on the PDMS membrane was 0.001 °C. Because thermal conductivity

of PDMS is much lower than that of glass, most heat from the electrode is transferred downward through the glass substrate. Therefore, the 7 μW is not sufficient to elevate the chip temperature appreciably.

Based on previous studies of gas evolving Ti/Pt electrodes [34][81], no corrosion of the electrodes is expected or experimentally observed at any current densities in this thesis.

2.5.3 Arbitrary Microgradients from Multiple Electrodes

Multiple microelectrodes in an array can be used to construct a multi-dimensional oxygen microgradient much in the same way that pixels in a display can be used to pattern images. The key to patterning and controlling arbitrary oxygen microgradients lies in the ability to control oxygen generation rates at different sites simultaneously and is strongly dependent on the diffusion microenvironment. Figure 2.10 demonstrates concept of arbitrary gradient schematically.

Before the simulation of desired microgradient profile, the oxygen microgradient from the single electrode was estimated with a mathematical expression. Curve Fitting Toolbox in Matlab^{TM} was used, and three terms of Gaussian function, derivative of error function, were chosen to express the oxygen microgradient, which showed the best fit with least parameters.

$$c(x) = Ae^{-\left(\frac{x-x_1}{B}\right)^2} + Ce^{-\left(\frac{x-x_1}{D}\right)^2} + Ee^{-\left(\frac{x-x_1}{F}\right)^2}$$

(2.13)

Where $c(x)$, x_1 and $A - F$ are concentration profile, position of electrode, and parameters to be solved, respectively. The calculated values of the parameters are listed in Table 2.3, with

various input fluxes. Minimizing the number of parameters is useful when many independent electrodes are used to fit an arbitrary concentration profile. From the Table 2.3, the parameters are closely related to the input flux. The relationship between input flux N and parameters are plotted in Figure 2.11. Parameters A, C, E and F can be linearly related to input flux, whereas B and D can be considered as constant values.

Figure 2.10 Conceptual illustration of arbitrary microgradient.

(a) Microgradient generated by a single, long and thin microelectrode along the floor of the cell culture chamber **(b)** By superimposing several such doses with a microelectrode array, different gradients can be patterned into monolayer culture. Note that each microelectrode in the array generates distinct amounts of oxygen.

Table 2.3 Calculated parameters for equation (2.13) with various input flux.

Input flux N (molecules /mm³s)	A	B	C	D	E	F	Peak concentration (%)
0.5×10^{13}	0.441	0.172	0.675	0.061	0.320	0.340	1.436
1.0×10^{13}	1.027	0.214	1.451	0.069	0.796	0.429	3.273
1.5×10^{13}	1.648	0.216	2.071	0.062	1.557	0.461	5.276
2.0×10^{13}	2.517	0.211	2.837	0.062	2.047	0.461	7.404
2.5×10^{13}	3.320	0.214	3.599	0.068	2.527	0.490	9.451
3.0×10^{13}	4.101	0.218	4.266	0.062	3.315	0.514	11.685
3.5×10^{13}	4.941	0.216	4.919	0.062	4.148	0.530	14.005

Figure 2.11 Relationship between N and other parameters.

Table 2.4 Parameters expressed as a function of input flux or constant value.

A	$1.502N - 1.182$
B	0.209
C	$1.337N\text{-}0.505$
D	0.064
E	$1.251N\text{-}1.027$
F	$0.050N\text{-}0.337$

All the parameters can thus be expressed as one parameter, input flux *N* as in Table 2.4. Therefore, equation (2.13) can be expressed as :

$$c(x) = (0.61N - 0.48)e^{-\left(\frac{x - x_1}{0.085}\right)^2} + (1.337N - 0.505)e^{-\left(\frac{x - x_1}{0.064}\right)^2}$$

$$+ (1.251N - 1.027)e^{-\left(\frac{x - x_1}{0.05N - 0.337}\right)^2} \tag{2.14}$$
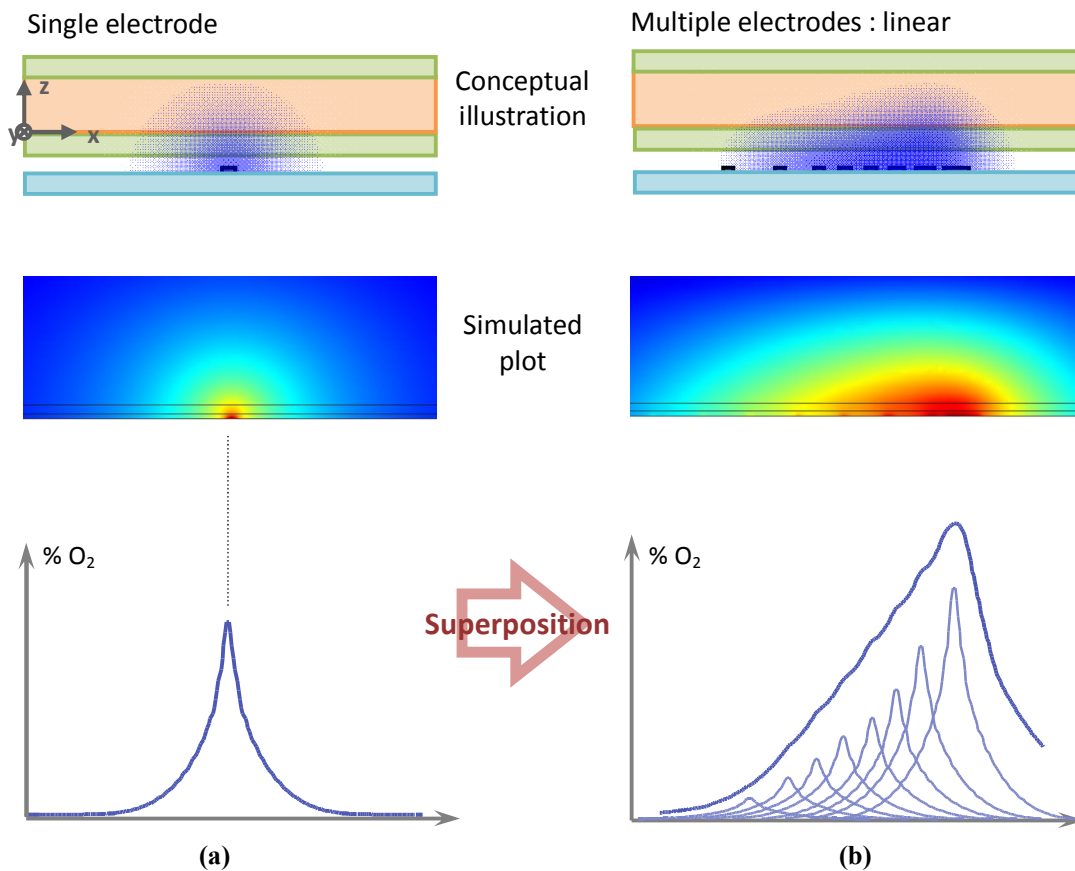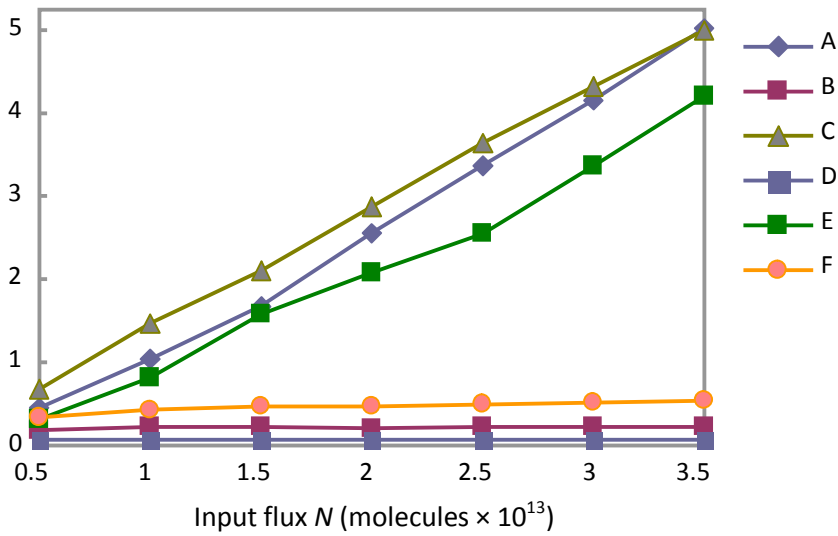
This equation will be used in construction of arbitrary microgradients. Variables are only the input flux *N* and position of the electrode x_1. For example, if the target is linear, numbers of the estimated equation (2.14) are used to fit the linear gradient. Figure 2.12 (c) was chosen from the various configurations in Figure 2.12, and values of parameters are listed in Table 2.5. This configuration generates 0.5 mm wide linear gradient with 8 independent electrodes. Note that the width of each electrode is fixed to 20 μm.
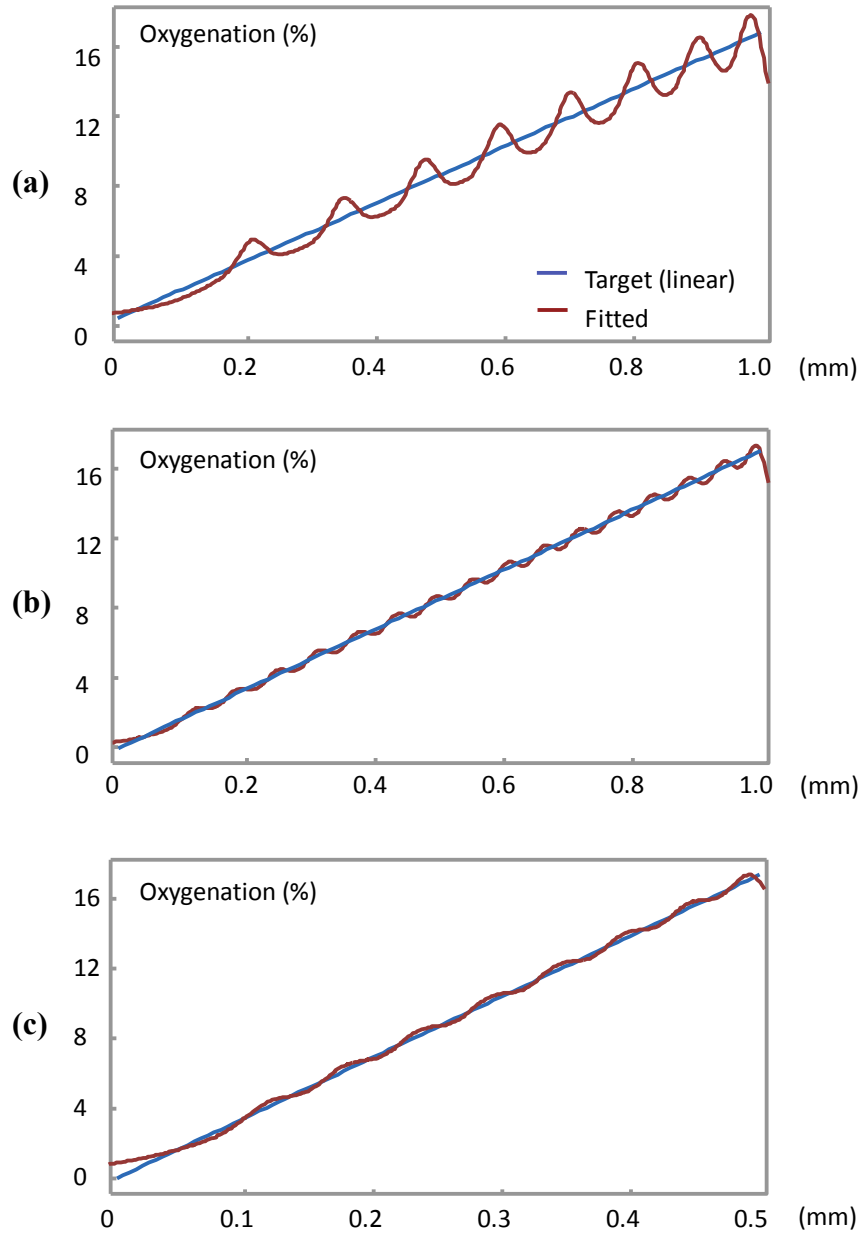
Figure 2.12 Various configurations of multiple electrodes to generate a linear microgradient by curve fitting method.

Blue line is linear target and red line is fit result. **(a)** 1 mm wide gradient with 8 electrodes, **(b)** 1 mm wide gradient with 16 electrodes, **(c)** 0.5 mm wide gradient with 8 electrodes.

Table 2.5 Electrode position and input flux of 8 electrode for linear microgradient.

Electrode number	Input Flux N (molecules/mm^{3}s)	Electrode Position x_1 (µm)
1	0.182×10^{13}	121
2	0.308×10^{13}	180
3	0.42×10^{13}	236
4	0.49×10^{13}	292
5	0.56×10^{13}	345
6	0.644×10^{13}	397
7	0.812×10^{13}	449
8	2.485×10^{13}	498

However, each electrode generates different amount of oxygen, which needs to be implemented with independent current sources. If we modify the fixed width of each electrode with maintaining the same input flux, amount of oxygen can be modulated. In other words, instead of applying different input flux on each electrode having fixed width, width of each electrode can be adjusted to make various oxygen peak while maintaining the same input flux density for all electrodes. Input flux of each electrode in Table 2.5 was converted to various electrode widths with fixed input flux, 0.607×10^{13} molecules/mm^{3}s (Table 2.6). All the independent electrodes can be connected to one current supply, generating distinct amount of oxygen from each electrode and desired arbitrary microgradient by superposition.

Other microgradients such as round shape and triangular shape are summarized in Table 3.1 with geometry data. The results of these simulations are presented alongside experimental data in section 3.7.2.

Table 2.6 Conversion of input flux in Table 2.5 to electrode width.

Input Flux N (molecules/mm^{3}s)	Fixed input Flux (molecules/mm^{3}s)	Electrode width (µm)
0.182×10^{13}		3.0
0.308×10^{13}		5.1
0.42×10^{13}		6.9
0.49×10^{13}		8.1
0.56×10^{13}	0.607×10^{13}	9.2
0.644×10^{13}		10.6
0.812×10^{13}		13.4
2.485×10^{13}		41.0

Chapter 3

Device Fabrication and Oxygen Microgradient Measurement

3.1 Fabrication Process

Fabrication steps listed in this section describes the first version of OMA, processed with equipments and chemicals in the Solid-State Electronics Laboratory in the University of Michigan, Ann Arbor. The later modified version processed in the Berkeley Microlab shares most of the process (section 3.4). There are also modifications and additions to the process for an improved version discussed in section 3.3.

3.1.1 Wafer Cleaning and Electrode Patterning

The device was fabricated on a 4" Pyrex glass substrate which was cleaned in Piranha (1:1 = $H_2SO_4 : H_2O_2$) for 20 minutes followed by a 10 minutes rinse-dry cycle. After coating HMDS at 3000 rpm for adhesion of photoresist, 1.2 μm photoresist (1813, Shipley) was spun

on the clean substrate at 2000 rpm for 30 seconds, pre-baked at 100 °C hot plate for 50 seconds (Figure 3.1 (a)). The glass substrate was then UV-exposed for 7.5 seconds in a mask aligner (MA6, Karl Suss) aligning with a chrome mask patterned electrode design. Microposit MF-319 developer was used to dissolve UV-exposed photoresist (Figure 3.1 (b)). A descum was performed for 3 minutes with 80 W oxygen plasma (March Asher PX-250) to remove residual photoresist around the electrode pattern. Titanium (Ti, 500 Å) and platinum (Pt, 1000 Å) were deposited using evaporation (Enerjet E-Beam Evaporator) with deposit ratio of 10 Å/sec and 5 Å/sec, respectively (Figure 3.1 (c)). Electrodes were patterned using lift-off process (Figure 3.1 (d)), with sonication in strong photoresist remover (1112A, Shipley) for 20 minutes. To remove residual metal particles stuck on a surface while rinsing, DI water-jet spray was applied for 5 minutes.
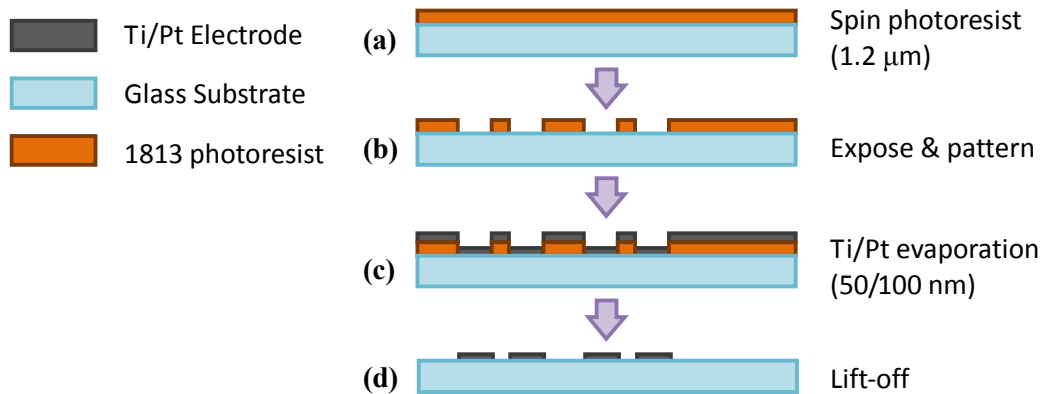
Figure 3.1 Electrode patterning using lift-off process.

3.1.2 Patterning Electrolyte Channel Layer

After HMDS spin-coat at 3000 rpm, 5 μm photoresist (1827, Shipley) was spun on the electrode-patterned substrate at 1200 rpm for 30 seconds, and pre-baked at 100 °C hot plate

for 50 seconds (Figure 3.2 (a)). Channel patterns were exposed for 17 seconds in MA6 aligning with a channel patterned mask and developed for 2 minutes in MF-319. Oxygen plasma treatment was followed with March Asher (250 mTorr, 80 W, 1 min) to enhance adhesion of PDMS to the substrate (Figure 3.2 (b)) as well as descuming the photoresist residue. PDMS (Sylgard 184, Dow Corning) was prepared by mixing in a 10:1 ratio of base and curing agent, spun on the substrate with 10 μm thickness, followed by allowing the PDMS to flow and flatten the surface for 10 minutes. Figure 3.3 shows measured thickness of PDMS with various spin speeds. The PDMS was then cured for 15 minute on 110 °C hot plate (Figure 3.2 (c)).
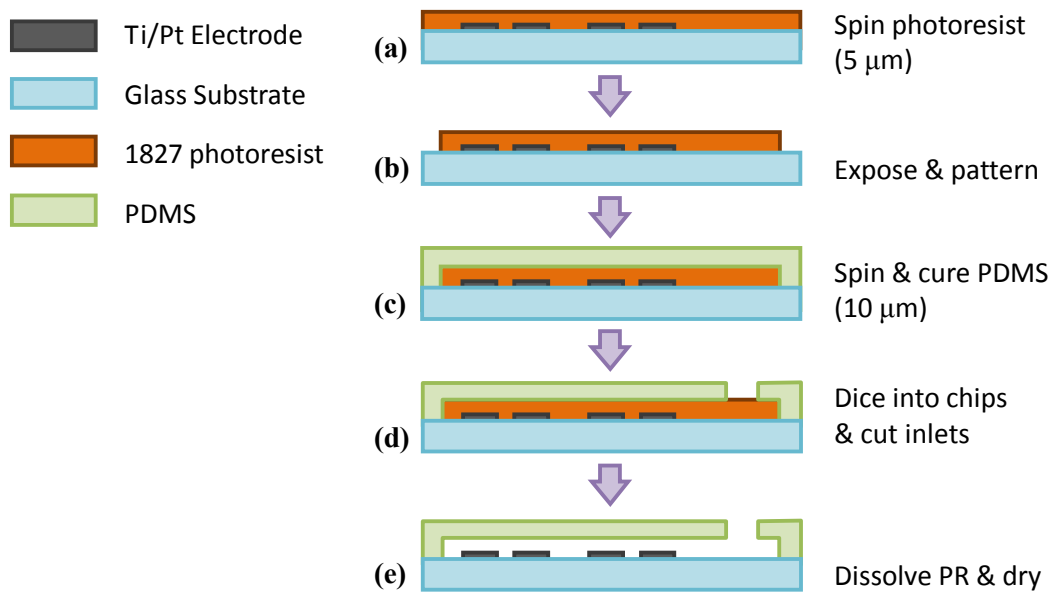
Figure 3.2 Patterning electrolyte channel using sacrificial layer and PDMS.
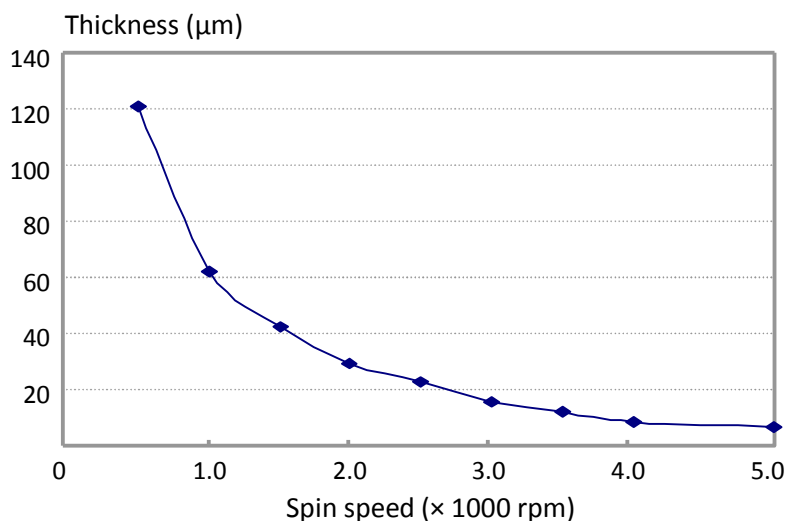
Figure 3.3 PDMS thickness vs. spin speed.

Spin conditions are : pre-spin of 30 seconds at 500 rpm followed by 40 seconds at various speeds.

3.1.3 Wafer Dicing and Releasing Channel Layer

The substrate was then diced into 6 mm × 20 mm chips, and the PDMS at the position of the liquid inlet was cut out carefully with razor blade to enhance the next step (Figure 3.2 (d)). The photoresist entrapped below the PDMS layer was removed by immersing the chip into acetone for 3 hours with ultrasonic shake. The chip was quickly transferred into methanol and sonicated again for 1 hour to remove acetone inside the PDMS and channel layer. The chip was then quickly transferred on 110 °C hot plate and dried for 1 minute (Figure 3.2 (e)). The quick evaporation of methanol on hot plate prevents the PDMS membrane from being stuck on the glass substrate, by pushing up the membrane. Those dried chips were inspected with microscope to find out broken or collapsed area of PDMS membrane, and baked in 160 °C oven overnight for complete cure of the PDMS.

3.1.4 Mold Preparation for Top PDMS Culture Chamber

Another PDMS layer, which serves as cell culture chamber, was molded into a cavity with a 4 mm × 15 mm area and 150 μm thickness with three microfluidic ports for loading cell culture medium. To fabricate the mold, 40 μm of 9260 photoresist was achieved by spin-coating (500 rpm for 10 sec / 1000 rpm for 30 sec) 20 μm thickness on a Si substrate, surface stabilization for 5 minutes, softbake at 110 °C for 1 minute, removal of edge bead, and repeating the 20 μm spin-coating followed by surface stabilization in sequence (Figure 3.4 (a)). After softbake in 90 °C oven for 30 minutes, mold patterns were exposed for 200 seconds in MA6 and developed for 5 minutes in 1:3 of AZ-400K (Clariant) : DI water followed by hardbake in 110 °C oven for 30 minutes (Figure 3.4 (b)).
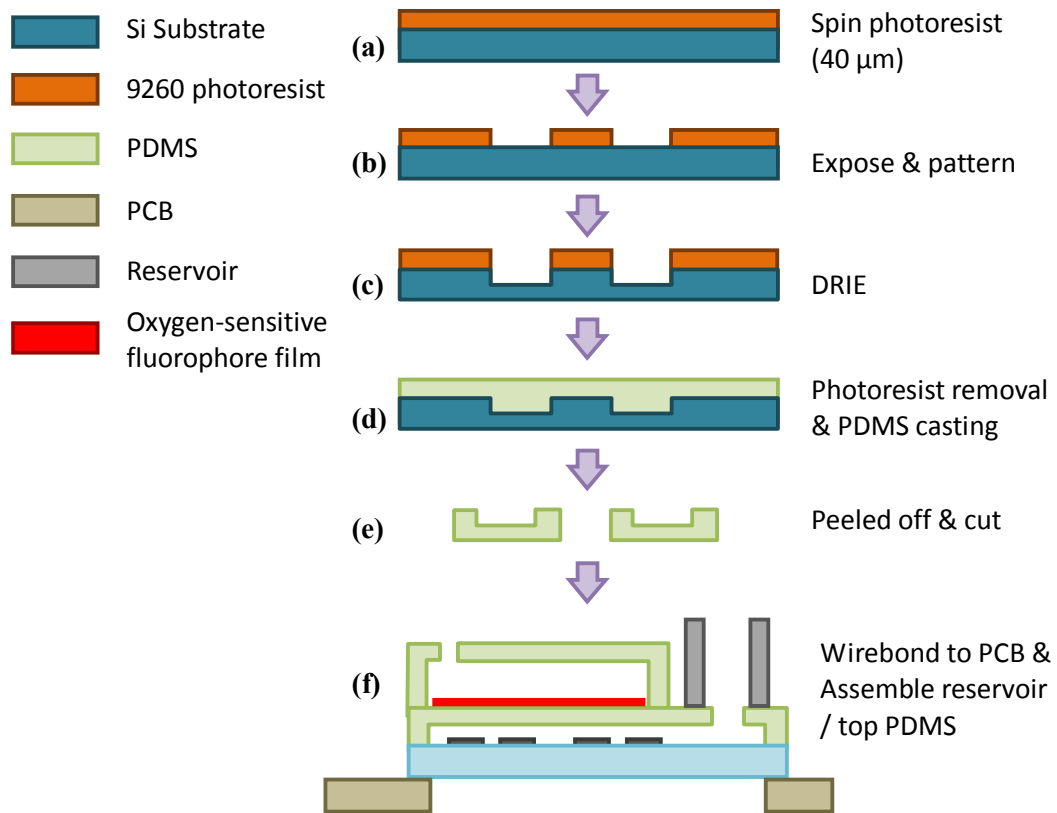
Figure 3.4 Mold casting of top PDMS culture chamber and packaging

After descuming process with March Asher, 150 μm deep mold was etched using DRIE (Figure 3.4 (c)). The photoresist was then removed in PRS 2000 photoresist remover for 10 minutes. Mixed Sylgard 184 was applied on the patterned Si substrate with amount of making 500 μm thickness followed by degassing in a vacuum chamber and curing on 110 °C hot plate for 15 minutes (Figure 3.4 (d)). Cast PDMS was peeled off and cut into units (Figure 3.4 (e)).

3.1.5 Reservoir and Culture Chamber Assembly

After attaching the chip onto a custom-made PCB with a silicone glue (734 RTV silicone, Dow Corning), PDMS membrane at the edge of electrodes (where wire-bonding is applied) was peeled off, and electrodes were wire-bonded to the PCB with aluminum wire. The PCB provides electrical connection between the electrodes and the outside circuitry (current source). The cell culture chamber and a 3 mm diameter and 10 mm height aluminum reservoir tube were attached to the first PDMS layer with Sylgard 184 as a glue (Figure 3.4 (f)) and the PDMS is cured on 100 °C hotplate. For some chips to measure oxygen level, a 10 μm thick oxygen-sensitive fluorophore film (Oxysense, Inc., see section 3.7.2) was laminated prior to attaching the PDMS cell culture chamber units.

3.1.6 Chip Operation

Just prior to operation, the completed chip was exposed to oxygen plasma to make the PDMS temporarily hydrophilic. This was required for easy electrolyte loading into the microelectrode channels, and more consideration will be discussed in section 3.2.2 and 3.3. After loading DI water into electrolyte channel, suspension culture of either mammalian cells or bacteria was loaded into cell culture chamber. For anoxic condition outside OMA, the chip

was placed into a gas-control chamber as shown in section 3.6.

3.2 Fabricated OMA

3.2.1 Fabricated Chip Picture

Figure 3.5 shows the fabricated OMA, before assembling the cell culture chamber to visualize elements under the chamber. Pads for wire-bonding are used to connect power supply. Electrolyte loaded from aluminum tube reservoir spreads into a main electrolyte channel and various designs. The magnified picture (Figure 3.5 (b)) shows a design that consists of 10 parallel, independently controllable electrodes (each 20 µm wide × 1 mm long, separated by 80 µm) as an example. A cathode patterned under main electrolyte channel is shared, or another design can also be used as a cathode.

Note that the regular array of dots in Figure 3.5 (c) is PDMS posts which hold up the PDMS membrane below the chamber as shown in section 2.4.3. A fully fabricated oxygen microgradient chip is shown in Figure 3.5 (d). Cell suspension is loaded through one of the three microfluidic ports. These openings and reservoir were capped with molded silicone to prevent culture medium evaporation.
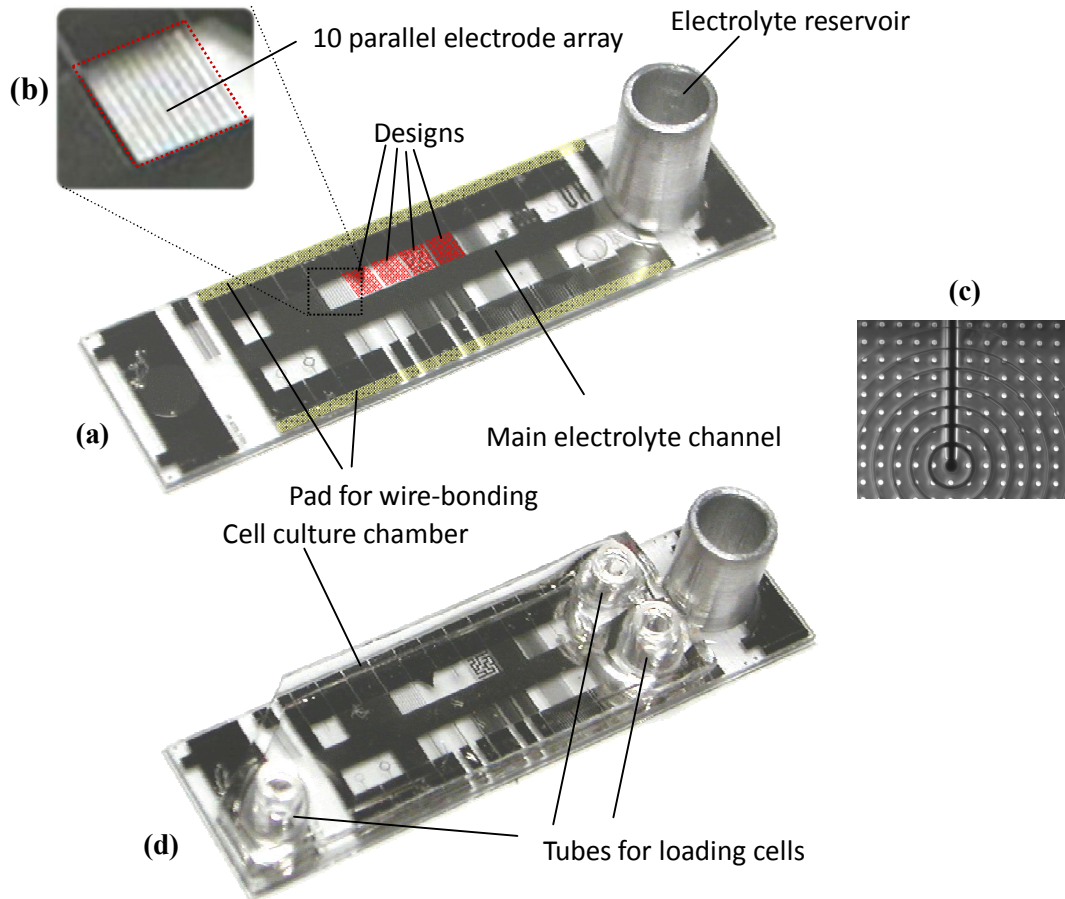
Figure 3.5 Picture of fabricated OMA.

(a) Before assembling cell culture chamber. Each design has 1 mm × 1 mm size on 8 mm × 18 mm size chip. **(b)** Magnified, red area shows one of oxygen gradient area **(c)** Regular array of 10 μm × 10 μm sized posts, spaced by 50 μm. **(d)** Fully fabricated chip picture.

3.2.2 Problem for Electrolyte Loading

The biggest problem of the early device was difficulty of filling electrolyte. Oxygen plasma treatment has been widely used and can be a solution (section 2.4.4). In case of OMA, however, the channel height is only 5 μm and due to post array inside channel, only 1.5 mm

distance from opening was able to be oxidized by the plasma treatment. In other words, if both side of the channel is open and the oxygen plasma is applied, the maximum channel width will be 3 mm (Figure 3.6).
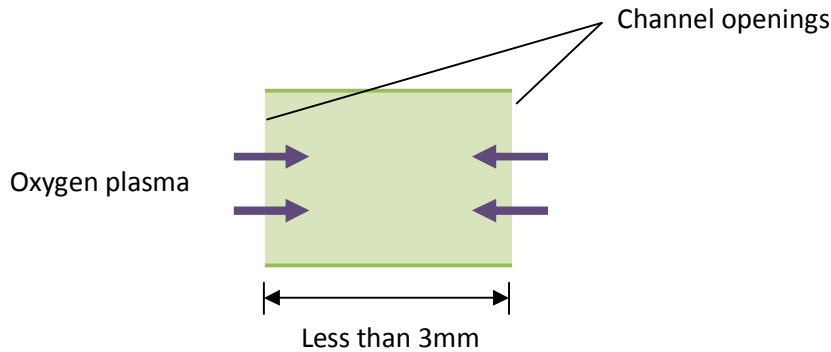
Figure 3.6 Schematic top view of 5 μm height channel.

Mixing with minimal amount of surfactant with water would be one of solution to fill the hydrophobic channel. However the surfactant diffuses though the PDMS membrane and its cytotoxicity affected the cell's viability [82]. Vacuum and release method [83] was introduced for characterization of the microgradient (section 3.7), but high possibility of trapping bubbles around corners existed and showed slow progress of filling.

3.3 Improvements of OMA

Two modified designs of OMA have been developed, resulting in successful surface treatment of entire electrolyte channel with oxygen plasma. The modifications were to confine the channel width less than 3 mm from both sides of opening as discussed in section 3.2.2.

3.3.1 Circularly Patterned OMA

Geometry of circularly patterned OMA is graphically described in Figure 3.7. The

electrodes and each microgradient area are aligned toward the center (Figure 3.7 (a)). A circular electrolyte channel sits on the top, and a reservoir (cut from 200 μL pipette tip) is placed at the center.
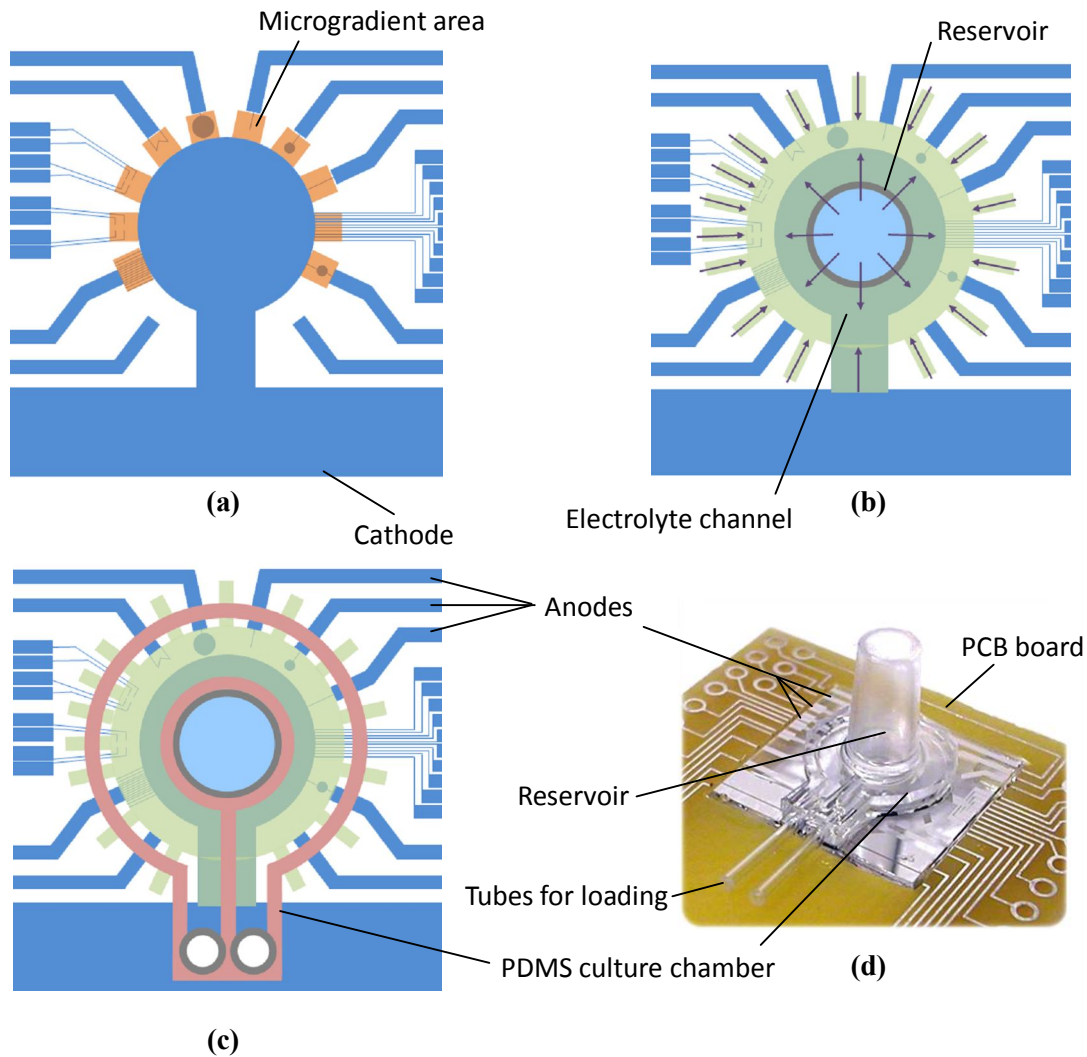
Figure 3.7 OMA having circularly patterned electrode array.

Chip size is 15 mm × 15 mm. **(a)** Electrode pattern (blue) and each microgradient area. Ten independent, 1 mm × 1 mm microgradient designs (orange) are circularly placed. **(b)** Electrolyte channel later (yellow) and oxygen plasma (arrows). **(c)** With cell culture chamber and tubes. **(d)** Fully fabricated chip picture.

The oxygen plasma coming from the bottom of reservoir and the edges of electrolyte channel (protruded outward) can oxidize all the channel area based on the criterion in section 3.2.2 (Figure 3.7 (b)); therefore electrolyte can be filled in all the channel area. Additionally, the round shape of culture chamber was designed to circulate culture medium through the tubes with syringe pump (Figure 3.7 (c)). However, a bubble formation occurred inside culture chamber during operation, and experimental setup became complicated due to tubes and syringe pumps. The reason for the bubble formation may be the lowered solubility limit for the circulating medium at 37 °C, because the medium in syringe was loaded at room temperature. This problem could be solved if the culture medium is prepared with 37 °C to remove effect of the solubility change in the medium before connection to the OMA. This design was used for bacterial experiment demonstrated in section 4.1.3.

3.3.2 Point Source Microgradient Chip

Despite the benefits from OMA system such as dynamic change and arbitrary patterning of oxygen microgradient, there arose a need for a simplified version of oxygen microgradient. Moreover, since most participation in this work was done with the metal electrodes used presented an imaging problem. In addition, it became desirable to generate a microgradient across a wider culture area (more than 1 mm × 1 mm) to increase gradient resolution so that more cells could be maintained at the same oxygen level. A wider culture area require a wider electrolyte channel, which exceeded the 3 mm width limit described in section 3.2.2; however, the entire electrolyte channel still needs to be treated with oxygen plasma to fill electrolyte easily.
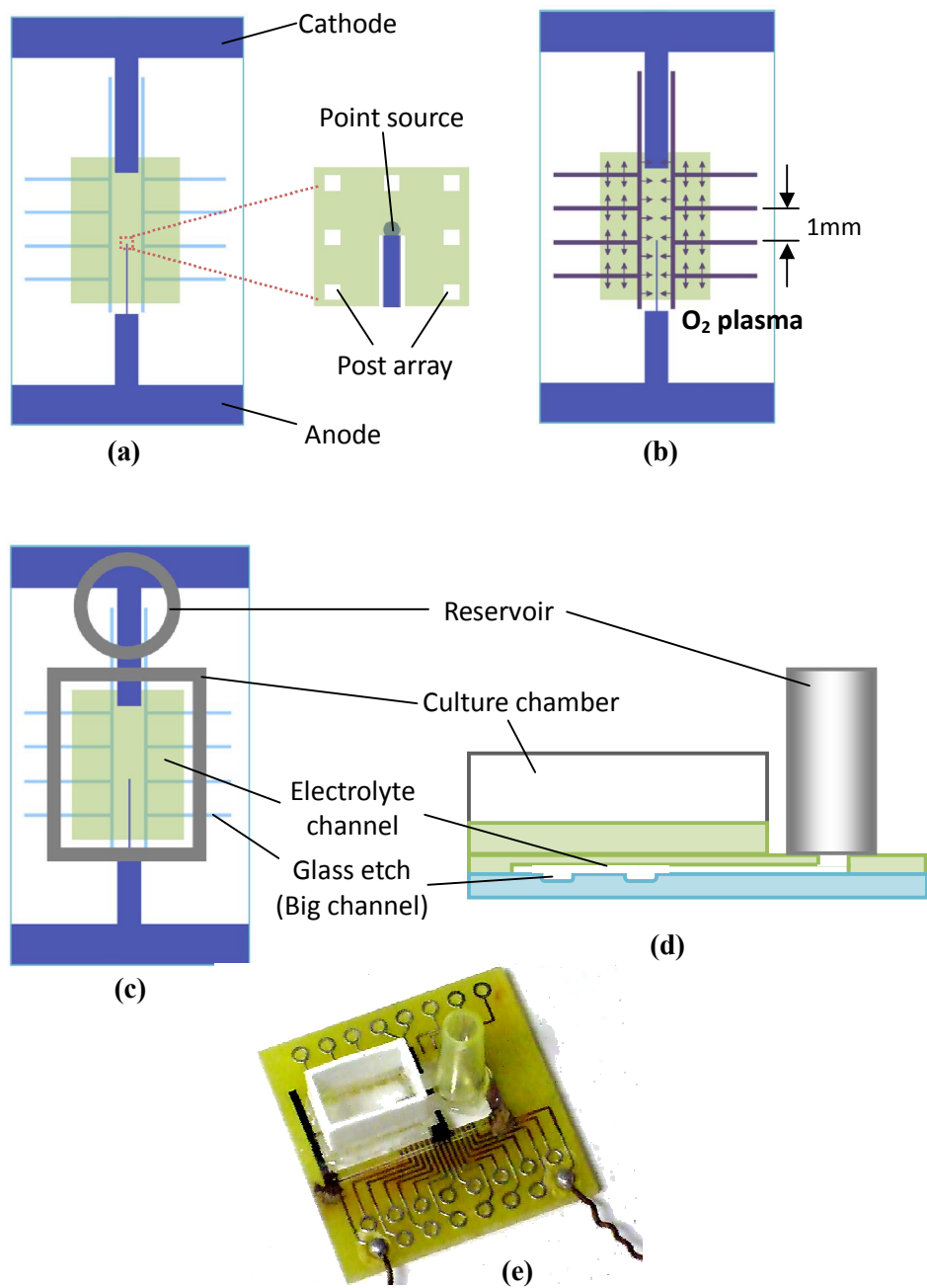
Figure 3.8 OMA with a point electrode and glass-etched electrolyte channel.

Chip size is 10 mm × 15 mm. **(a)** Electrode pattern (blue) and electrolyte channel area (yellow). Big channel is patterned on glass (light blue). **(b)** Oxygen plasma can be introduced all the channel. **(c), (d)** With cell culture chamber and tubing. **(e)** Picture of fabricated chip.

To satisfy those requirements, more fabrication steps were introduced to oxidize the wide area of electrolyte channel and only a single point electrode was placed at the center of chip. 50 μm depth and 300 μm width additional electrolyte channel was patterned on the glass substrate by wet etching. This big channel allows oxygen plasma to enter and spread into entire channel easily. The space between the big channel is 1 mm, and the big channel is connected to electrolyte reservoir and extended outward of the culture chamber. The magnified illustration in Figure 3.8 (a) shows the point oxygen source; only the round tip of Ti/Pt electrode is exposed to the electrolyte channel (other areas were covered with PDMS). A culture chamber (5 mm × 8 mm and 4 mm height) replaced the top-covered PDMS chamber, made with 1 mm tall PDMS ring and a 3 mm tall polystyrene rectangular tube.

A glass wet-etch process for patterning the big channel was added to the fabrication process described in section 3.1. Piranha-cleaned glass substrate was immersed into 10:1 diluted BHF for 5 minutes. This additional cleaning process is required for adhesion of chrome (Cr) / gold (Au) layer. After patterning electrodes described in section 3.1.1, 1000 Å / 5000 Å of Cr/Au were deposited by evaporation on both side (to prevent backside etch of substrate) with deposit ratio of 15 Å/sec and 10 Å/sec, respectively. 40 μm 9260 photoresist was spun with the same process in 3.1.4 on both side (Figure 3.9 (a)). The Cr/Au layer is then patterned using etchant of each metal (Figure 3.9 (b)). After descuming for 3 minutes with 80 W oxygen plasma, 300 μm width × 50 μm depth of big channel was etched in 49% HF (hydrofluoric acid) for 7 minutes (Figure 3.9 (c)) and 9260 photoresist was removed in PRS 2000 (Figure 3.9 (d)). Figure 3.10 shows etch ratio of glass by wet-etch in 49% HF with time. The floor of PDMS membrane needs to be flat for imaging; the electrolyte channel also must a have uniform height (5 μm from the glass substrate). Therefore, the 50 μm depth big channel is

required to be filled flat, so that the later 5 μm sacrificial photoresist for electrolyte channel can make the uniform height; 1827 photoresist was applied on the etched big channel enough to fill up.
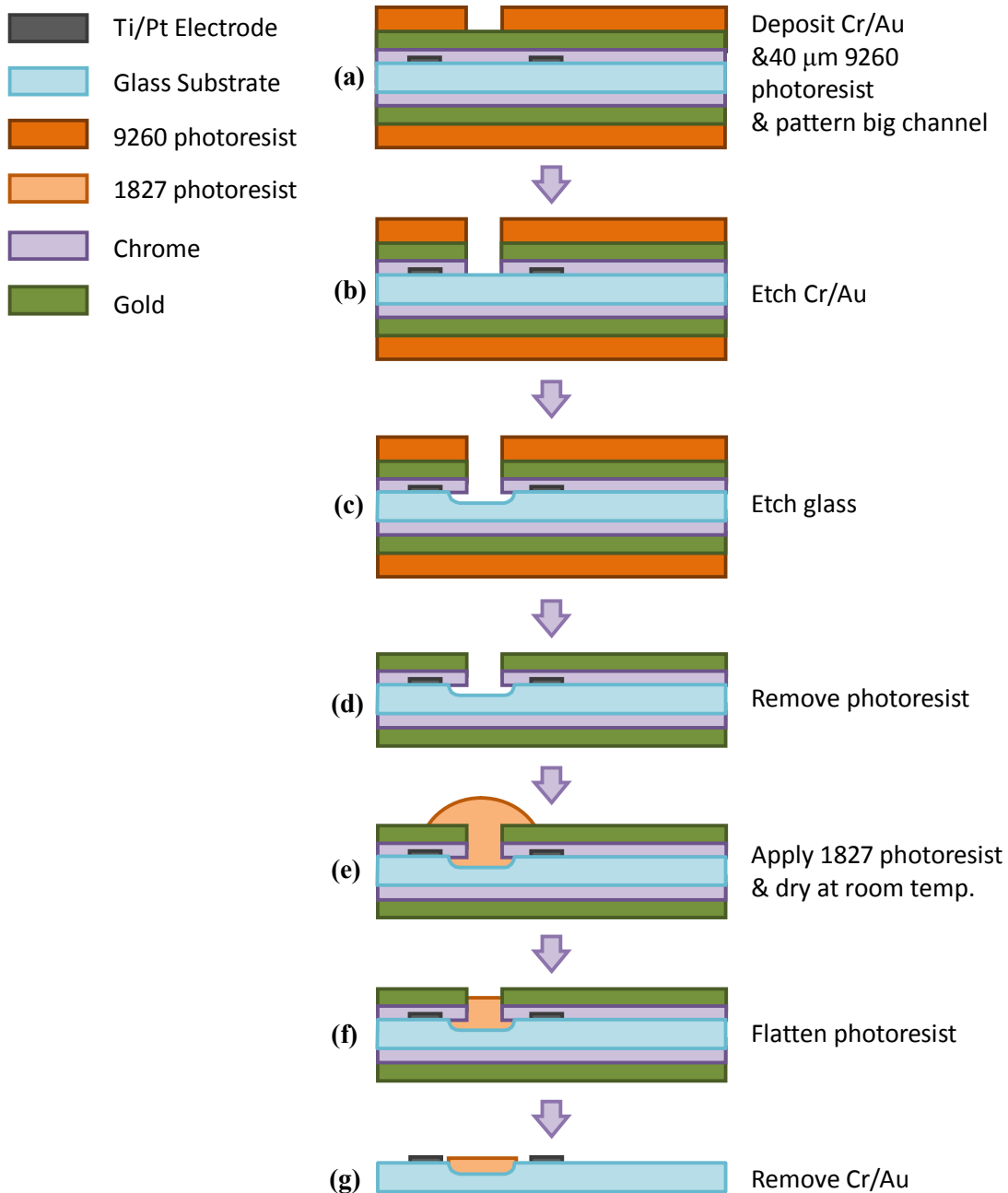
Figure 3.9 Glass etch and photoresist filling process for big channel.

The photoresist was dried in air-vented place with room temperature for 5 days to evaporate solvent (Figure 3.9 (e)). Excessive photoresist was flattened followed by descuming with oxygen plasma (Figure 3.9 (f)). Lastly, sacrificial Cr/Au layers were removed (Figure 3.9 (f)). Remaining process continues from electrolyte layer patterning as described from section 3.1.2. This version was used for our collaboration with Forbes lab (U. Mass., Amherst) as well as my experiments with myoblasts.
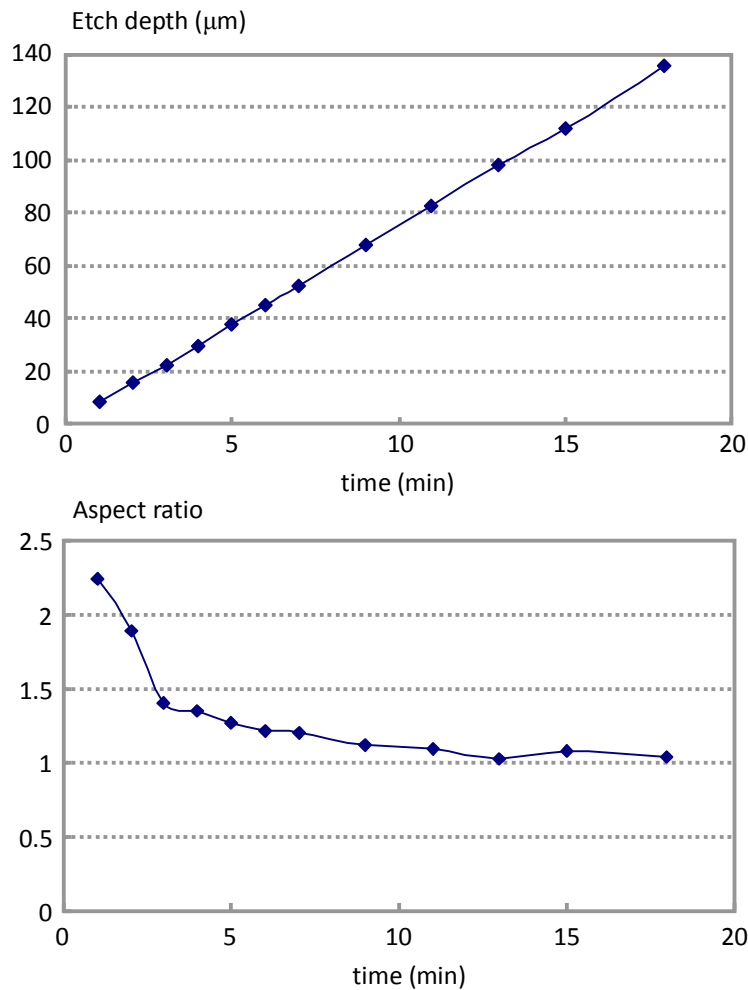
Figure 3.10 Isotropic wet-etch of glass in HF.

(a) Etch depth, and **(b)** aspect ratio (sidewall etch divided by etch depth) with time. More than 17 minutes of etch generated damage to the photoresist and metal layer.

3.4 Six Inch Wafer Process in Berkeley Microlab

Six inch glass wafer was introduced to fabricate the point source microgradient chip (in section 3.3.2) in the Berkeley Microlab. Chemicals and facilities to produce the same chip are different from those in the University of Michigan.

3.4.1 Wafer Cleaning and Electrode Patterning

500 μm thick, 6" Pyrex glass substrate was cleaned in Piranha for 10 minutes followed by a rinse-dry cycle in the Spin Rinse Dryer, then immersed into 10:1 diluted BHF for 5 minutes. After coating HMDS in the Primeoven, 1.3 μm G-line photoresist was spun on the clean substrate at 5000 rpm for 30 seconds, pre-baked at 90 °C hot plate for 60 seconds. The glass substrate is then UV-exposed with 0.14 Joule/cm^2 in the Ksaligner. 1.1 μm I-line photoresist was spin-coated at 4100 rpm, then baked at 90 °C hot plate for 60 seconds. The bi-layer photoresists on the substrate were exposed in the Ksaligner, aligning with a chrome mask patterned electrode design. OPD 4262 developer was used to dissolve UV-exposed photoresist. A descum was performed for 3 minutes with 50 W oxygen plasma (Technics-C) to remove residual photoresist around the electrode pattern. Titanium (Ti, 500 Å) and platinum (Pt, 1000 Å) were deposited using evaporation (Edwardseb3). Electrodes were patterned using lift-off process, with sonication in acetone for 20 minutes. To remove residual metal particles stuck on a surface while rinsing, DI water-jet spray was applied for 5 minutes.

3.4.2 Patterning Electrolyte Channel Layer

After HMDS coat in the Primeoven, 5 μm 1827 photoresist was spun on the electrode-patterned substrate at 1200 rpm for 30 seconds, and pre-baked at 100 °C hot plate for 50

seconds. Channel patterns were exposed in the Ksaligner using a channel-patterned mask and developed for 2 minutes in MF-319. Oxygen plasma treatment was followed with the Technics-C to enhance adhesion of PDMS to the substrate as well as descuming the photoresist residue. PDMS (Sylgard 184, Dow Corning) was prepared by mixing in a 10:1 ratio of base and curing agent, spun on the substrate with 10 μm thickness, followed by allowing the PDMS to flow and flatten the surface for 10 minutes. The PDMS was then cured for 15 minute on 110 °C hot plate.

3.4.3 Glass Etch for Patterning Big Channel

After patterning electrodes, 1000 Å Cr / 5000 Å Au were deposited by evaporation on both side in the Edwardseb3. 40 μm SPR-220 photoresist was spun. The Cr/Au layer was then patterned using etchant of each metal. After descuming for 3 minutes with 50 W oxygen plasma, 300 μm width × 50 μm depth of big channel was etched in 49% HF (hydrofluoric acid) for 7 minutes and the photoresist was removed in MF-26A. The substrate was then diced into 6 mm × 18 mm chips with the Esec 8003 Dicing Saw. Remaining steps are the same as in section 3.1.3 - 3.1.6.

3.5 Simple Oxygen Concentration Gradient Chip

As stated in section 2.4.3, this simple microgradient chip has several advantages compared to the OMA. First, substrate for cell culture area was fabricated with a cut piece of culture dish, providing the same adhesive condition with conventional *in vitro* experiment. Second, fabrication does not involve complicated process (no use of microfabrication facilities). Third, multiple chips can be used due to no wires for electric connection and decreased size. Ease of

fabrication and simultaneous operation would make suitable for use in optimization experiment requiring various conditions in series or in duplicates.

To fabricate the device, a cured piece of PDMS (Sylgard 184, Dow Corning) having 1 mm width × 2 mm height was placed on a 500 μm slit between cut pieces of culture dish (Falcon 3003, Fisher Scientific) using 734 RTV silicone glue. 150 μm thickness of glass slides were attached under the dish pieces using minimal amount of PDMS as a glue. The PDMS glue was then cured on 70 °C hot plate for 2 hours. Those glass slides prevent upward diffusion of atmospheric oxygen through the dish piece. After assembling a 5 mm × 7 mm area and 2 mm height culture chamber with polystyrene pieces using 734 RTV silicone glue, several completed chips were assembled on the open bottom of a gas-control chamber (Figure 3.11 (a), (b). See also Figure 3.13 (d)).

A needle-type, 50 μm tip fiber-optic oxygen probe (501656, World Precision Instruments) was also employed to measure oxygen level on the culture floor of the chip. The fiber-optic probe is connected to PC via sensor module (OXY-MICRO-AOT) and oxygen profile is monitored on screen. Compared to the fluorophore membrane used in OMA, it would not be suitable for sensing complex shape of spatial gradient and positioning of the sensor needs to be treated very carefully due to its fragile tip. The gas-control chamber and the chip were UV-sterilized for 1 hour, and then the culture area was coated with collagen (same procedure with dish control, see section 4.2.5) prior to operation. Because the gas-control chamber is placed inside 37 °C incubator (20% atmospheric O_2 + 5% CO_2), oxygen diffuses through the PDMS piece and generates a gradient across cell culture area. Measured oxygen level using the oxygen probe and closely matched to simulation (Figure 3.11 (c), (d)).
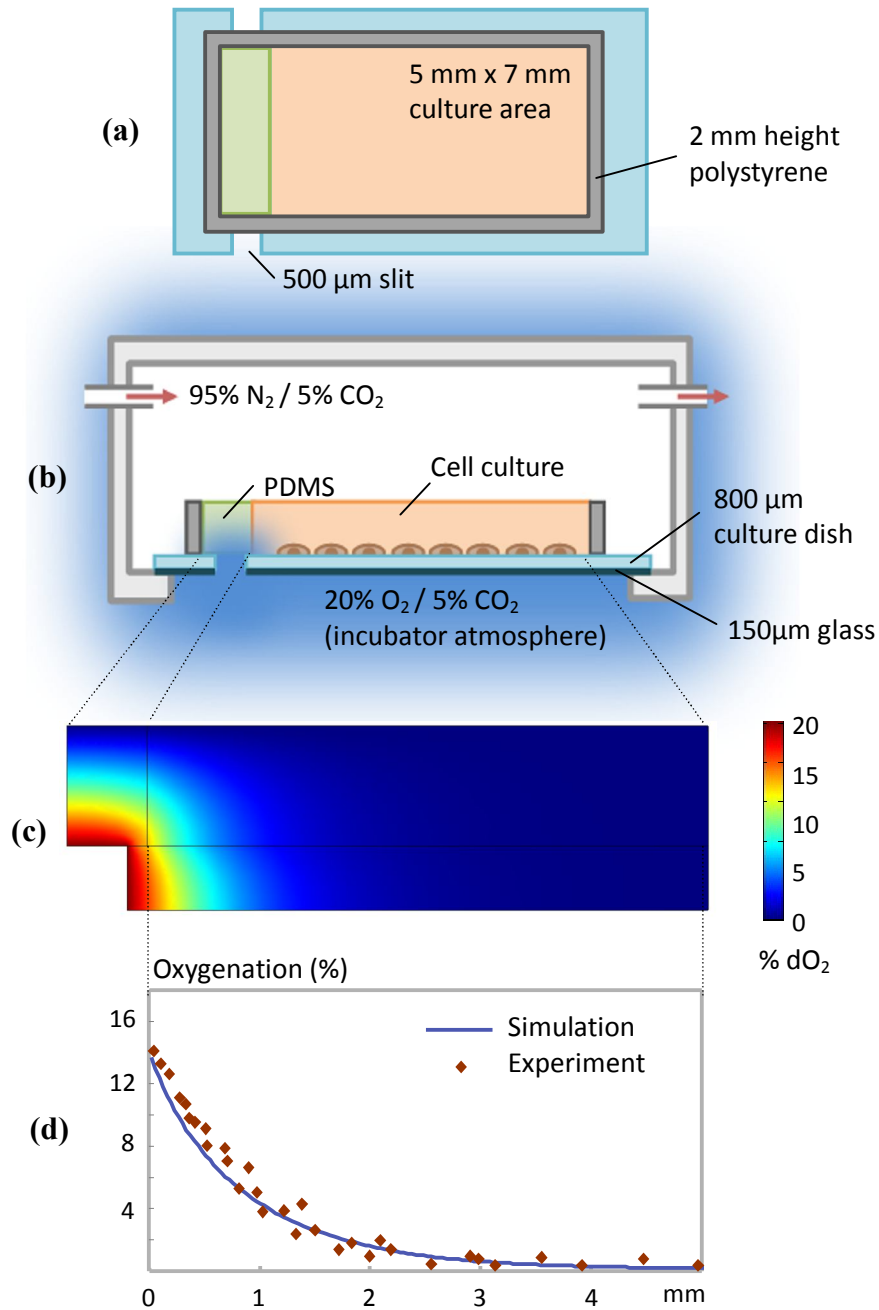
Figure 3.11 Simple oxygen gradient chip utilizing atmospheric oxygen.

(a) Top view of the chip. **(b)** Schematic illustration with gas-control enclosure. **(c)** Gradient formation simulated by COMSOL[TM]. **(d)** Measured and simulated gradient across the culture area.

3.6 Gas-Control Chamber

The OMA needs to be enclosed by anoxic gas condition (0% O_2), so that all the oxygen entering the cell culture is generated by electrolysis. The anoxic ambient presented around the chip acts as a constant oxygen sink. These boundary conditions lead to a sharp fall-off of oxygen concentration away from the oxygen-generating microelectrode (see Figure 2.7 (b)). Various types of gas-control chamber were developed. Experiments in section 3.7 employed a custom-made transparent headspace (Figure 3.12), which permits continuous microscopy of the chip while purging the exterior with a defined atmosphere (e.g. 100% N_2).
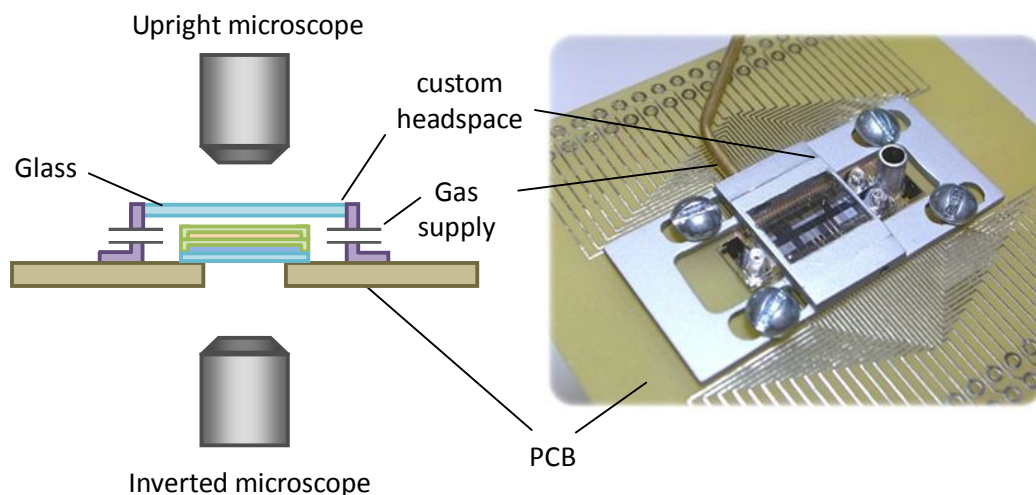
Figure 3.12 Custom headspace mounted to the chip and PCB.

Top of the headspace is covered with a glass cover-slip, allowing either upright or inverted microscopy.

Using the tiny headspace, however, is not suitable for long period of cell culture experiments; the purging gas causes removal of humidity around OMA and evaporation of culture medium eventually unless a special humidifier (e.g. a bubbler) is connected ahead the gas-control

headspace. Moreover, in order to maintain 37 °C environment for mammalian cells, the gas-control chamber (115 mm × 65 mm × 54 mm, PN-1322-C NEMA 4X, Bud Industries) was placed in a culture incubator; tight sealing of the chamber is needed not to lower the oxygen level in the incubator caused by leaked anoxic gas during the purging.
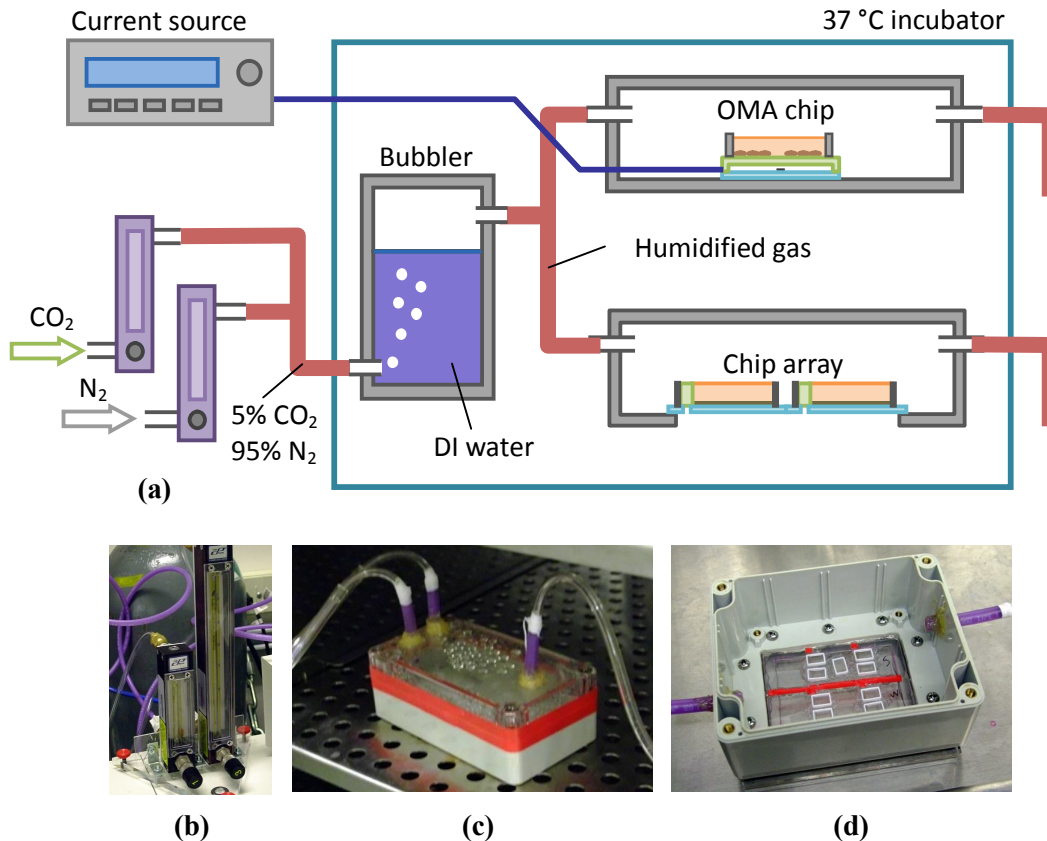
Figure 3.13 Experimental setup with gas-control system and 37 °C incubator for mammalian cell culture.

(a) Controlled gas mixture passes the bubbler inside 37 °C incubator to purge the gas-control box without evaporation of culture medium. **(b)** Flowmeters for CO_2 and N_2. **(c)** Gas bubbler inside the incubator. **(d)** A gas-control box with multiple simple gradient chips shown in section 3.5.

Figure 3.13 (a) illustrates experimental setup for mammalian cell culture including gas-control chamber. Mixed gas (5% CO_2 and 95% N_2), is humidified while passing a bubbler chamber, and continuously purges the gas-control chamber including OMA or simple gradient chips. Each CO_2 and N_2 gas is controlled by flowmeters (C-32048-07 for CO_2, C-32048-63 for N_2, Cole-Parmer) with flow rate of 5 mL/min and 95 mL/min, respectively. Note that bottom side of the gas-control box was replaced with transparent glass pieces for microscopy. An anaerobic sachet (AnaeroGen, AN0010C, Oxoid) replacing complex gas-supply system (which reduces atmospheric oxygen to below 1% and generates CO_2 to between 9 − 13%) was used with a custom-made chamber for section 4.1.3.

3.7 Microgradient Measurement

First part of this section demonstrates temporal modification of the microgradient profile during an experiment. Experimental measurement of various gradient profiles verifies the measured profile closely matches simulation result. Hydrogen peroxide generated during electrolysis as a by-product is also quantified and discussed.

For visualization of dynamic change of microgradient (section 3.7.1), resazurin redox indicator solution was made by mixing 5 : 5 : 1 of 1 M NaOH : 0.3 M glucose : 0.1% resazurin. Concentration of the resazurin was maximized to achieve highest color contrast since the cell culture chamber where resazurin solution is loaded has only 150μm height. Resazurin first undergoes an irreversible transition from blue to colorless (resazurin to resorufin); this occurred over ~2 minutes in a beaker subsequent to mixing.

(a)   **(b)**
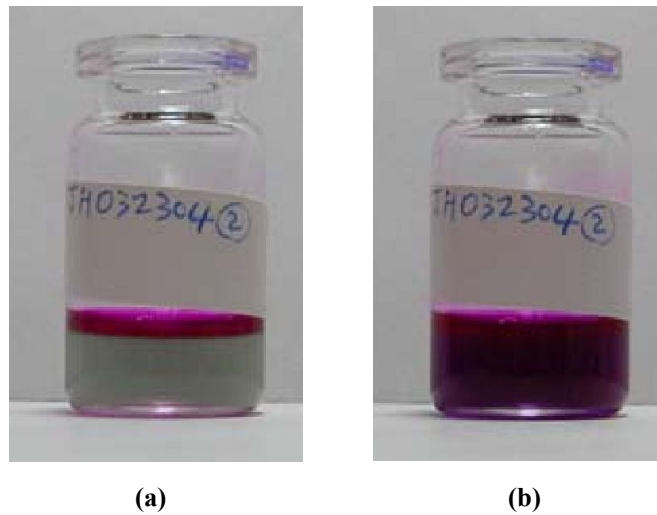
Figure 3.14 Color change of resazurin by oxygenation.

(a) Before shaking the bottle. Colorized only the surface where oxygen can reach and react. **(b)** After shaking, whole solution turned color to purple.

The colorless solution was loaded into the chip for experimentation, and then the chip was purged with anoxic gas; in the presence of oxygen, resorufin is reversibly changed into dehydroresorufin which is purple red as in Figure 3.14. Video data were captured using a color CCD camera connected on a white light microscope column and video capture software.

A laminated, oxygen-sensitive fluorophore membrane was employed to quantify the oxygen microgradients generated by the OMA (section 3.7.2). Essentially, the membrane measured the oxygen gradient present across the 'floor' of the cell culture chamber. This film was obtained pre-spun from Oxysense, Inc. as a proprietary product under a special agreement. Processes for making such films have been extensively published [84][85][86][87]. The emitted light intensity under fluorescent excitation decreases linearly with the amount of oxygen in the membrane

[84][85]. The oxygen-sensitive membrane intensity response was obtained with two-point calibration images (0% and 20% O_2) by purging outside of the chip with anoxic gas mixture for 10 minutes using a custom-headspace and then taking an image. Images were acquired at 50× magnification at a resolution of 480 × 480 pixels (corresponding to a ~1 mm × 1 mm field). Fluorescent microscopy of the film employed custom filter cubes (DM : 505 / EX : 460−500 / BA : 510−560), and upright fluorescent microscopy was performed with a 5.1 mega-pixel Digital CCD Color Camera. Various electrode configurations were designed to measure and compare generated oxygen microgradients with finite element diffusion simulations (see section 2.5).

Amplex Red solution (Amplex Red Hydrogen Peroxide/Peroxidase Assay Kit, A22188, Molecular Probes) was prepared according to the manufacturer's instructions for the peroxide detection (section 3.7.3). Solutions with 0 and 10 μM H_2O_2 were prepared and loaded into chips for a two-point calibration of the fluorescent intensity response as a function of H_2O_2 concentration. Images were acquired and processed as for the fluorescent membrane sensor described above. G-2A filter cube (having close to the spectra of resorufin (EX : 571 / EM : 585)) was used with inverted microscopy. The resultant concentration vs. time data were compared with results from 2-D FEM diffusion/kinetic simulations of the device and the Amplex Red system to determine what fraction of the current through the electrodes was required to generate the measured concentration change (section 2.3).

All image analysis was done on Matlab[TM] software with custom codes (shown below). Since the fluorescent intensity of the oxygen-sensitive membrane is linearly decreased by the oxygen level, the gradient in the image can be calculated with two-point calibration images at 0% and 20% O_2. To obtain cross-sectional intensity plot, five pixels were averaged above and below the cross-section in question. This was also done to the calibration images.

< Matlab^{TM} custom code for microgradient quantification>

```matlab
%import 480 x 5 pixel RGB images shwowing area across the microgradient
im_anoxic=imread('anoxic.bmp'); %image after nitrogen purging
im_normoxic=imread('normoxic.bmp'); %image before nitrogen purging
im_gradient=imread('1uA.bmp'); %image after microgradient constrcution


% get only red intensity among RGB
im_anoxic=im_anoxic(:,:,1); im_normoxic=im_normoxic(:,:,1); im_gradient=im_gradient(:,:,1);


% convert the intensity to double precision
im_anoxic=im2double(im_anoxic);
im_normoxic=im2double(im_normoxic);
im_gradient=im2double(im_gradient);


% get O2 (%) from two point calibration
num=imabsdiff(im_anoxic,im_gradient); den=imabsdiff(im_anoxic,im_normoxic);
O2_percentage=num./den.*21;


% get average value along 5 pixel width
O2_percentage_mean=mean(O2_percentage,2);


% unit converstion from pixel to mm. % 1 mm corresponds to 520 pixel of the image.
% therefore, 480 pixel corresponds to 0.923 mm
x_value=0.923/480:0.923/480:0.923;
plot(x_value, O2_percentage_mean) % plot
```

3.7.1 Dynamic Change Visualization

A redox indicator, resazurin was loaded into cell culture chamber to visualize the generated dissolved oxygen, and the chip was mounted with a custom-made transparent headspace as described in section 3.6. Figure 3.15 shows how the oxygen doses could be localized and manipulated using ten horizontal microelectrodes (each 20 μm × 1 mm). Different electrodes

were turned on and off in sequence; the arrow in every frame indicates which of the ten microelectrodes is running current in that image. Since the electrodes are long and thin, the microgradient is essentially one-dimensional. Video-capture frames are 20 seconds apart, thus showing that microgradient construction and modification can be achieved within 1 minute.
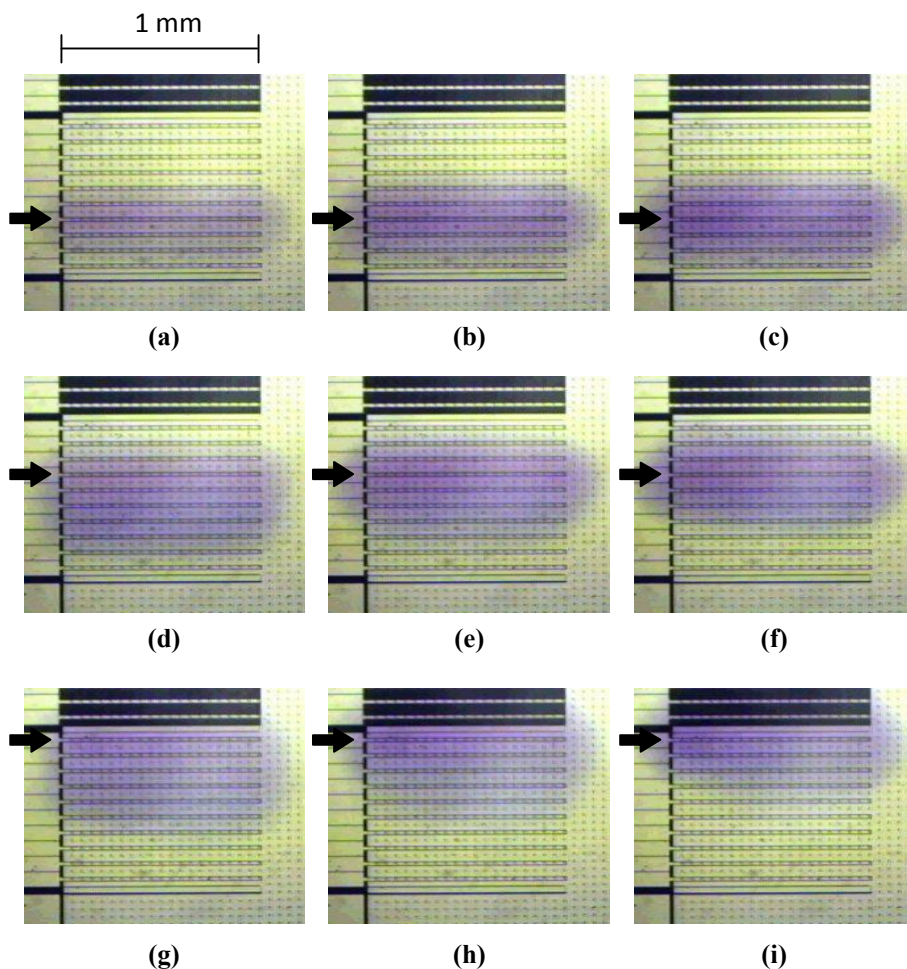
Figure 3.15 Time-lapse white-light images of patterned oxygen microgradient.

3.7.2 Microgradient Quantification

Figure 3.16 shows examples of electrode geometries that generated 1-D and 2-D microgradients.

66
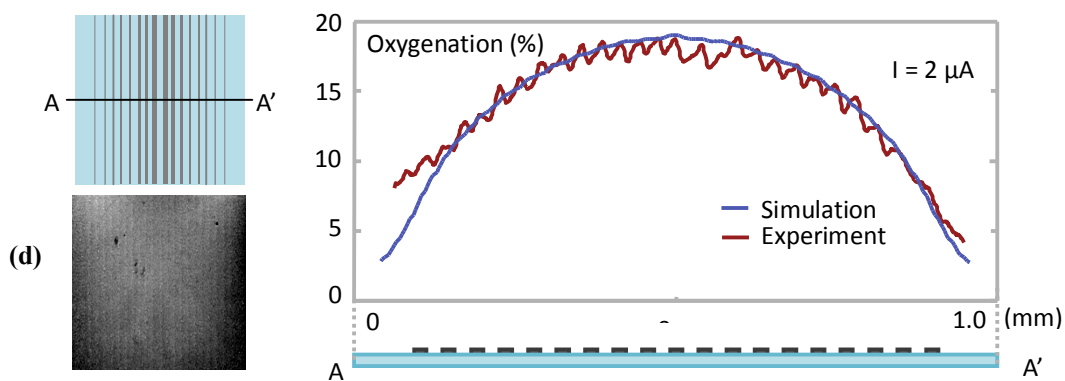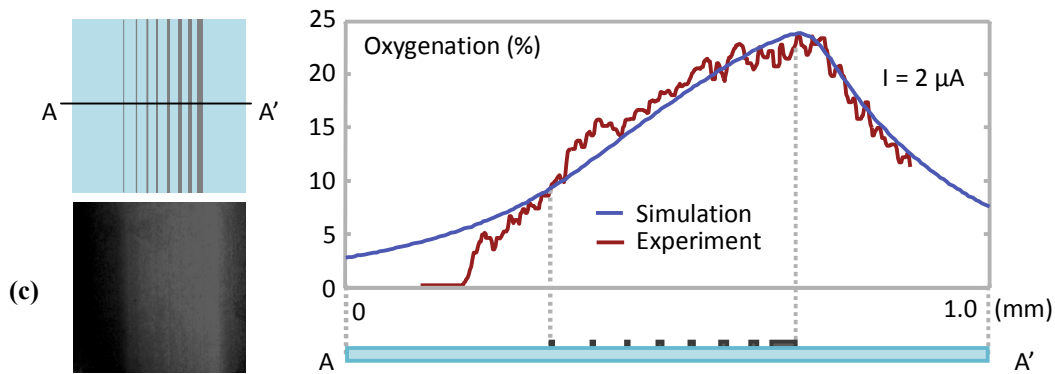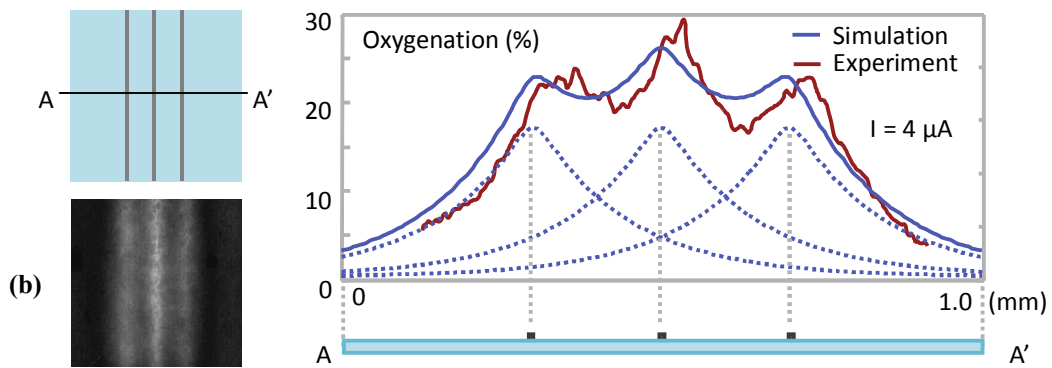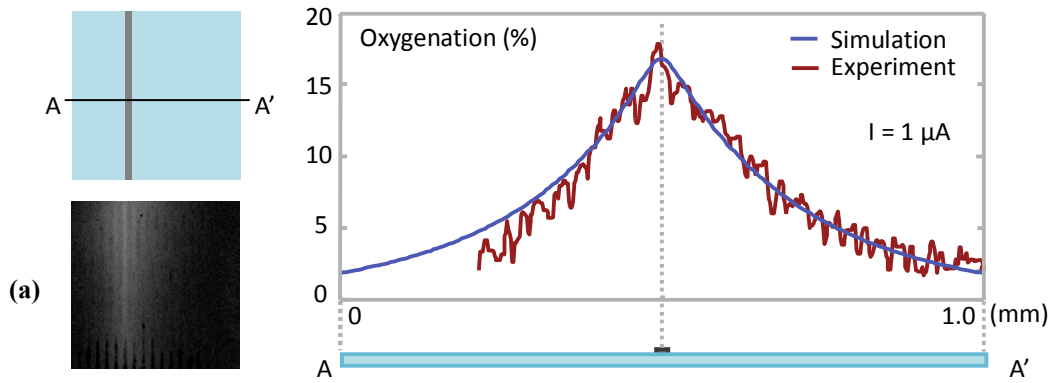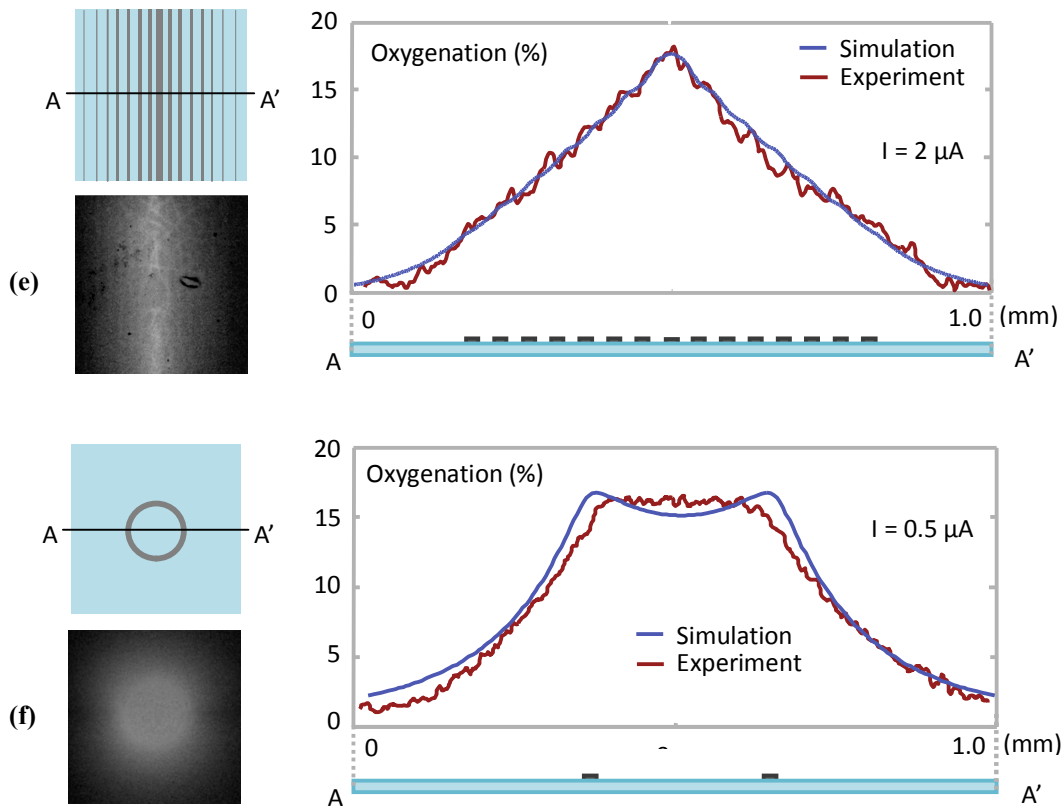
Figure 3.16 Microgradients generated by various electrode arrays.

(Top left) Top-view of electrode design; gray lines indicate electrode geometry. *(Bottom left)* Fluorescent images (light intensity inverted) captured with sensor membrane. *(Right column)* Simulated and measured profiles at cross-section A-A' of **(a)** sharp microgradient with single electrode, **(b)** 3 electrodes with 200 μm spacing (individual electrode gradients are shown with dashed lines), **(c)** linear gradient with 8 electrodes, **(d)** half-circle gradient with 21 electrodes, **(e)** triangular gradient with 15 electrodes, and **(f)** ring flat gradient with ring shape electrode.

An array of long, thin electrodes (such as the one in the Figure 3.5 (b) and Figure 3.15) generated an approximately one-dimensional oxygen microgradient except near the edges of

the array. Data from this array could thus be compared with 2-D FEM diffusion simulations.

Figure 3.16 (a) shows a comparison of measured and simulated gradients generated by a single, long electrode in the ten electrode array. By varying the generated oxygen through an array of evenly-spaced electrodes, many such oxygen 'peaks' were superimposed to construct microgradients with arbitrary profiles. Figure 3.16 (b) − (f) shows measured and simulated results for an array of electrodes generating other microgradient profiles.

Geometry data of the microgradient designs in Figure 3.16 are listed in Table 3.1. The origin of each design is taken to be at the center of the figures referenced.

Table 3.1 Coordinates of the electrode center and electrode width for designs presented in this thesis.

Design	Electrode center (µm)			Electrode width (µm)		
Figure 3.16 (a)	0.0			20.0		
Figure 3.16 (b)	0.0,	200.0,	400.0	20.0,	20.0,	20.0
Figure 3.16 (c)	−130.5,	−72.5,	−17.5,	3.0,	5.0,	7.0,
	38.0,	90.5,	142.0,	8.0,	9.0,	10.0,
	192.5,	227.5		15.0,	41.0	
Figure 3.16 (d)	−427.0,	−384.5,	−339.5,	20.0,	27.0,	25.0,
	−295.0,	−252.5,	−209.5,	26.0,	27.0,	27.0,
	−167.5,	−126.5,	−86.0,	27.0,	27.0,	28.0,
	−47.5,	0.0,	47.5,	25.0,	40.0,	25.0,
	86.0,	126.5,	167.5,	28.0,	27.0,	27.0,
	209.5,	252.5,	295,	27.0,	27.0,	26.0,
	339.5,	384.5,	427.0	25.0,	27.0,	20.0
Figure 3.16 (e)	−358.0,	−300.1,	−245.0,	3.0,	5.1,	6.9,
	−190.0,	−137.1,	−85.8,	8.1,	9.2,	10.6,
	−35.2,	0.0,	35.2,	13.4,	41,	13.4,
	85.8,	137.1,	190.0,	10.6,	9.2,	8.1,
	245.0,	300.1,	358.0	6.9,	5.1,	3.0
Figure 3.16 (f)	150.0			20.0		
Figure 4.1	0.0,	35.2,	85.8,	41.0,	13.4,	10.6,
	137.1,	190.0,	245.0,	9.2,	8.1,	6.9,
	300.1,	358.0		5.1,	3.0	

3.7.3 Hydrogen Peroxide Generation

Of particular interest was the generation of hydrogen peroxide, a highly potent ROS with well-studied effects on cell cycle and differentiation as mentioned in section 2.2.2. Since the anode and cathode were not separated by an ion-exchange membrane but simply resided at

some distance from each other in the same liquid electrolyte, there exists the possibility of hydrogen peroxide generation at the cathode. It is thus important to quantify the fraction of current generating hydrogen peroxide rather than oxygen. Amplex Red indicator was loaded into the cell culture chamber and the fluorescence intensity monitored over two hours while applying a current through the OMA. In Figure 3.17, the hydrogen peroxide was accumulated with 20 μM in every hour, and was not localized around the anodes and increased homogeneously throughout the entire cell culture area. This fact indicates it was likely generated by the large cathode and gradually diffused over the whole culture area. A hydrogen peroxide flux of 2.2×10^{11} molecules H_2O_2/mm^2s were required to generate the measured concentration change. During the experiment, 10 μA/mm^2 of current ran constantly through the electrode used in Figure 4.1, corresponding to a flux of 3.13×10^{13} electrons/mm^{2}s. Assuming the peroxide reaction involved a two-electron transfer (reaction (2.8)), less than 1.4% of the total current went towards hydrogen peroxide generation. H_2O_2-eliminating activity in various cells has been reported, half-life of hydrogen peroxide is less than 20 minutes in cell and medium [88]. The level of hydrogen peroxide generation can be increased or reduced by 1) adjusting the pH of the electrolyte (since production is favored in acidic environments), or 2) altering the separation between cathode and anode with distance or membranes [37].
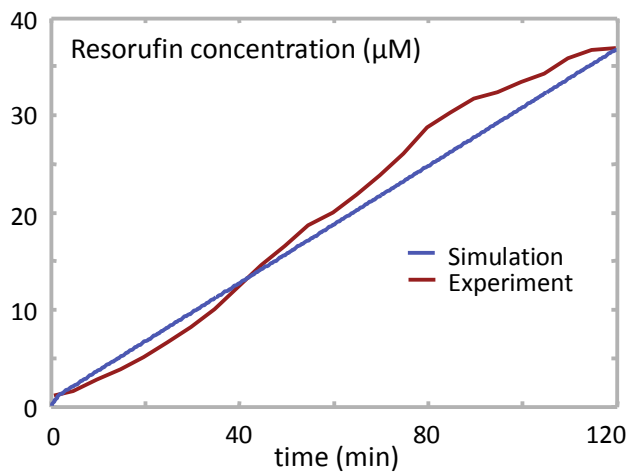
Figure 3.17 Plot of resorufin concentration vs. time.

Chapter 4

Cell Culture Results

4.1 Initial Biological Experiments

Three initial culture experiments were demonstrated for verification of the microsystem as a possible bio-application. Two different cell lines were used to characterize the device: murine C2C12 myoblasts and suspensions of *Bacillus subtilis* bacteria. C2C12 myoblasts, isolated in the 1970s from muscle of mouse [89], have been often used to study differentiation of myoblasts. C2C12 myoblasts were used to characterize the device due to their known response to the oxygen environment. Recent research has shown that the oxygen environment is a strong regulator for apoptosis, differentiation and metabolism in C2C12 [39][40][90][91][92][93]. We also used this cell line to observe calcium-release from re-oxygenation following ischemia, a topic of much current interest [94][95]. A different set of experiments was carried out using *Bacillus subtilis*, an obligate bacterial aerobe. This bacterium is a model organism in aerotaxis, oxygen-sensing and motility studies in prokaryotes [96].

4.1.1 C2C12 Myoblasts under Hyperoxia

C2C12 cells were used to validate the presence of oxygen gradients due to their well-known sensitivity to the oxygen environment. C2C12 myoblast cells were maintained in 100 mm culture dishes (Falcon 3003, Fisher Scientific) in GM, composed of 83% DMEM (11965, Gibco), 1% GlutaMAX (61965-026, Gibco), 1% penicillin/streptomycin (30-004-Cl, Cellgro) and 15% FBS (26140, Gibco), in an incubator with atmosphere of 20% O_2 and 5% CO_2 at 37 °C. To take cells from plates, 2 mL of 0.25% trypsin-EDTA (25200-106, Invitrogen) was applied for 30 seconds. Trypsinized cells were detached from the plate surface and allowed for collection. The detached cells were centrifuged for one minute at 1000 rpm, supernatants were removed and cells were re-suspended in GM with desired cell density. Cells in GM were transferred into the chip and allowed to be grown. After 2 hours, current was applied to electrodes to observe apoptosis by hyper-oxygenation on the cells. To visualize apoptotic cells, LIVE/DEAD (BacLightTM Bacterial Viability Kit, L13152, Molecular Probes) was used to stain the C2C12 myoblasts. All aliquot preparations followed the standard procedure in the product manual. After removing medium in the culture, indicator solution is loaded and incubated for 15 minutes at room temperature prior to taking images. G-2A (DM : 565 LP / EX : 510 − 560 / BA : 590 LP) and B-2A (DM : 500 LP / EX : 450 − 490 / BA : 515 LP) Nikon filter cubes with inverted microscopy were used for apoptotic and non-apoptotic cells, respectively.
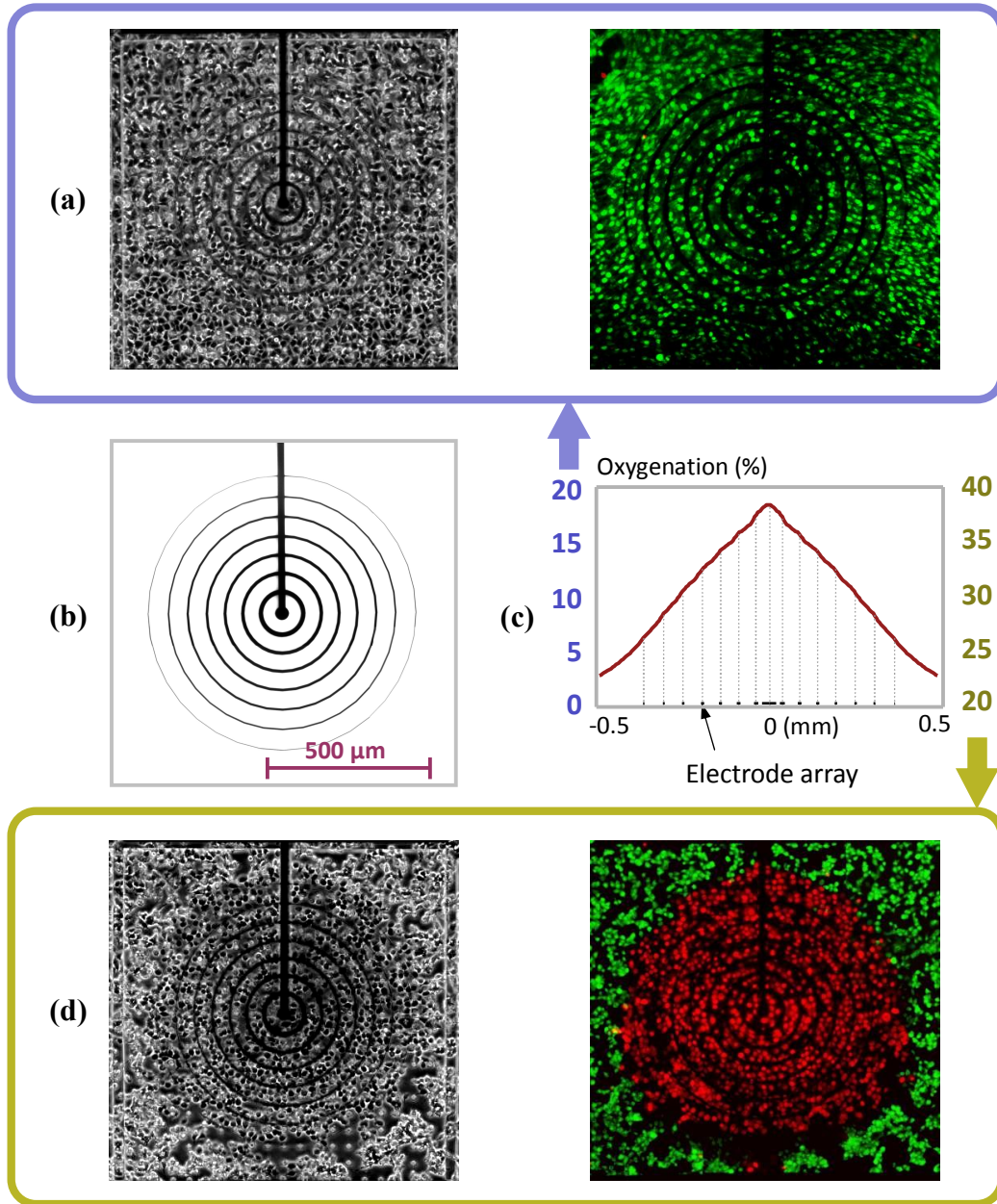
Figure 4.1 Hyperoxia induced apoptosis in C2C12 myoblasts.

(a) Whitelight and LIVE/DEAD image of myoblasts in anaerobic chamber, with 20% dO$_2$ peak. **(b)** Electrode array making a linear, cone-shaped profile. **(c)** Oxygenation plot under hypoxic (left, blue) and normoxic (right, yellow) condition outside. **(d)** Whitelight and LIVE/DEAD image with 40% dO$_2$ peak.

Figure 4.1 shows the result of the experiment. External environmental conditions were maintained at 20% atmospheric O_2, 5% CO_2 and 37 °C. For an input current density of 10 $\mu A/mm^2$, simulations showed the patterned microgradient had an oxygen concentration maximum of ~ 40% and decreased linearly (Figure 4.1 (c)). Within 2 − 4 hours of current application, cells in oxygen-rich areas took on a well-defined spherical shape and contracted from the surface (Figure 4.1 (d), left). When stained with LIVE/DEAD, the spherical, contracted cells stained red in a well-defined area corresponding to the hyper-oxygenated region generated by the microelectrodes (Figure 4.1 (d), right). We interpreted this to be an induction of apoptosis. This patterning of apoptosis was repeatable across all experiments and always coincided with areas with a highly oxygenated environment. Apoptosis always began at the center after 2 hours and expanded to the edge of the ring after another 1 − 2 hours. The boundary of apoptosis always coincided with the 25 − 28% oxygen region (Figure 4.1 (c)). Note that this experiment was carried out in a 20% O_2 ambient so that the electrodes raise the oxygen concentration above this baseline.

As a control, devices with applied potential but no electrolyte and devices with electrolyte but no applied potential showed no effect on normal cell growth over a 12 − 18 hours of culture. To show that cells could be grown for extended periods of time with oxygen from the microelectrodes without suffering deleterious effects, C2C12 myoblasts were grown in the same medium on the same electrode design with the same current density in an anoxic chamber (95% N_2 / 5% CO_2); these cultures grew normally for 3 days with no evidence of apoptosis (Figure 4.1 (a)). Cells in these conditions grew to confluence at the same rate as cells grown in plates. All experiments were repeated at least three times.

4.1.2 Calcium Release during Localized Re-oxygenation

To illustrate the ability for the OMA to control oxygen levels with time, we chose to examine calcium-release during simulated ischemia (i.e. *in vitro* hypoxia) followed by rapid, localized re-oxygenation. Hypoxia followed by rapid re-oxygenation of entire culture plates is frequently employed as an *in vitro* model of ischemia/re-oxygenation injury and is the topic of much current research. Specifically, cytosolic calcium levels are known to increase drastically with re-oxygenation following ischemia. However, the molecular details of oxygen sensitivity, the exact mechanism of injury and its links to metabolism are still being elucidated [94][95]. This model is also useful as a test of O_2 (and not H_2O_2) generation because dosing cells with hydrogen peroxide has been shown to attenuate Ca^{2+} release during re-oxygenation [94].

C2C12 myoblasts were cultured in OMA for 24 hours in an anoxic chamber (95% N_2, 5% CO_2) with no oxygen input from our device. Cells grew normally with expected undifferentiated morphology. At this point, the medium was replaced with a buffer containing the calcium indicator and re-introduced into the anoxic chamber for 45 minutes. A Ca^{2+}-sensitive fluorescent indicator (Fluo-4 NW Calcium Assay Kit (F36206), Molecular Probes, Inc.) was used to detect Ca^{2+} release during the oxygen generation. The indicator solution was prepared according to the manufacturer's instructions for adherent cells and loaded into chips after carefully removing the GM from the cell culture. The chip was then cured in a 37 °C anoxic incubator 45 minutes before dosing with oxygen. Inverted microscopy was used without necessity of fluorescent excitation.
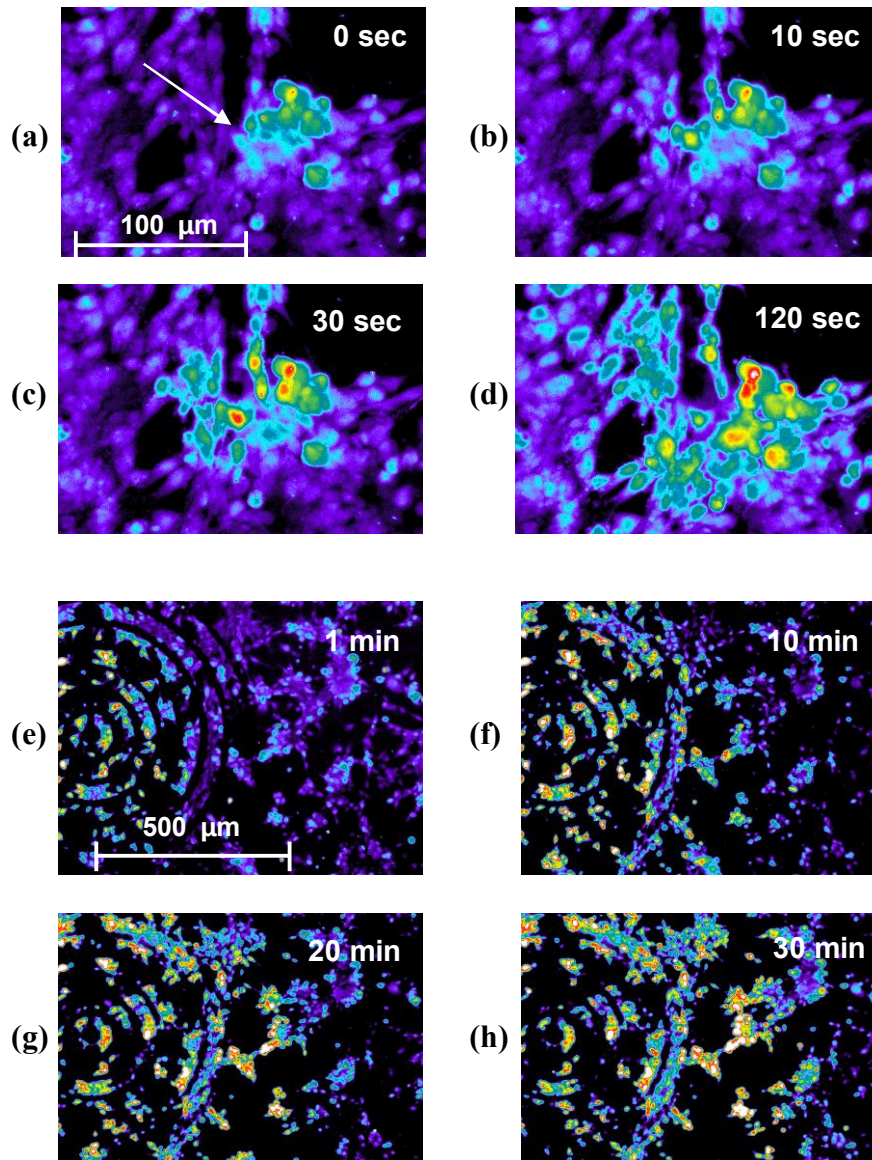
Figure 4.2 Pseudo-colored, time-lapse of fluorescence image of Ca^{2+} release.

(a)-(d) Ca^{2+} release by generated oxygen at a point source. Current density of 6.4 mA/mm^2 was applied. **(e)-(h)** While applying a continuous current density of 10 μA/mm^2 at cone-shaped electrode. Images were taken at the indicated times.

After 45 minutes, oxygen was introduced to the culture using one of our oxygen arrays.

Figure 4.2 (a) − (d) shows a time-sequence of oxygen-dependent calcium release near an oxygen-generating 10 μm diameter 'point-source' electrode. Note the spread of calcium-release and increase in intensity of the fluorescence (proportional to calcium concentration) beyond the area directly over the electrode. The oxygen-sensitive calcium levels can also be seen with arrays that generate larger, linearly decreasing gradients; Figure 4.2 (e) − (h) shows one such example. Again, note how calcium levels are proportionally lower for cells farther from the oxygen maxima and extend, as expected, beyond the microelectrode array. As a control, cells were grown as described, loaded with Fluo-4 NW, re-introduced into an anoxic chamber for 45 minutes, and then rapidly oxygenated *en masse* by purging the chip with atmospheric air (20% O_2). Observation over 30 minutes showed calcium levels across the chip were similar to those seen around electrodes. Had our electrode been introducing substantial hydrogen peroxide, we would expect the localized response to be significantly lower than the response from air purging [95].

4.1.3 Aerotaxis of Bacteria

Bacillus subtilis, a model obligatory aerobe, was employed to demonstrate dynamic aerotaxis assays driven by oxygen microgradients. Optical density at 600 nm (OD_{600}) was used to measure density of *Bacillus subtilis*. Bacterial suspension cultures (Ward's Natural Science) were grown in 50 mL aliquots in 150 mL shake flasks in LB medium at 28 °C on a 150 rpm shaker table, for 24 hours. This resulted in stationary phase cultures with $OD_{600} \sim 2$. The incubated culture was then diluted in LB to desired density. Suspensions were diluted to 0.5 OD_{600} in 1 mL, loaded into a microgradient chip and the device was quickly (~ 10 seconds) introduced into an anoxic chamber (100% N_2). After 30 − 45 minutes of expose to anoxic

condition, the bacteria became sluggish and moving speed was drastically reduced. Oxygen was introduced from OMA at this point. Aerotaxis assays could then be performed by locally dosing oxygen with the microelectrode array. For example, after 7 minutes of dosing oxygen from a single 10 μm diameter microelectrode at a current density of 6.4 mA/mm^2 (33 nmol O$_2$/mm^{2}s) bacteria self-assembled into the band shown in Figure 4.3 (a), (b). If this current density were maintained unchanged, the band could be maintained for up to 24 hours (beyond this, the band remained but medium depletion and/or waste product accumulation began to kill off bacteria). Once the initial band was formed, altering the input current density allowed the researcher to control the size of the band and observe the dynamic aerotaxis. For example, Figure 4.3 (c) − (f) shows the change in the band as the oxygen input is steadily decreased over 10 minutes. As the current decreases, the band tightens around the diminishing source; beyond a certain threshold (~ 1.2 mA/mm^2 or 6.6 nmol O$_2$/mm^{2}s) the band disperses and the suspension once again becomes homogenous. Such dynamic spatial response and sensitivity threshold experiments are impossible with current methods [96][97][98].
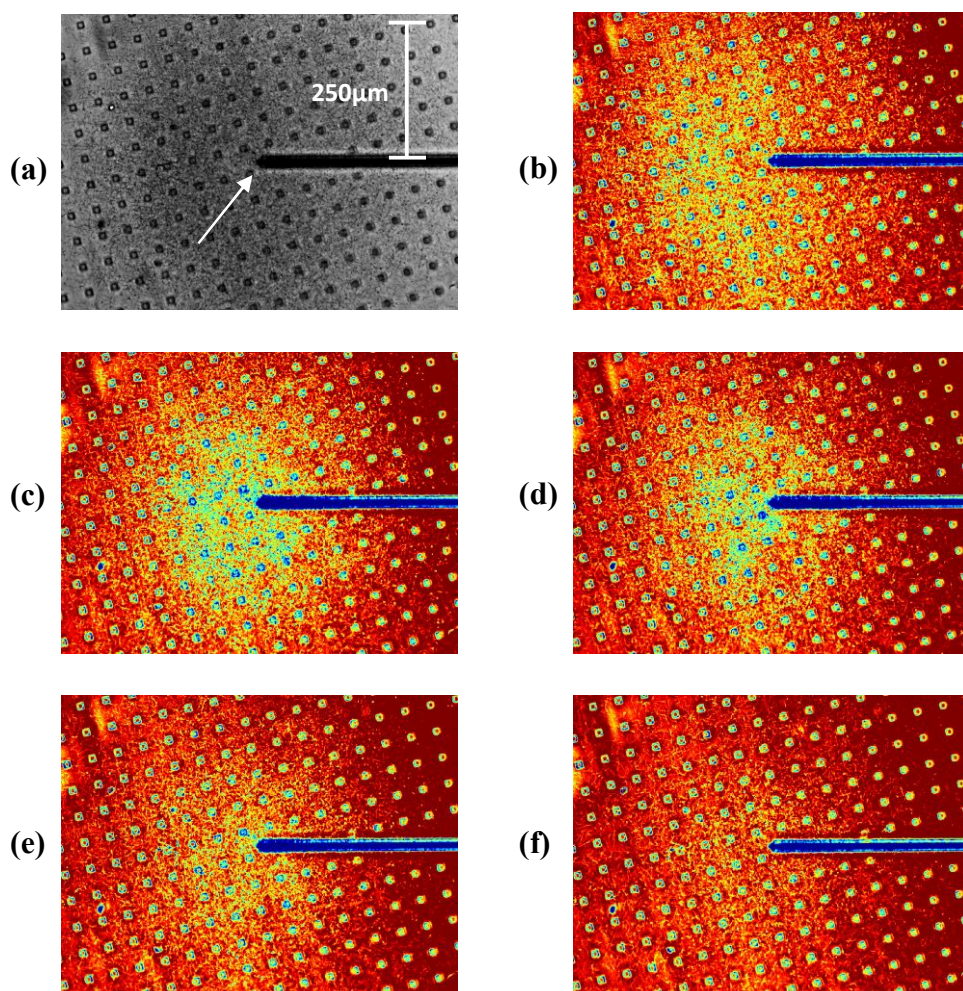
Figure 4.3 Bacterial aerotaxis toward oxygen-generating electrode.

The microelectrode is a 10 μm diameter circle at the center of the images (larger structure extending to right is buried and does not generate oxygen). **(a)** Differential Interference Contrast (DIC) microscopy of aerotactic band formation for a current density of 6.4 mA/mm^2. **(b)-(f)** Pseudo-color images of aerotactic band as current is decreased from 6.4 to 1.2 mA/mm^2. Note that (b) is pseudo-colored image of (a).

4.2 SOD1 Heterozygote Myoblasts

More research focuses on further quantification of a complete, biological question to answer the effects of microgradients generated by the oxygen microgradient system during cell culture. In this section, the effect of the oxygen concentration gradients to a specific cell type, related to decreased ability of detoxifying ROS, will be explored further. No clear mechanism has been verified for the relationship between SOD1 deficiency and oxygen level. Therefore, exploring the effect of SOD1-deficiency through oxygen level can provide important information in many clinical and biological researches. We initially propose hypotheses describing 1) the effect of oxygen stress on the SOD1-deficient heterozygote compared to wild-type myoblasts, and 2) whether cell-cell cytosolic exchange occurs under oxygen concentration gradient compared to discrete oxygen levels.

4.2.1 Sources and Cellular Effect of ROS

In section 2.2.2, the generation of ROS was discussed in the context of water electrolysis. During normal metabolism, cell produces ROS by-products from the oxidative metabolism inside the cell. The generated species are highly reactive free radicals generated by incomplete reduction of oxygen [99]. Approximately 1×10^{12} of O_2 molecules pass through each cell per day in our body, and 2% of them are converted to superoxide. Therefore, formation of ROS and their effect on cellular metabolism is of increasing interest in the biological community.

$O_2^{\bullet-}$

O_3 $^{\bullet}OH$

O_2

O^- H_2O_2

HOCl
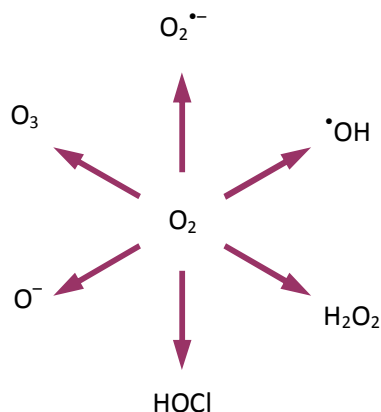
Figure 4.4 Reactive oxygen species generated from oxygen molecule

Various potential functions and sources of free radicals have been discussed since the free radical theory was proposed by Harman to investigate aging in 1950s [100]. Mitochondria are thought to be the primary sources of free radicals. Mitochondrial ROS are generated by oxidative phosphorylation which uses generated energy across inner mitochondrial membrane to produce ATP [101][102]. The respiratory chain of mitochondria is mainly composed of the mitochondrial oxidative phosphorylation system. Electrons leaked from several sites react with oxygen, and then free radicals are generated as by-products [103].

Non-mitochondiral ROS are also produced by cytosolic enzymes such as NADPH (reduced form of NADP) oxidase [104]. Various families of NADPH oxidase have been identified, Nox/Duox families are representative [105][106][107][108]. In contrast to mitochondrial ROS, those enzyme families generate superoxide anion with signal transduction pathways regulating NADPH oxidase activation [104] for the radicals to participate potential physiologic functions.

ROS generated by the Nox/Duox families also plays important roles in cellular metabolism as signaling molecules [109][110]. The metabolic ROS are known to affect growth and proliferation of cells [111][112], differentiation of stem cells [110][113], receptor signaling

[114], activation of apoptosis [115][116], cell senescence [117][118], and innate immune system [108][119] as shown in Figure 4.5.
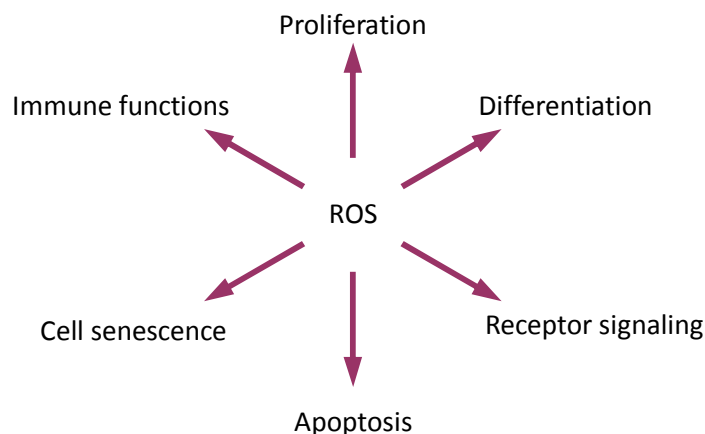
Figure 4.5 Reactive oxygen species as various signal molecules

Other than the positive effects, cells in our body are always exposed to oxidative damage which can occur if the ROS level increases. Cellular ROS level is regulated by antioxidant enzyme families (e.g. SOD or GPX in Figure 4.7) and various small molecules such as vitamins, thioredoxin [120] and glutathione [121] to minimize the oxidative damage. However, the conversion rate of ROS to non-toxic molecule by antioxidants is not perfect; possible detrimental effect by excessive ROS could always exist. As simply illustrated in Figure 4.6, DNA structure could be changed due to hydroxyl group [122][123][124]. Proteins would not function or be degraded if the structure is changed by the oxidation [125][126]. Oxidation of lipids could change their properties [127]. Ultra-violet radiation from the sun induces reactive oxygen species in our skin, mediating skin aging and increasing melanoma [128].
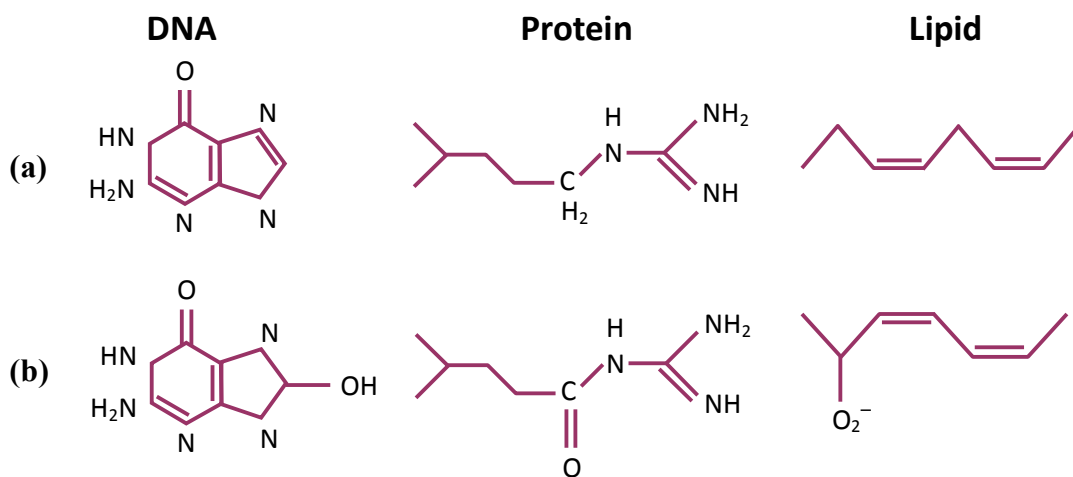
Figure 4.6 Detrimental effects of ROS to DNA, protein, and lipid.

(a) Natural structures. **(b)** Modified structures by ROS.

4.2.2 SOD Enzyme

Superoxide dismutase (SOD) enzyme family catalyzes dismutation of superoxide anion (O_2^-) into hydrogen peroxide, which proceeds to be reduced to water by catalase or GPX enzyme family (Figure 4.7) [129]. As such, SOD enzyme is primarily responsible for mediating oxidative damage to the cell. Three isoforms of SOD have been discovered in mammals. Superoxide dismutase-1 (SOD1) mostly exists in cytosol. Since SOD1 uses copper (Cu) and zinc (Zn) as cofactors, it is also known as CuZnSOD. SOD1 deficiency is known to be related to ALS [130] and liver cancer [131]. More than one hundred different SOD1 mutations have been found [132]; it has been suggested that over-expression of SOD1 could result in Down's Syndrome [133]. SOD2, also known as MnSOD, is localized in mitochondria and uses Manganese (Mn) as a cofactor. Abnormal SOD2 expression is also related to various diseases such as Alzheimer's disease [134] and tumor metastasis [135]. SOD3 is tetrameric

extracellular enzyme implicated in cardiovascular disorders and ischemia [136].
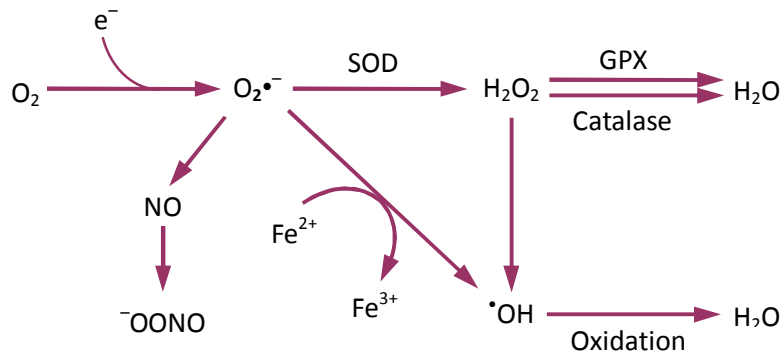
Figure 4.7 Major pathway of superoxide dismutased by SOD and GPX.

4.2.3 Myoblast Cell

Myoblasts are proliferating muscle progenitor cells, derived from muscle satellite stem cells found in skeletal muscle. They differentiate and self-assemble into muscle myotubes under the proper conditions [89]. Skeletal muscle is mainly composed of muscle fibers, and each muscle fiber is covered with a plasma membrane called a sarcolemma. Skeletal muscle also contains satellite cells located in between the basal lamina of skeletal muscle and the sarcolemma of muscle fiber [137]. Figure 4.8 describes the process of muscle regeneration inside skeletal muscles. Satellite cells are mostly quiescent; when they get signals, they proliferate or differentiate into myofibers. Once skeletal muscle undergoes injury, satellite cells are migrated into damaged area, re-enter the cell cycle and start proliferation as muscle precursor cells. After increasing population via a transient dividing stage, the myoblasts fuse together to become myofibers *in vivo* (or myotube *in vitro*), depending on differentiation signals.
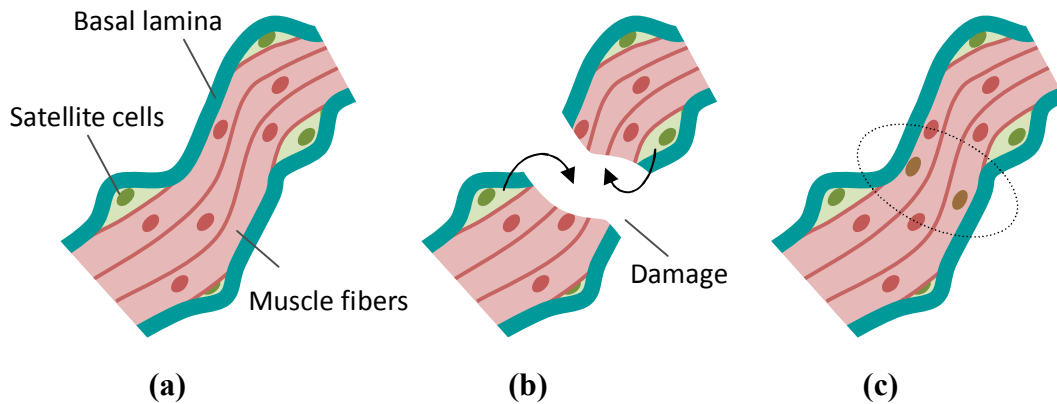
Figure 4.8 Muscle regeneration by satellite cells.

(a) Satellite cells stay quiescent in skeletal muscle. **(b)** Satellite cells are migrated into injured area and become myoblasts, then proliferate. **(c)** Myoblasts are differentiated into myofibers, healing damaged skeletal muscle.

At *in vitro* culture, this process can be recapitulated by isolating myoblasts from whole muscle, expanding myoblasts in high serum medium that encourages a cell to commence cell division (Figure 4.9). Cells are maintained as myoblasts in growth media, and then serum is drawn out of culture medium to induce differentiation. For this work, young wild-type myoblasts were isolated from three week old mice.
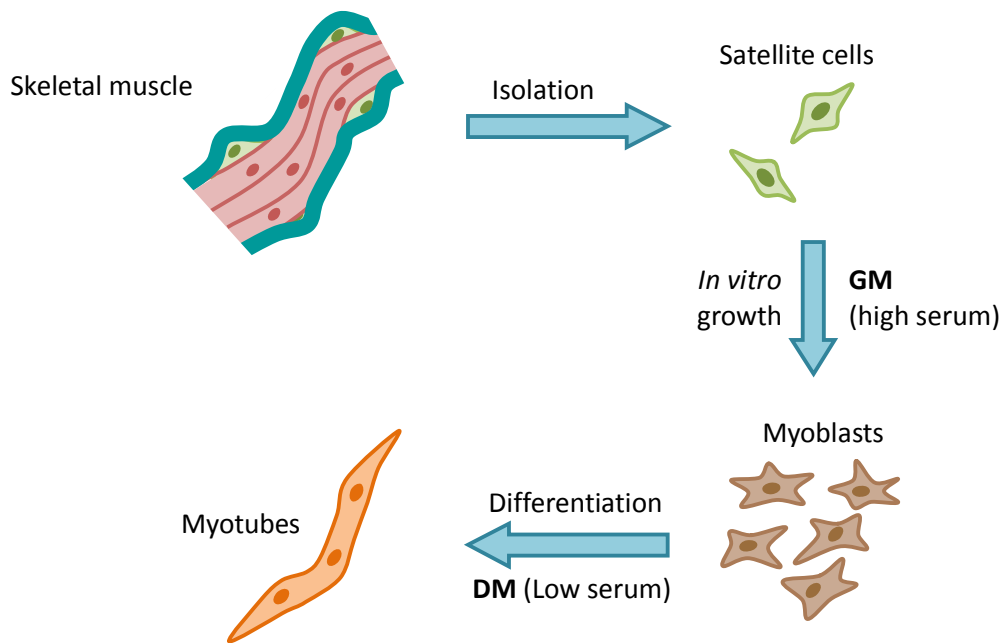
Figure 4.9 Process illustration of isolation and growth of myoblast *in vitro*.

4.2.4 SOD1 Heterozygous Myoblasts

SOD1 homozygous knockout (SOD1$^{-/-}$) mice developed normally but showed morphological abnormalities and degenerative changes after injury as well as decreased life span [138]. SOD1$^{-/-}$ mice also exhibit $17 - 20\%$ lower mass and accelerated sarcopenia when compared to wild-type mice [139], and impaired responses to oxidative stress [140]. SOD1$^{-/-}$ myoblasts have not been successfully maintained in culture [141]. For this reason, SOD1 heterozygous (SOD1$^{+/-}$) myoblasts were chosen for this work.

The heterozygote SOD1 mouse was generated via transgenesis [3]. Briefly, SOD1 homozygous knockout early embryonic stem cells were injected into blastocyst. If the modified DNA introduced into embryonic stem cells integrates, some of the sperms will carry the foreign DNA. When these transgenic sperm fertilize a normal egg, a transgenic mouse is

produced with the same foreign DNA in every cell. After this transgenesis, mice were screened. Heterozygous mice for SOD1 were chosen for this work.

4.2.5 *In Vitro* Growth

Due to less adhesion onto dish compared to C2C12 myoblasts, wild-type and SOD1 heterozygote myoblasts were cultured on a collagen-coated dish [142], with GM composed of 74% F-10 Ham's nutrient mixture (11550, Invitrogen), 1% penicillin/streptomycin (30-004-Cl, Cellgro), 25% FBS (26140, Gibco) and 5 ng/mL bFGF (G5071, Promega) in 37 °C incubator [141]. The bFGF stimulates proliferation and inhibits differentiation of myoblast to myotube [143]. 500× aliquot stock of bFGF is prepared by mixing and filter-sterilizing 10 mL of 1% BSA (0.12 g BSA in 10 mL PBS (10010-049, Invitrogen)) with 25 μg of bFGF powder, and is stored in −20 °C freezer. Passage or re-suspension was performed by trypsinizing for 1 minute with 1 mL of 0.25% trypsin-EDTA followed by PBS wash, then re-suspended onto a collagen-coated culture dish with 12 mL of GM and 24 μL of bFGF stock.

• Collagen Coating on Culture Dish

500 mL of 0.1 mg/mL collagen stock is prepared by adding 16.67 mL of collagen (PureCol, 5409, Inamed Biomaterials) into 483.3 mL of 0.1 N acetic acid made by mixing and filter-sterilizing 2.87 mL glacial acetic acid (acetic acid : 17.4 N) and 480.46 mL of QH$_2$O. 2 mL of the stock is applied into each 100 mm culture dish and swirl to spread evenly. After incubating the dishes overnight in 37 °C incubator, the liquids are aspirated and dishes are allowed to dry inside sterilized culture bench. Prepared dishes are stored in 4 °C refrigerator and washed quickly with PBS before suspending cell and culture medium.

4.3 Oxygen Concentration Gradients on SOD1 Heterozygote Myoblasts

Our proposed hypothesis was that SOD1 haplo-deficiency in myoblasts contributes to defective muscle differentiation compared to wild-type. To study this, the effect of oxygen stress to muscle progenitor cells and muscle differentiation will be characterized by exposing wild-type and $SOD^{+/-}$ myoblasts to various oxygen levels, while measuring cytosolic superoxide levels and characterizing and scoring morphologic differentiation.

Additionally, we hypothesized that cytosolic exchange through gap junctions could help cells be more robust to apoptotic levels of hypoxia or be induced to differentiate differently under different gradient conditions. We were curious as to whether cell-cell signaling would occur between different cells in a gradient, modulating the response of the cells in that gradient. For these experiments, cells were seeded to ensure cell-cell contact. Control experiments were done by the author in the Csete lab in Emory University as a collaboration.

Background removal was performed for fluorescent images in section 4.3.2 with Image J software ver. 1.42q (http://rsb.info.nih.gov/ij/) and multiple images were stitched with Adobe Photoshop CS3 for gradient experiments. Biological data acquired from duplicate experiments were expressed as mean value ± standard deviation using Microsoft Excel 2007. Student's t-test ($p = 0.05$ as significance level) was performed as a statistical analysis of comparison between two groups. In the experiment using OMA in section 4.3.1, about 40 images were taken then stitched for the entire area of OMA using Adobe Photoshop CS3 (see Figure 4.11 (b), (c)). The stitched image was divided at every 100 pixels from electrode in circular way, and light intensity of each cell was then measured and averaged in Matlab^{TM}.

4.3.1 Cytosolic Superoxide

Since SOD1 heterozygotes are half-deficient in the enzyme to convert superoxide to H_2O_2, the superoxide level inside $SOD1^{+/-}$ should be higher than that inside wild-type myoblasts. Cytosolic superoxide was measured using DHET, superoxide-sensitive fluorescent dye.

• DHET : Plate Control

DHET is fluorescent indicator assay for cytosolic superoxide detection in wild-type and $SOD1^{+/-}$ myoblasts. For dish controls, conventional protocol in biology was used [144][145] with optimization of concentration and incubation time. Cells were seeded with density of 35×10^3 cells/cm^2 on 60 mm culture dish, and grown with GM in 37 °C incubator for 3 days. After washing with PBS three times, 10 μM DHET solution mixed with 1% FBS in DMEM-F12 medium (DMEM : Nutrient mix F-12 without phenol-red and HEPES, 21041-025, Invitrogen) was loaded and incubated for 20 minutes. Cells were washed with PBS three times and re-suspended with 200 μL of 1% FBS in DMEM-F12 medium. Then the cells were transferred into black, flat-bottom 96 well plate (07201205, Fisher Scientific). A microplate reader (Synergy-HT, Biotek) was used to measure fluorescence (EX : 485 nm / EM : 530 nm) and the result was normalized to counted cell number.

• DHET : OMA

Unlike the plate control, fluorescence with OMA involves several issues on the measurement protocol. First, cells in OMA must stay adherent on PDMS membrane to experience oxygen microgradient, whereas the cells in control are re-suspended; thus the re-

suspending process is not allowed. Second, microscopy is used to detect fluorescence over the microgradient area, instead of the microplate reader. However, fluorescence detection with microscope was difficult even with long exposure when the same recipe was used since sensitivity of plate reader is much higher. Increasing concentration of the assay also caused a problem; usage of higher concentration of DHET affected viability of cells, leading then to shrink and death eventually. Without increasing DHET concentration, concentration of FBS in DMEM-F12 could be increased for cells to stay healthy. Increasing the serum concentration is also known to reduce fluorescence intensity [146]. Therefore, concentration of FBS was optimized with experiments. Lastly, the gas-control box encompassing OMA should keep anoxic condition while the washing steps and DHET loading to minimize a chance for cells to be exposed to ambient oxygen.
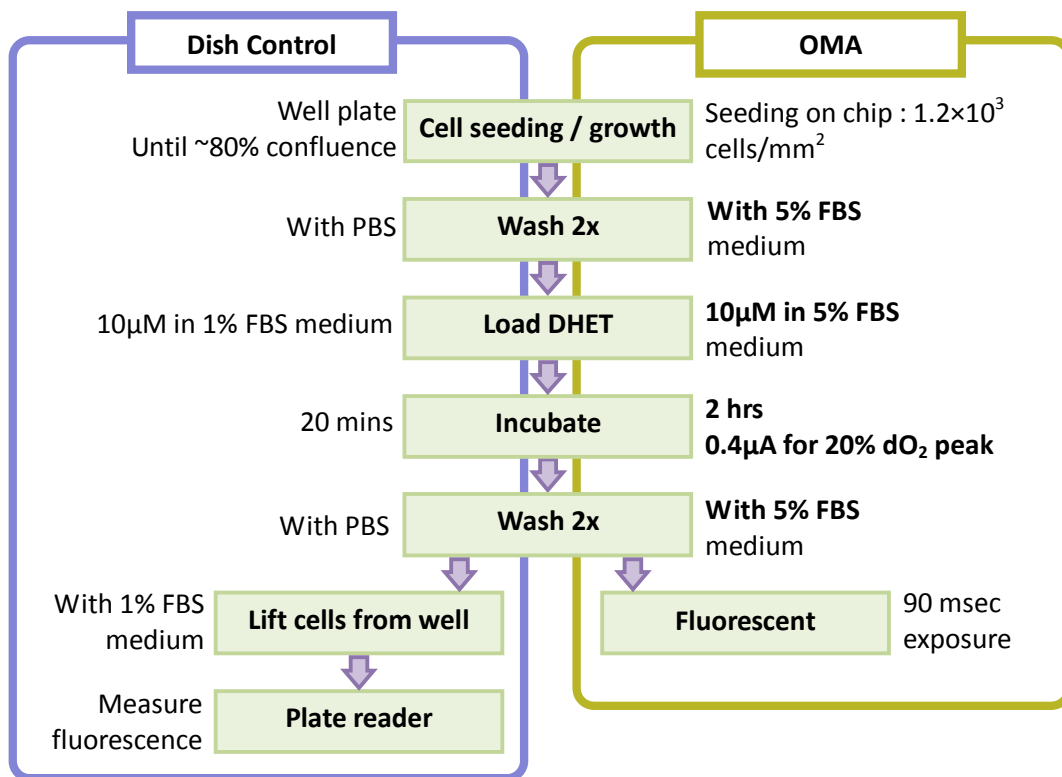
Figure 4.10 DHET measurement protocol for both dish control and OMA.

Culture area in OMA was treated with fibronectin for adhesion of cells. Cells were seeded with density of 1.2×10^3 cells/ mm^2; higher cell density than that in the control was used and cells were grown for 2 hours. The gas-control box was moved into a glove box (Model 5503-11, electro-tech systems) which maintains anoxic condition. After washing 2 times with 5% FBS in DMEM-F12, 10 μM of DHET in DMEM-F12 was loaded then the gas-control box was closed inside the glove box. After moving into 37 °C cell culture incubator, 5% CO_2 and 95% N_2 mixed gas was continuously purged, with 0.4 μA of current to generate 20% oxygen peak from electrode. After 2 hours of operation, box was transferred back into the anoxic glove box and cells were washed two times with 5% FBS in DMEM-F12. Images were taken with inverted microscope (B-2A filter cube). Figure 4.10 shows comparison of the DHET protocols in two different conditions.

In control (Figure 4.11 (a)), SOD1$^{+/-}$ myoblasts exhibited about 18% higher superoxide ($p = 0.009$) than wild-type myoblasts when exposed to ambient oxygen level (20% O_2). Superoxide detection in various oxygen level can be done with oxygen microgradient chip. Figure 4.11 (b) and (c) show the difference in cytosolic superoxide levels between wild-type and SOD1$^{+/-}$ myoblasts.

Figure 4.11 (d) shows quantitative fluorescence vs. distance from the oxygen source in the OMA. Note that intensity was plotted based on relative fluorescent unit (RFU). Because we know the concentration level of the oxygen microgradient, the light intensity can be rearranged to the oxygen level (Figure 4.11 (e)). From this, level of superoxide inside SOD1$^{+/-}$ myoblast is significantly higher than that inside wild-type myoblast through wide range of oxygen level ($p < 0.05$ except two data points at 14.3% and 11.1% O_2) as expected above.

(a)

(b)

SOD1$^{+/-}$

Electrode

1 mm

(c)

Wild-type

Electrode

1 mm
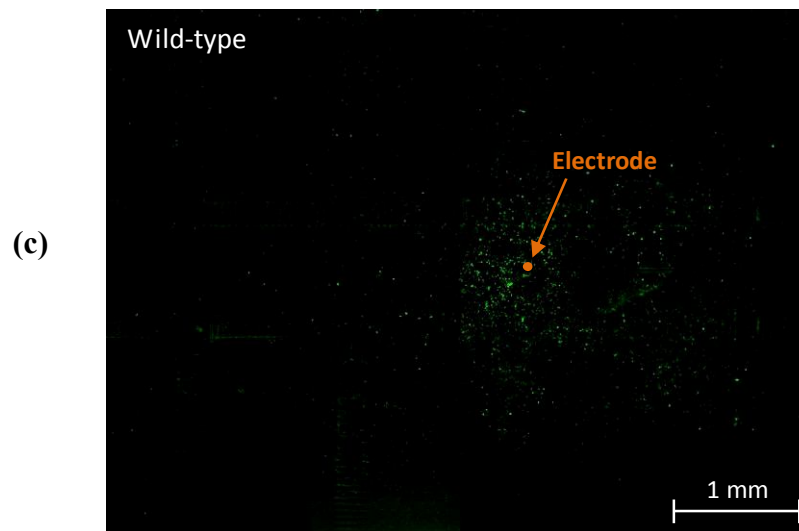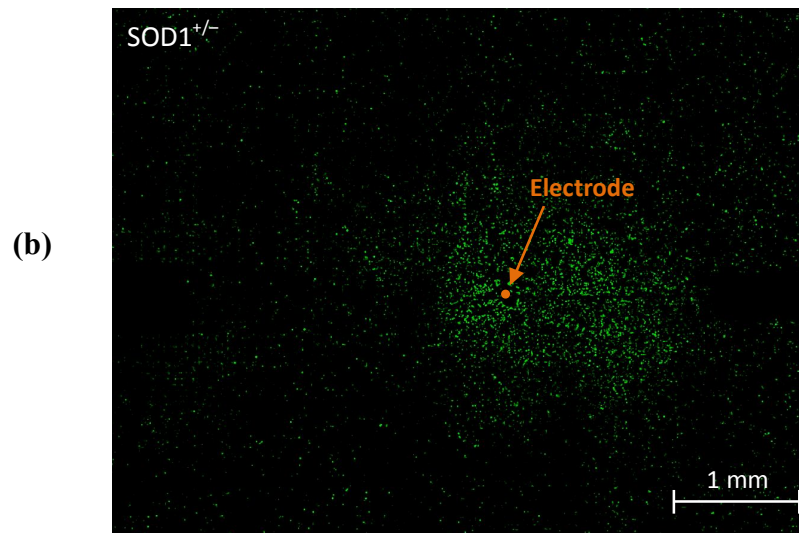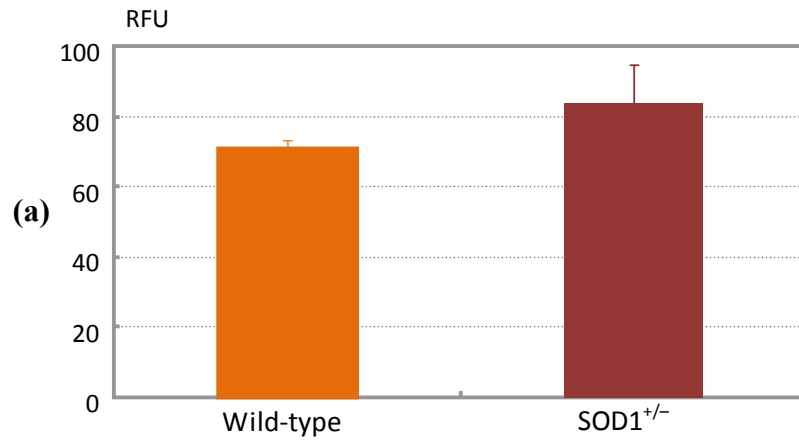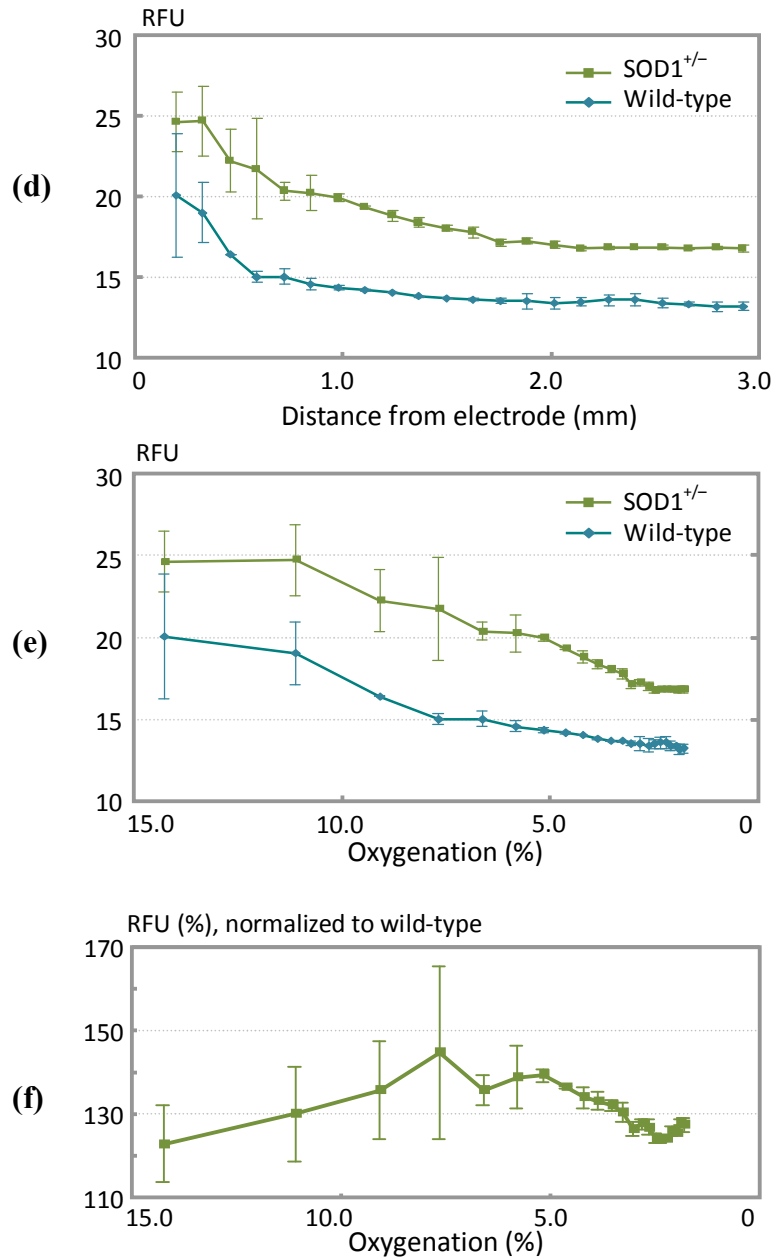
Figure 4.11 Superoxide anions in SOD1$^{+/-}$ compared to wild-type myoblasts.

(a) Control data with 20% O_2. **(b), (c)** DHET images on OMA, with SOD1$^{+/-}$ and wild-type, respectively. Fluorescence were amplified for visibility. **(d)** Intensity plot along distance from electrode. **(e)** Intensity plot with oxygen level. **(f)** Normalized intensity of SOD1$^{+/-}$ to that of wild-type myoblasts.

Figure 4.11 (f) shows normalized fluorescence of superoxide anion in SOD1$^{+/-}$ to that in wild-type. About 30% higher fluorescence was detected in SOD1$^{+/-}$ compared to wild-type, whereas 18% higher than the control.

4.3.2 Morphologic Differentiation

Normal differentiation of myoblasts in culture involves fusion of single-cell myoblasts into multinucleated myotubes, and coordinates up-regulation of MHC which can be stained with MF20 antibody. These morphologic observations were quantified by calculating the fusion index (FI) and differentiation potential (DP). FI is a percentage ratio between the number of nuclei in the myotubes having more than one nuclei versus the sum of nuclei in the myotubes and myoblasts. DP is a complementary method of quantifying efficiency of differentiation. Single cells expressing MHC (capable of fusion) are added to the numerator of FI, compared to DP.

$$\text{FI} = \frac{\text{Number of nuclei in MHC-expressed myotubes having} \geq 2 \text{ nuclei}}{\text{Total number of nuclei}} \times 100 \qquad (4.1)$$

$$\text{DP} = \frac{\text{Number of nuclei in MHC-expressed myotubes}}{\text{Total number of nuclei}} \times 100 \qquad (4.2)$$

The control experiment with discrete oxygen level involves a complicated setup for producing specific oxygen level. For the dish control, cells were normally grown on 60 mm culture dish for one day then culture medium was switched to DM. An incubator chamber (Modular Incubator Chamber MIC-101, Billups-Rothenberg) and culture dishes were

95

transferred into a glove box (O_2 Control Glove Box, CoyLab) and then the glove box was purged with a specific oxygen level (0%, 2%, 5%, and 10% O_2) and 5% CO_2. When the gas composition reaches desired level, the air chamber (having the dishes inside) was closed inside the globe box (culture dishes in the tight-sealed air chamber now have the specific gas ratio) and was transferred into 37 °C incubator. Therefore, whenever a specific oxygen level is needed, the whole globe box is purged with the oxygen. In contrast, experiments with oxygen gradient can be done with the simple oxygen gradient chip (section 3.5) generating continuous and wide-range of oxygen level, showing the gradient chip can substitute for conventional biology experimental system such as a gas-controlled glove box as well.

After 3 days of incubation in DM, myoblast cells were washed with DPBS (Dulbecco's PBS with calcium and magnesium, 21-030-CV, Mediatech) two times. Cells were fixed with 1:1 methanol and acetone mixture for 5 minutes at room temperature, then allowed to dry in chemical hood for 10 minutes. After rehydration in PBS for 10 minutes (for dish control, ~1cm diameter circles were made with pap-pen prior to this step), 10 % donkey serum (017-000-121, Jackson Immuno Research) in PBS was applied for 30 minutes as a blocking step. After removing the block gently, MF20 primary antibody (mf20-c, Developmental Studies Hybridoma Bank, University of Iowa) (1:50 dilution in PBS) was applied and incubated for 3 hours. Cells were washed three times with PBS on a shaking table, then secondary antibody (Alex Flour 568 anti-mouse IgG, A-11004, Invitrogen) was applied (1 : 400 dilution of in PBS) for 45 minutes. The red-fluorescent antibody was washed three times with PBS on a shaking table, then drop 10% DAPI (VECTASHIELD Mounting Medium with DAPI, H-1200, Vector Labs) in PBS on the stained cell and cover-slip was applied. G-2A for stained MHC and UV-2A (DM : 400 LP / EX : 330 − 380 / BA : 420 LP) for DAPI were used for imaging.

Figure 4.12 shows differentiation of wild-type and SOD1$^{+/-}$ under continuous oxygen gradient using the simple oxygen concentration gradient chip. Red fluorescence shows MHC immuno-staining while nuclei are marked with blue-fluorescent DAPI. Four individual images were stitched together to show a gradient of cell differentiation with respect to the oxygen level.

SOD1$^{+/-}$ shows clear defects in morphologic differentiation through the oxygen gradient, ranging from 14% to 0%, compared to wild-type. From phenotype observation, any overall directional formation of myotubes either along the same or toward higher oxygen level was not found. Control experiments with five discrete oxygen level (Figure 4.13) show the same result, with a distinct difference between wild-type and SOD1$^{+/-}$.

Because of the non-linearity of the oxygen profile across culture area in the case of the continuous gradient as in Figure 4.12, higher oxygenation area is smaller than lower oxygenation area, which affects total cell count. Fluorescent images were divided into segments of 2% oxygenated level. For example, FI and DP of 13% oxygenated level was calculated from a cropped culture area exposed to 14% − 12% oxygenated level. Especially for 1% and 0% oxygenated levels, 2% − 0.5% and 0.5% − 0% oxygenated areas were used for calculation, respectively. Cells normally grown in 20% oxygen (outside gas-control box, on normal culture dish) were included as normoxic control.
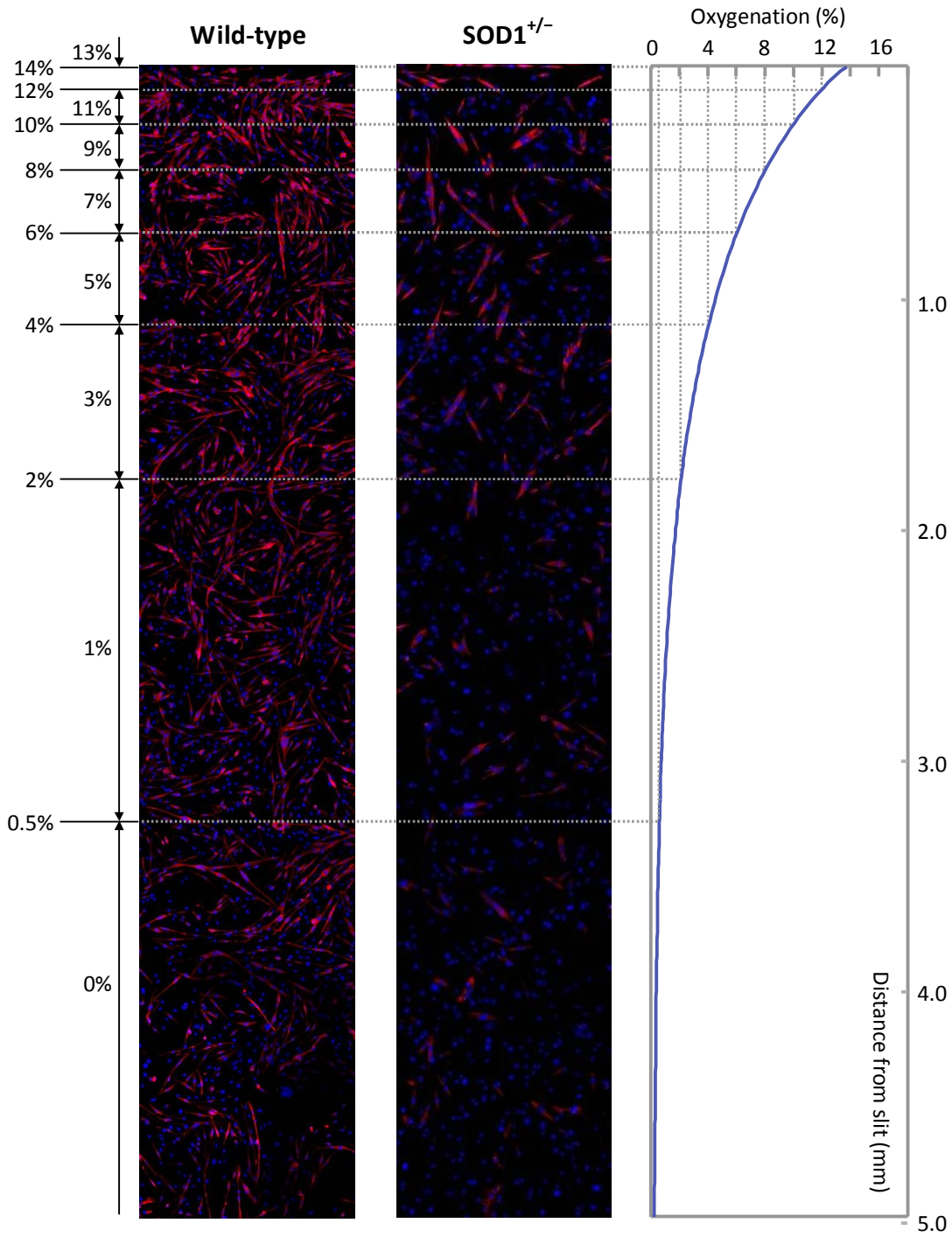
Figure 4.12 Differentiation of myoblasts in continuous oxygen gradient.

Cells on the area close to oxygen source experience higher oxygen compared to those on further area from the oxygen source.
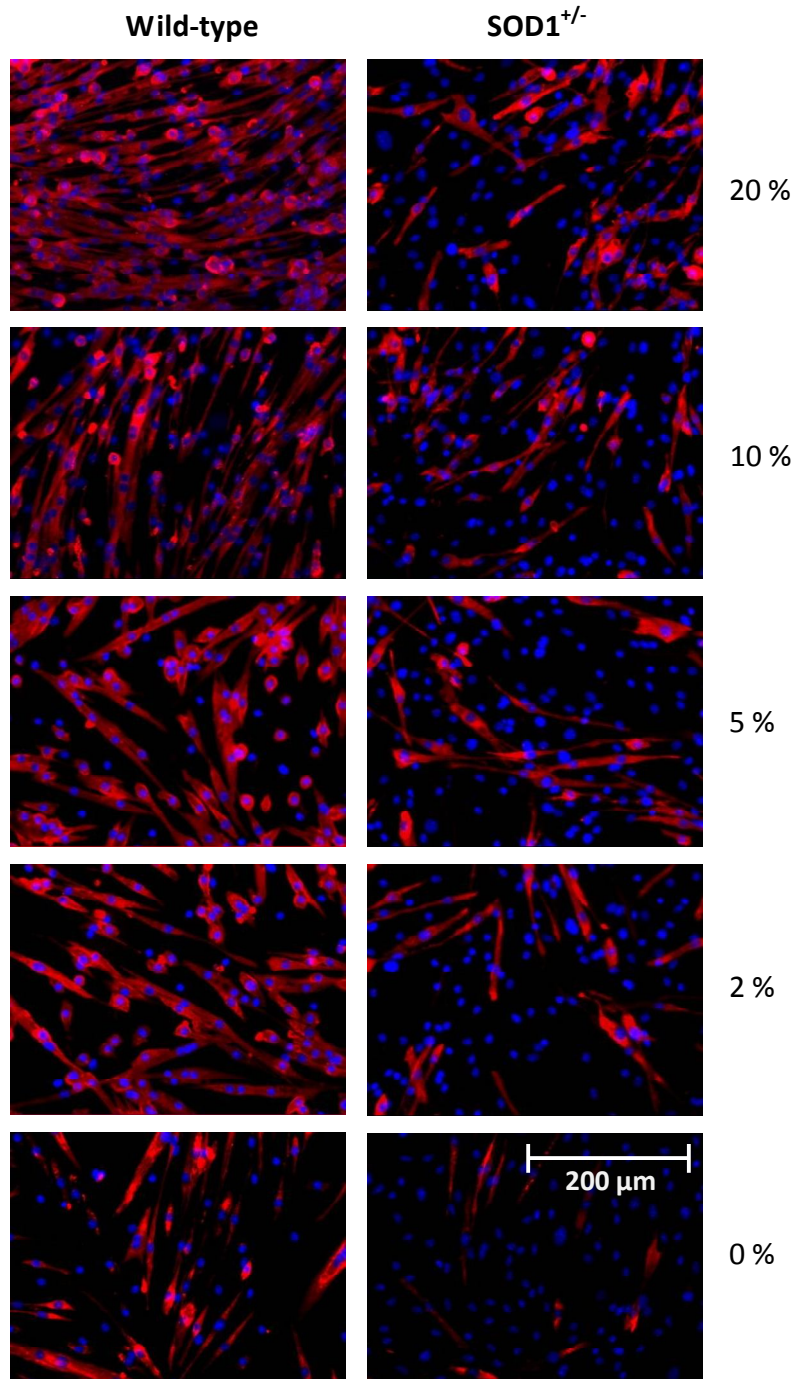
Figure 4.13 Differentiation of myoblasts in discrete oxygen levels using conventional

glove boxes (not oxygen microgradients).
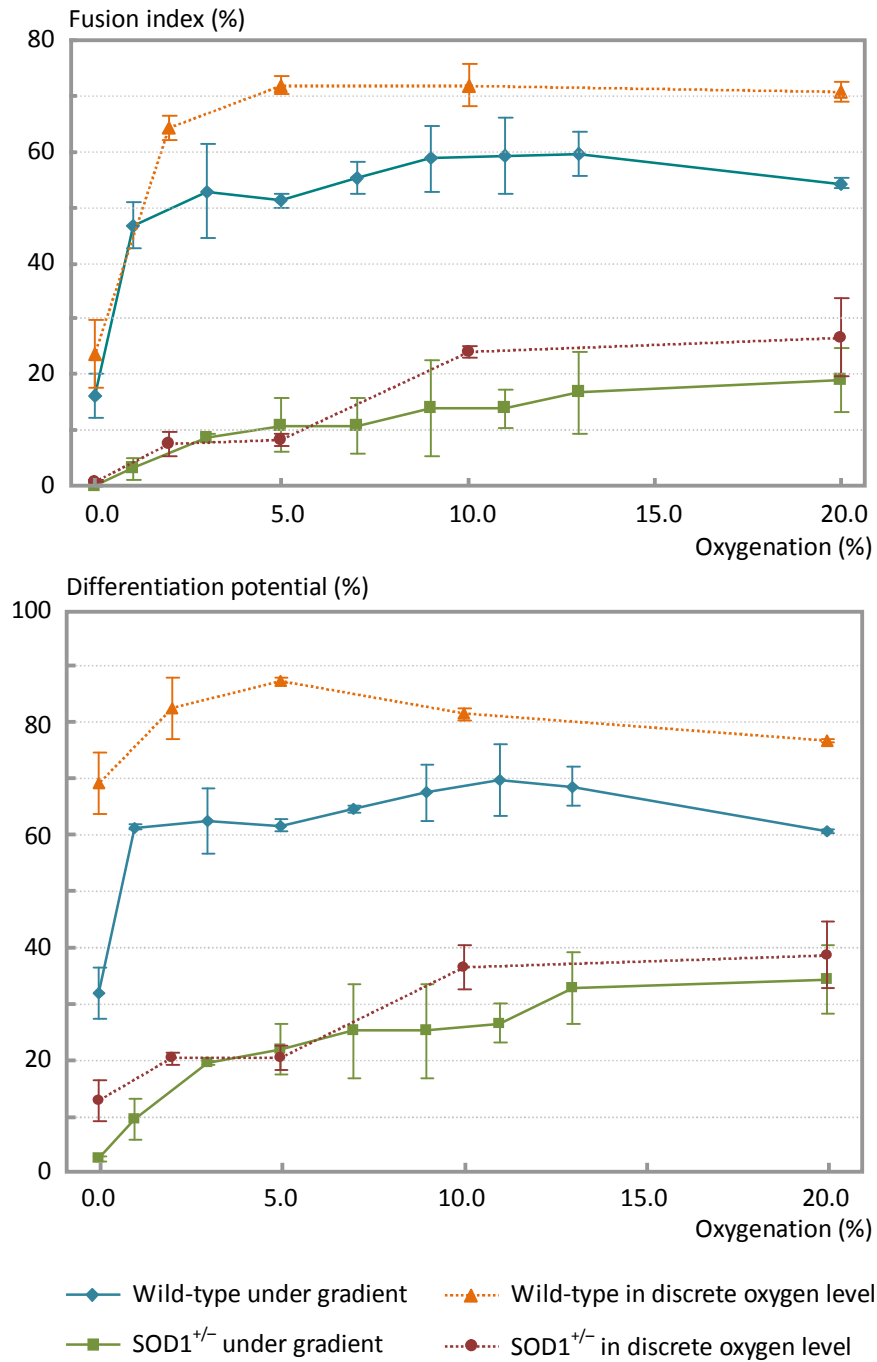
Figure 4.14 Quantification of differentiation for both cell types under discrete and gradient oxygen levels.

(a) Fusion index (FI) and **(b)** Differentiation potential (DP).

In Figure 4.14, both discrete and gradient oxidation experiments show similar trend at each cell type in response to the whole range of oxygen level. Despite of the similar trend, FI and DP from gradient experiment were lower than those from discrete experiment, including control in 20% O_2. The reason for this difference could be different passage numbers for the two types of experiment.
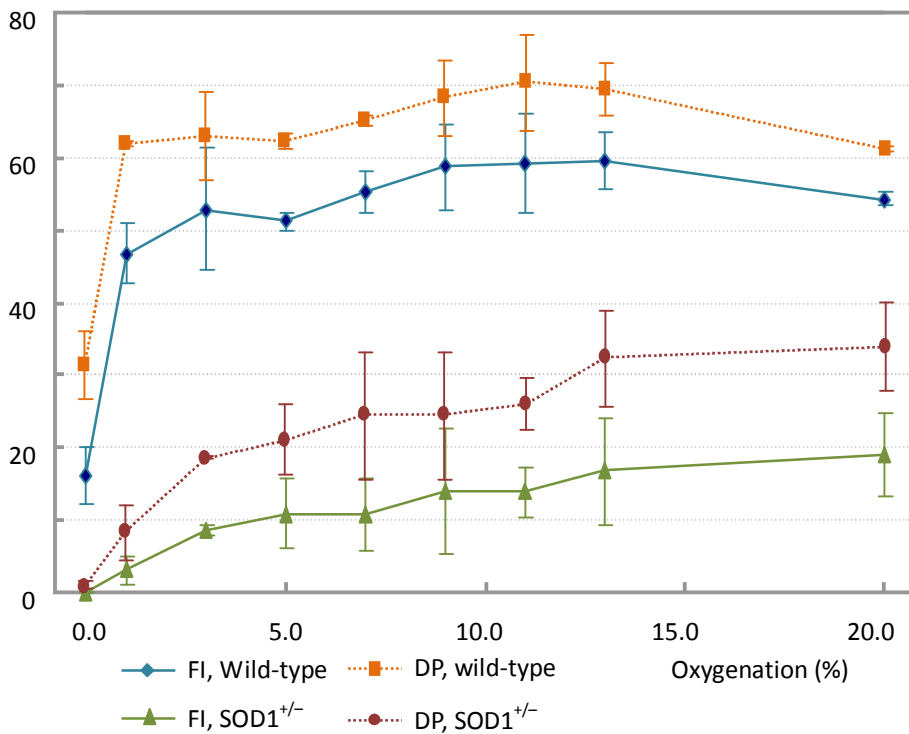
Figure 4.15 FI and DP of both cell types under continuous gradient oxidation.

Figure 4.15 shows FI and DP only from the result under oxygen gradient. FI of wild-type was almost flat with oxygen level (46.7 ± 4.1 in 1% O_2 and 54.3 ± 1.0 in 20% O_2) except in 0% oxygenated area (16.2 ± 3.9, p = 0.008 compared to 1% O_2). There was an increase of FI along 1% − 9% oxygen compared to oxygen level more than 11%, but differences between

each condition were not significant ($p > 0.05$); meaning the normal wild-type myoblast is robust to oxygen level. About 50% of wild-type myoblasts were differentiated in wide-range of oxygen. In contrast, FI of SOD1$^{+/-}$ myoblasts was much lower (~ 40% of difference) in most of oxygen range (~ exceptionally 16% of difference at 0% O_2), and significantly different behavior ($p < 0.05$ compared to wild-type in all oxygen levels); FI of SOD1$^{+/-}$ myoblasts gradually increased over oxygen level. FI in 0% O_2 was zero (no differentiation of cells), and maximum FI was in 20% O_2 (18.9 ± 5.8).

DP includes single cells expressing MHC, which is capable of fusion, on numerator of FI. In case of wild-type, the number of single cells expressing HMC was highest (~15%) in 0% and 2% O_2, but showed ~10% in other oxygen level with no significant difference. This means much more cells turned on MHC than fused cells incorporated into myotubes even in hypoxia condition, suggesting that MHC was prematurely turned on without fusion. Lowest DP of wild-type was 31.5 ± 4.7 in 0% O_2, and DP numbers in other oxygen were ~65, meaning that DP of wild-type myoblasts also indicates hypoxia-tolerant as well as FI. Single cells expressed HMC in SOD1$^{+/-}$ myoblasts showed gradual increase (1.2% in 0% O_2 − 15.6% in 13% O_2) in contrast to the wild-type case. DPs of SOD1$^{+/-}$ myoblasts were also lower than those of wild-type myoblasts over the entire oxygen range. Lowest DP was observed in 0% O_2 (1.2 ± 0.5) and increased gradually to the highest number (33.9 ± 6.2) in 20% O_2, indicating that SOD1$^{+/-}$ myoblasts are highly sensitive to oxygen level in terms of their differentiation.

Chapter 5

Conclusion and Future Directions

5.1 Summary of Contribution

Oxygen microenvironments formed by a concentration gradients in our body play a crucial role in many biological processes (e.g. vascular formation) and the progress of many diseases (e.g. non-vascularized tumor hypoxia). Because of this, there is a need for devices that can pattern and control the oxygen microenvironment in tissue culture. I believe the OMA technology can advance the current state-of-the-art in microgradient assays. The OMA technology should enable numerous studies in the field of biology where oxygen gradients are required.

5.1.1 Oxygen Microgradient Array

The OMA, a microsystem for the electrolytic patterning of oxygen concentration microgradients within 1 mm × 1 mm area during cell culture was developed. The system

employs an array of microfabricated Ti/Pt electrodes having $3-40$ µm in width. The array of electrodes was embedded under 5 µm height electrolyte channel to generate precise doses of dissolved oxygen via electrolysis of water. The dissolved oxygen diffuses up through a 10 µm thick, gas-permeable PDMS membrane and reach cell culture and medium. The oxygen concentration microgradient profile was able to be modulated by changing amount of current or altering the electrode during experiment, with saturation time less than one minute. A sharp microgradient from single electrode was superimposed to generate various, arbitrary microgradient profiles such as linear, triangular and cone-shaped. An oxygen-sensitive fluorophore membrane was introduced for quantification of oxygen microgradient generated from fabricated OMA.

Prior to fabrication, microgradients generated by various electrode configurations were simulated in COMSOL^{TM} software. Fabrication involved lithography to pattern electrodes and electrolyte channel, and molding process to assemble cell culture chamber on top. The early design was modified to enhance electrolyte loading. Various gas-control chambers were built to purge and maintain specific gas composition outside of the microsystem so that the oxygen source in the system is only by electrolytic generation. Beyond the OMA, we also built simple oxygen concentration microgradient chip which utilizes atmospheric oxygen to generate gradient without any electrical connection or microfabrication processes. ROS generation was discussed and hydrogen peroxide generated during the electrolysis was measured, showing that the peroxide will be low in the presence of cell and medium.

5.1.2 Biological Experiments

Three different types of culture experiments were demonstrated with the OMA in both

mammalian and prokaryotic systems. Localized hyperoxia (20% − 40% gradient dO_2) induced apoptosis in C2C12 myoblasts (with applying 20% additional O_2 peak onto 20% O_2 outside OMA), while control experiment (with the same 20% O_2 peak onto 0% O_2 outside) showed no apoptotic cells. Rapid re-oxygenation with oxygen microgradient following 45 minutes of hypoxia induced the localized calcium release in the study of ischemia/re-oxygenation myoblast model. Dynamic aerotaxis were demonstrated with assays of *Bacillus subtilis*; size of bacterial band was modulated by alteration of current density.

The reduced ability in SOD1-deficient myoblasts to convert superoxide into hydrogen peroxide showed ~30% increased amount of cytosolic superoxide compared to young, wild-type myoblasts throughout wide-range of oxygen (2% − 14% O_2 on microgradient, 20% O_2 as a control), and the difference may not be related to dosed oxygen. Less differentiation was definite in SOD1-deficient myoblasts in wide-range of oxygen level (0% − 13% O_2), indicating SOD1 haplo-deficiency in myoblasts contributed defective muscle differentiation compared to wild-type myoblasts by phenotype observation. Therefore, the detrimental effect of ROS on myoblasts can be concluded as significant; muscle differentiation and myoblast fusion were highly sensitive to increased cellular superoxide. Quantitive comparison of myoblast fusion between discrete (0%, 2%, 5%, 10%, 20% O_2) and continuous (under gradient) oxygen level showed no evidence of cell-cell signaling concerning hypoxia or differentiation in both cell types. Other than wild-type myoblasts which showed hypoxia-tolerant, SOD1-deficient myoblasts were highly sensitive to oxygen level in myoblast fusion and differentiation.

5.2 Future Directions

Despite the strong advantages of OMA listed above, there still needs improvements for special applications or enhancement as a biological application Solutions for some of the limitations experienced during development and future applications will be addressed in this section.

5.2.1 Feedback Control of Oxygen Microgradient

The calculation of microgradient profiles assumed that change in cellular oxygen was not high enough to change the microgradients. In cases where cellular oxygen consumption is high and stable, such as experiments with tumor cylindroids, the effect of the cellular consumption on the pre-defined oxygen microgradient can be estimated with high confidence. However, if 1) the consumption is high and changes with time or 2) the consumers move around the culture area (e.g. experiment with high density of aerobic bacteria), the resultant oxygen profile could not be determined easily. To compensate the dynamic consumption, a feedback control of oxygen profile would be required. The biggest problem for the control would be the real-time sensing of spatial oxygen distribution at the culture where cells experience oxygen. The oxygen-sensitive film used in OMA is not applicable for real-time sensing with cell culture, since the material requires frequent expose to fluorescent light. Therefore, new method of oxygen sensing needs for the feedback control, discussed in section 5.2.2.

5.2.2 Spatial Oxygen Sensing

Various types of oxygen-luminescent polymers have been developed in organic chemistry [147]. Among these, silicone-composite, oxygen-sensitive films would be useful if it can substitute both gas-transport membrane and oxygen sensing [87][148]. Ruthenium-based

complexes are widely used as oxygen sensor films [149][150], especially when dispersed in silicone rubber [151]. Bio-compatibility of the oxygen-sensor and the measuring system should be considered if the system is embedded in cell culture when building real-time feedback control (section 5.2.1). Long-term stability of the sensor at 37 °C would also be required given the long periods of cell culture.

5.2.3 Enhancement of PDMS Property

Despite the bio-compatibility of PDMS used in many bio-applications, problems still exist when using PDMS in cell culture. The toxicity of uncross-linked monomers mentioned in section 2.4.2 can be solved by washing PDMS in solvents in a specific sequence [152]. However, the washing process is not a perfect solution if the structure is complicated, since PDMS swells and causes huge deformation in early steps of the solvent process. After the washing step, nano-sized pores inside PDMS increase in diameter and transport of medium components may occur (see section 2.4.4). In case of the OMA, the washing step induced frequent chip-failures, making tiny pores on PDMS membrane and leaking culture medium into electrolyte channel.

A higher stiffness, gas permeable membrane would be preferred to replace the thin PDMS membrane in the OMA 1) to reduce density of post array inside electrolyte channel and 2) to provide harder substrate for cell adhesion. Lower number of posts can increase influx of oxygen plasma during surface treatment and enhance visibility for cell imaging. Slight modification of mixing ratio between monomer and cross-linker can change hardness of PDMS [153][154]. Baking temperature and time also affects hardness [74]; higher temperature would be preferred, but high-temperature baking process involves deformation of PDMS.

Lastly, scaffolding of stiffer membrane or the use of porous hydrophobic polymer may be advantageous.

5.2.4 Transparent Electrode

The Ti/Pt electrode used in OMA blocks microscopy. Altering the electrode area was minimized while designing oxygen microgradient to reduce the block. The constraint does make it difficult to design arbitrary gradient. Patterning Indium tin oxide (ITO) is widely used in panel displays due to its highly conductive and transparent characteristics [155][156]. ITO electrode could replace the Ti/Pt electrode, but more research needs to be done to investigate any optical degradation during water electrolysis [157] and the trade-off between conductivity and transparency.

5.2.5 Batch Operation of OMA

Many cases of biological experiment involve optimization over a large parameter space, which requires multiple experiments running different conditions at the same time. When running experiments in the same condition but with various cell types, a batch-operation would reduce researcher's effort and possible differences induced when duplicate experiments are done at different times. However, the OMA was not designed for multiple connections because of the limits in size of PCB (on which each chip is mounted) and the size of the gas-control chambers. It would thus be advantageous if multiple OMAs are connected to one current supply or an OMA chip having multiple cell culture areas on one substrate is designed.

5.2.6 Generation of Other Gases

There may be interest in generating gradient of other gases (e.g. NO) for biological application. Electrolytic generation of various gas molecule is possible with published electrolytes. Nitric oxide (NO), one of the most important gaseous molecules in biology and medicine [158], is an example. McGill *et al.* demonstrated electrolytic generation of NO using *N*-nitroso-*N*-oxybenzenamine ammonium salts as a compound in electrolyte [159]. However, accumulation of by-products and concentration change of the electrolyte composite should be considered during the operation.

5.2.7 System for Long-Term Sequential Imaging

It would be interesting to observe cell migration or progressive morphologic changes of cells in a gradient over a long-term period. This would require time-lapse microscopy. This would take from several hours to over a week depending on the experiment (e.g. tracking of myoblast migration during differentiation might require imaging every 20 minutes for several days). In the experiments with OMA, the gas-control chamber was placed inside a culture incubator for 37 °C temperature, while desired atmospheric condition around the OMA was maintained by a gas-purging system (section 3.6). The gas-control chamber needs to be placed on a microscope stage to run the sequential imaging during an experiment and temperature control of the chamber would have to be precisely controlled.

5.2.8 Wound-Healing Assay Using Oxygen Concentration Gradient

Observation of the wound-healing process under an oxygen concentration gradient would be of great interest. Once a tissue is mechanically damaged, cells tend to migrate toward the

damaged area and re-proliferate (e.g. muscle regeneration process in section 4.2.3); those morphological, dynamic activities *in vivo* can be reproduced in a wound healing assay *in vitro*. Wound-healing assays have been used for many years to monitor cell migration, proliferation [160], or any given factor inducing different behavior of cells during the recovering process [161][162]. In those assays, cells in a small area or line are removed by scraping off with a sharp object such as pipette tip, or by ECIS electrical wounding [163] for higher resolution. The damaged area is observed with microscopy over time as cells move in and recover the area (thus the equipment needed for long-term inspection would also be required as in section 5.2.7).

Oxygen has been known to play a significant role in wound-healing (see section 1.3). As an initial experiment, wild-type myoblasts were placed in a simple oxygen concentration gradient chip as in Figure 5.1; repopulation on higher oxygenated area is apparent. In relation to the experiment with SOD1 heterozygote myoblasts (section 4.2), oxygen concentration gradient might affect migration differently in SOD1$^{+/-}$ and wild-type cells. The direction of the wound can be made perpendicular or parallel to the oxygen concentration gradient (e.g. wound scratch along the same gradient direction could be used for observation of cell-cell signaling by changing the wounded gap). This assay could also be used for monitoring migration or morphologic change in response to chemotactic and chemokinetic factors which are known to be related to oxygen stress.

5% O$_2$ 2% O$_2$

500 μm
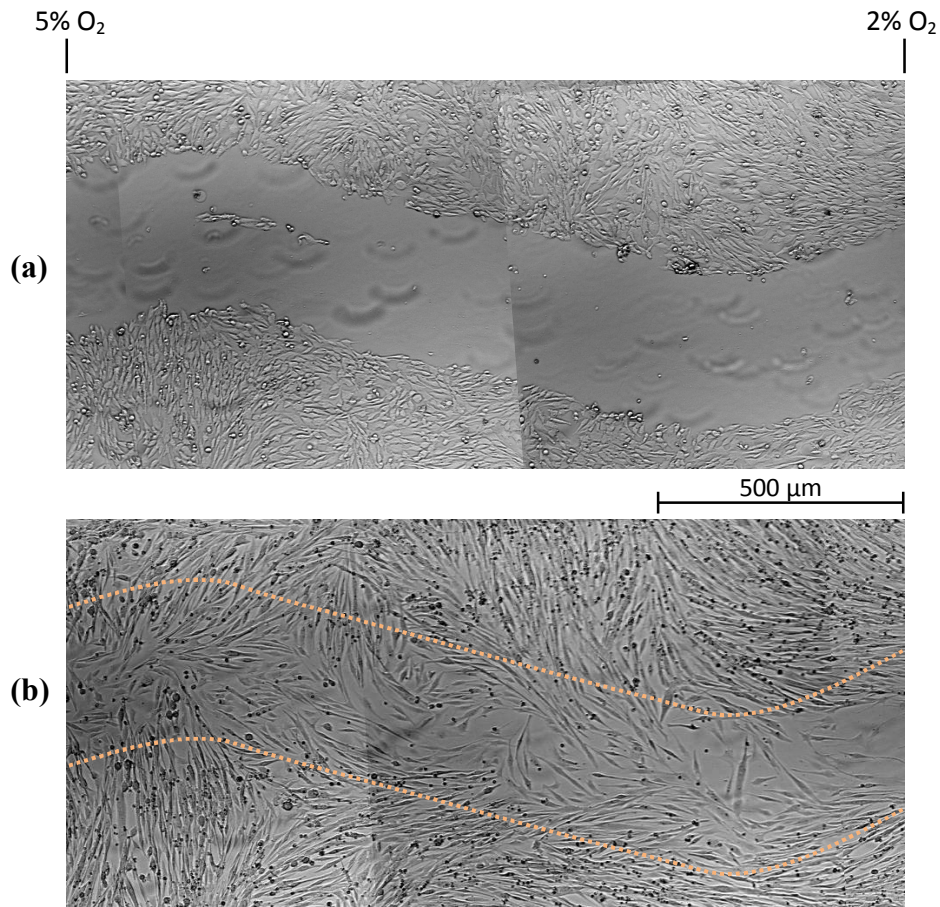
Figure 5.1 Migration and differentiation of wild-type myoblasts in wound-healing assay with oxygen gradient.

Once myoblast culture in GM reached 100% confluence, ~300 μm width wounded area was created by scraping with pipette tip in the gradient direction, followed by switching medium to DM. **(a)** After scraping, **(b)** after two days under oxygen gradient.

References

[1] H. A. Harper, V. W. Rodwell, and P. A. Mayes, *Review of Physiological Chemistry*, 16th edition, Lange Medical Publications, Los Altos, California, 1977.

[2] N. A. Campbell and J. B. Reece, *Biology*, 6th edition, Benjamin Cummings, 2002.

[3] H. Lodish, A. Berk , L. Zipursky, P Matsudaira , D. Baltimore, and J. Darnell, *Molecular Cell Biology*, 5th edition, W. H. Freeman, 2003.

[4] E. J. Fernandez and E. Lolis, "Structure, Function, and Inhibition of Chemokines," *Annu. Rev. Pharmacol. Toxicol.*, 42: 469−99, 2002.

[5] A. M. Turing, "The Chemical Basis of Morphogenesis," *Philos. Trans. R. Soc. London, Ser. B*, 237: 37−72, 1952.

[6] A. Yochelis, Y. Tintut, L. L. Demer, and A. Garfinkel, "The Formation of Labyrinths, Spots and Stripe Patterns in a Biochemical Approach to Cardiovascular Calcification," *New J. Phys.*, 10: 055002, 2008.

[7] A. Giaccia, B. G. Siim, and R. S. Johnson, "HIF-1 as a Target for Drug Development," *Nat. Rev. Drug Discovery*, 2: 803−11, 2003.

[8] G. L. Semenza, "Oxygen-regulated Transcription Factors and Their Role in Pulmonary Disease," *Respir. Res.*, 1: 159−62, 2000.

[9] G. L. Semenza, "HIF-1 and Human Disease: One Highly Involved Factor," *Genes Dev.*, 14: 1983−91, 2000.

[10] P. Carmeliet and R. K. Jain, "Angiogenesis in Cancer and Other Diseases," *Nature*, 407 (6801): 249−57, 2000.

[11] D. J. Ceradini, A. R. Kulkarni, M. J. Callaghan, O. M. Tepper, N. Bastidas, M. C.

Kleinman, J. M. Capla, R. D. Galiano, J. P. Levine, and G. C. Gurtner, "Progenitor Cell Trafficking is Regulated by Hypoxic Gradients through HIF-1 Induction of SDF-1," *Nature Med.*, 10 (8): 858−64, 2004.

[12] G. Payne, V. Bringi, C. Prince, and M. L. Shuler, *Plant Cell and Tissue Culture in Liquid Systems*, Wiley-Interscience, 1993.

[13] G. Helmlinger, F. Yuan, M. Dellian, and R. K. Jain, "Interstitial pH and pO_2 Gradients in Solid Tumors *in Vivo*: High-Resolution Measurements Reveal a Lack of Correlation," *Nature Med.*, 3 (2): 177−82, 1997.

[14] M. Höckel and P. Vaupel, "Tumor Hypoxia: Definitions and Current Clinical, Biologic, and Molecular Aspects," *J. Natl. Cancer Inst.*, 93 (4): 266-76, 2001.

[15] M. Höckel, K. Schlenger, S. Höckel, and P. Vaupel, "Hypoxic Cervical Cancers with Low Apoptotic Index Are Highly Aggressive," *Cancer Res.*, 59: 4525-28, 1999.

[16] E. K. Frow, J. Reckless, and D. J. Grainger, "Tools for Anti-Inflammatory Drug Design: In Vitro Models of Leukocyte Migration," *Med. Res. Rev.*, 24: 276-98, 2004.

[17] S. Boyden, "The Chemotactic Effect of Mixtures of Antibody and Antigen on Polymorphonuclear Leukocytes," *J. Exp. Med.*, 115: 453−66, 1962.

[18] N. L. Jeon, H. Baskaran, S. K. Dertinger, G. M. Whitesides, L. Van de Water, and M. Toner, "Neutrophil chemotaxis in linear and complex gradients of interleukin-8 formed in a microfabricated device," *Nat. Biotechnol.*, 20: 826−30, 2002.

[19] S. K. Dertinger, D. T. Chiu, N. L. Jeon, and G. M. Whitesides, "Generation of Gradients Having Complex Shapes Using Microfluidic Networks," *Anal. Chem.*, 73: 1240−46, 2001.

[20] D. M. Cochran, D. Fukumura, M. Ancukiewicz, P. Carmeliet, and R. K. Jain, "Evolution of Oxygen and Glucose Concentration Profiles in a Tissue-Mimetic Culture System of

Embryonic Stem Cells," *Ann. Biomed. Eng.*, 34 (8): 1247-1258, 2006.

[21] M. Pinelis, J. H. Park, and M. M. Maharbiz, "Bacterial Aerotaxis Assays with Spatial and Temporal Control of Oxygen Microscale Gradients," *BMES,* Baltimore, Maryland, 2005.

[22] O. Baracchini and J. C. Sherris, "The Chemotactic Effect of Oxygen on Bacteria," *J. Pathol. Bacteriol.*, 77: 565-74, 1959.

[23] S. I. Bibikov, R. Biran, K. E. Rudd, and J. S. Parkinson, "A Signal Transducer for Aerotaxis in *Escherichia Coli*," *J. Bacteriol.*, 179 (12): 4075–79, 1997.

[24] A. Rebbapragada, M. S. Johnson, G. P. Harding, A. J. Zuccarelli, H. M. Fletcher, I. B. Zhulin, and B. L. Taylor, "The Aer Protein and the Serine Chemoreceptor Tsr Independently Sense Intracellular Energy Levels and Transduce Oxygen, Redox, and Energy Signals for *Escherichia Coli* Behavior," *Proc. Natl. Acad. Sci. U S A.*, 94: 10541–46, 1997.

[25] D. J. Lazlo and B. L. Taylor, "Aerotaxis in Salmonella Typhimurium: Role of Electron Transport," *J. Bacteriol.*, 145: 990–1001, 1981.

[26] J. W. Allen and S. N. Bhatia, "Formation of Steady-State Oxygen Gradients *in Vitro*: Application to liver zonation," *Biotechnol. Bioeng.*, 82: 253-62, 2003.

[27] G. Mehta, K. Mehta, D. Sud, J. W. Song, T. Bersano-Begey, N. Futai, Y. S. Heo, M.-A. Mycek, J. J. Linderman, and S. Takayama, "Quantitative Measurement and Control of Oxygen Levels in Microfluidic Poly(dimethylsiloxane) Bioreactors during Cell Culture," *Biomed. Microdevices*, 123-134, 2007.

[28] P. Atkins, *Physical Chemistry*, 5th edition, Oxford University Press, Oxford, 1994.

[29] R. T. Ferrell, D. M. Himmelblau, "Diffusion coefficients of hydrogen and helium in water," *AIChE Journal*, 13 (4): 702 - 08, 2004.

[30] J. D. Seader and C. W. Tobias, "Ozone by Electrolysis of Sulfuric Acid*," Ind . Eng . Chem.,* 44 (9), 2207-11, 1952.

[31] E. R. Kotz and S. Stucki, "Ozone and Oxygen Evolution on PbO_2 electrodes in Acid Solution," *J. Electroanal. Chem.,* 228, 407-15, 1987.

[32] L. M. Da Silva, L. A. De Faria, and J. F. C. Boodts, "Green processes for environmental application. Electrochemical ozone production," *Pure Appl. Chem.,* 73 (12), 1871–84, 2001.

[33] P. C. Foller and C. W. Tobias, "The Anodic Evolution of Ozone," *J. Electrochem. Soc.*, 129 (3): 506-15, 1982.

[34] M. M. Maharbiz, W. J. Holtz, S. Sharifzadeh, J. D. Keasling, and R. T. Howe, "A Microfabricated Electrochemical Oxygen Generator for High-Density Cell Culture Arrays," *J. Microelectromech. Syst.*, 12 (5): 590-99, 2003.

[35] R. A. Jacob, "The integrated antioxidant system," *Nutr. Res.*, 15: 755-66, 1995.

[36] D. B. Min and J. M. Boff, "Singlet Oxygen Oxidation of Foods," *Comp. Rev. Food Sci. Food Safety*, 1: 58-6, 2002.

[37] Z. Qiang, J. H. Chang, and C. P. Huang, "Electrochemical Generation of Hydrogen Peroxide from Dissolved Oxygen in Acidic Solutions," *Water Res.*, 36 (1): 85-94, 2002.

[38] R. K. Hobbie, *Intermediate Physics for Medicine and Biology*, 3rd edition, John Wiley & Sons Inc, 1997.

[39] O. Pansarasa, L. Castagna, B. Colombi, J. Vecchiet, G. Felzani, and F. Marzatico, "Age and Sex Differences in Human Skeletal Muscle: Role of Reactive Oxygen Species," *Free Rad. Res.*, 33: 287-93, 2000.

[40] M. L. Hamilton, H. Van Remmen, J. A. Drake, H. Yang, Z. M. Guo, K. Kewitt, C. A. Walter, and A. Richardson, "Does Oxidative Damage to DNA Increase with Age?," *Proc.*

Natl. Acad. Sci., 98: 10469-74, 2001.

[41]   E. P. Kartalov, W. F. Anderson, and A. Scherer, "The Analytical Approach to Polydimethylsiloxane Microfluidic Technology and Its Biological Applications," *J. Nanosci. Nanotechnol.*, 6: 2265-77, 2006.

[42]   J. M. McDonald and G. M. Whitesides, "Poly(dimethylsiloxane) as a Material for Fabricating Microfluidic Devices," *Acc. Chem. Res.*, 35: 491–99, 2002.

[43]   J. C. McDonald, D. C. Duffy, J. R. Anderson, D. T. Chiu, H. Wu, O. J. A. Schueller, and G. M. Whitesides, "Fabrication of Microfluidic Systems in Poly (dimethylsiloxane)," *Electrophoresis*, 21 (1): 27–40, 1999.

[44]   D. K. Caia, A. Neyera, R. Kuckukb, and H. M. Heiseb, "Optical Absorption in Transparent PDMS Materials Applied for Multimode Waveguides Fabrication," *Opt. Mater.*, 30 (7): 1157-61, 2008.

[45]   G. Kotzara, M. Freas, P. Abelb, A. Fleischmanc, S. Royc, C. Zormand, J. M. Morane, and J. Melzak, "Evaluation of MEMS Materials of Construction for Implantable Medical Devices," *Biomaterials*, 23: 2737-50, 2002.

[46]   N. Angelova and D. Hunkeler, "Rationalizing the Design of Polymeric Biomaterials," *Trends Biotechnol.*, 17 (10): 409-21 1999.

[47]   J. N. Lee, X. Jiang, D. Ryan, and G. M. Whitesides, "Compatibility of Mammalian Cells on Surfaces of Poly(dimethylsiloxane)," *Langmuir*, 20: 11684-91, 2004.

[48]   J. N. Lee, C. Park, and G. M. Whitesides, "Solvent Compatibility of Poly(dimethylsiloxane)-Based Microfluidic Devices," *Anal. Chem.*, 75 (23): 6544–54, 2003.

[49]   A. Mata, C. Boehm, A. J. Fleischman, G. Muschler, and S. Roy, "Growth of Connective

Tissue Progenitor Cells on Microtextured Polydimethylsiloxane Surfaces," *J. Biomed. Mater. Res.*, 62 (4): 499-506, 2002.

[50]   M. T. Khorasani and H. Mirzadeh**, "**BHK Cells Behaviour on Laser Treated Polydimethylsiloxane Surface," *Colloids Surf., B*, 35 (1): 67-71, 2004.

[51]   Stephen J. Clarson, *Siloxane polymers,* Prentice Hall, Englewood Cliffs, N.J, 1993.

[52]   D. Armani, C. Liu, and N. Aluru, "Re-configurable Fluid Circuits by PDMS Elastomer Micromachining," *MEMS '99*, Orlando, Florida, 222-27, 1999.

[53]   J. C. Lötters, W. Olthuis, P. H. Veltink, and P. J. Bergveld, "The Mechanical Properties of the Rubber Elastic Polymer Polydimethylsiloxane for Sensor Applications," *Micromech. Microeng.*, 7: 145-147, 1997.

[54]   J. E. Mark, *Polymer Data Handbook*, 3rd edition. Oxford Univ. Press, New York, 1999.

[55]   H.-B. Wang, M. Dembo, and Y.-L. Wang, "Substrate Flexibility Regulates Growth and Apoptosis of Normal but not Transformed Cells," *Am. J. Physiol. Cell Physiol.*, 279 (5): C1345-50, 2000.

[56]   R. J. Pelham and Y. L. Wang, "Cell locomotion and focal adhesions are regulated by substrate flexibility," *Proc. Natl. Acad. Sci. USA.*, 94 (25): 13661–65, 1997.

[57]   T. Yeung, P. C. Georges, L. A. Flanagan, B. Marg, M. Ortiz, M. Funaki, N. Zahir, W. Ming, V. Weaver, and P. A. Janmey, "Effects of Substrate Stiffness on cell Morphology, Cytoskeletal Structure, and Adhesion," *Cell Motil. Cytoskeleton*, 60 (1): 24-34, 2005.

[58]   J. L. Tan, J. Tien, D. M. Pirone, D. S. Gray, K. Bhadriraju, and C. S. Chen, "Cells Lying on a Bed of Microneedles: An Approach to Isolate Mechanical Force," *PNAS*, 100 (4): 1484-89, 2003.

[59]   H. B. Wang, M. Dembo, and Y. L. Wang, "Substrate flexibility regulates growth and

apoptosis of normal but not transformed cells," *Am. J. Physiol. Cell Physiol.*, 279 (5): C1345–50, 2000.

[60] D. Bodasa and C. Khan-Malek, "Hydrophilization and Hydrophobic Recovery of PDMS by Oxygen Plasma and Chemical Treatment - An SEM Investigation," *Sens. Actuators B*, 123 (1): 368-373, 2007.

[61] G. G. Bausch, J. L. Stasser, J. S. Tonge, and M. J. Owen, "Behavior of Plasma-Treated Elastomeric Polydimethylsiloxane Coatings in Aqueous Environment," *Plasma Polym.*, 3 (1): 23-34, 1998.

[62] D. C. Duffy, J. C. McDonald, O. J. A. Schueller, and G. M. Whitesides, "Rapid Prototyping of Microfluidic Systems in Poly(dimethylsiloxane)," *Anal. Chem.*, 70 (23): 4974–84, 1998.

[63] Z. L. Zhanga, C. Crozatiera, M. Le Berrea, and Y. Chen, "In situ Bio-Functionalization and Cell Adhesion in Microfluidic Devices," *Microelectron. Eng.*, 78-79: 556-62, 2005.

[64] K. Miyaki, H.-L. Zeng, T. Nakagama, and K. Uchiyama, "Steady Surface Modification of Polydimethylsiloxane Microchannel and Its Application in Simultaneous Analysis of Homocysteine and Glutathione in Human Serum," *J. Chromatogr. A*, 1166 (1-2): 201-06, 2007.

[65] Y. Liu, J. C. Fanguy, J. M. Bledsoe, and C. S. Henry, "Dynamic Coating Using Polyelectrolyte Multilayers for Chemical Control of Electroosmotic Flow in Capillary Electrophoresis Microchips," *Anal. Chem.*, 72 (24): 5939–44, 2000.

[66] V. Linder, E. Verpoorte, W. Thormann, N. F. de Rooij, and H. Sigrist, "Surface Biopassivation of Replicated Poly(dimethylsiloxane) Microfluidic Channels and Application to Heterogeneous Immunoreaction with On-Chip Fluorescence Detection," *Anal. Chem.*, 73 (17): 4181–89, 2001.

[67] S. Bernhard, L. Thomas, K. Rudiger, W. Alexander, G. Vera-Maria, and N. Oskar, "UV-irradiation induced Modifcation of PDMS Flms Investigated by XPS and Spectroscopic Ellipsometry," *Surf. Sci.*, 532-535: 1067-71, 2003.

[68] T. J. Roseman, L. J. Larion, and S. S. Butler, "Transport of prostaglandins through silicone rubber," *J. Pharmaceutical Sci.*, 70 (5): 562- 66, 1981.

[69] T. Hatanaka, M. Inuma, K. Sugibayashi, and Y. Morimoto, "Prediction of Skin Permeability of Drugs. I. Comparison with Artificial Membrane," *Chem. Pharm. Bull.*, 38 (12): 3452–59, 1990.

[70] E. L. Warrick, O.R. Pierce, K. E. Polmanteer, and J. C. Saam, "Silicone Elastomers Development," *Rubber Chem. Technol.*, 52: 437, 1979.

[71] P. Pandey and R. S. Chauhan, "Membranes for Gas Separation," *Prog. Polym. Sci.*, 26: 853-93, 2001.

[72] W. L. Robb, "Thin Silicone Membranes - Their Permeation Properties and Some Applications," *Ann. N. Y. Acad. Sci.*, 146(1): 119-37, 1968.

[73] M. E. Cox and B. Dunn, "Oxygen Diffusion in Poly(dimethyl Siloxane) using Fluorescence Quenching. I. Measurement Technique and Analysis," *J. Polym. Sci., Part A: Polym. Chem.*, 24: 621-36, 1986.

[74] M. Liu, J. Sun, and Q. Chen, "Influences of Heating Temperature on Mechanical Properties of Polydimethylsiloxane," *Sens. Actuators A*, 151 (1): 42-45, 2009.

[75] J. L. Tan, J. Tien, D. M. Pirone, D. S. Gray, K. Bhadriraju, and C. S. Chen, "Cells Lying on a Bed of Microneedles: an Approach to Isolate Mechanical Force," *Proc. Natl. Acad. Sci.*, 100 (4): 1484-89, 2003.

[76] G. Y. Yang, V. J. Bailey, Y.-H. Wen, G. Lin, W. C. Tang, and J. H. Keyak, "Fabrication and

Characterization of Microscale Sensors for Bone Surface Strain Measurement.," *Proc., 3rd IEEE Int. Conf. Sensors*, 1355-58, 2004.

[77] J. O. Bockris, A. K. N. Reddy, and M. Gamboa-Aldeco, *Modern Electrochemistry*, 2nd edition, Springer, 2000.

[78] H. W. Blanch and D. S. Clark, *Biochemical Engineering*, CRC Press, 1997.

[79] P. G. Arthur, J. J. Giles, and C. M. Wakeford, "Protein Synthesis During Oxygen Conformance and Severe Hypoxia in the Mouse Muscle Cell Line C2C12," *Biochim. Biophys. Acta.*, 1475: 83-89, 2000.

[80] J. R. Welty, C. E. Wicks, and R. E. Wilson, *Fundamentals of Momentum, Heat, and Mass Transfer*, 3rd edition, John Wiley & Sons, NY, 1984.

[81] J. P. Hoare, "Some Effects of Alternating Current Polarization on the Surface of Noble Metal Electrodes", *Electrochemica Acta*, 9 (5): 599-605, 1964.

[82] N. Dias, R. A. Mortara, and N. Lima, "Morphological and Physiological Changes in Tetrahymena Pyriformis for the *in Vitro* Cytotoxicity Assessment of Triton X-100," *Toxicol. in Vitro*, 17 (3) 357-66, 2003.

[83] J. Monahan, A. A. Gewirth, and R. G. Nuzzo, "A Method for Filling Complex Polymeric Microfluidic Devices and Arrays," *Anal. Chem.*, 73 (13): 3193–97, 2001.

[84] W. Trettnak, W. Gruber, F. Reininger, and I. Klimant, "Recent Progress in Optical Oxygen Sensor Instrumentation," *Sens. Actuators B*, 29: 219-25, 1995.

[85] A. K. McEvoy, C. M. McDonagh, and B. D. MacCraith, "Dissolved Oxygen Sensor based on Fluorescence Quenching of Oxygen-sensitive Ruthenium Complexes Immobilised in Sol-gel-derived Porous Coatings," *Analyst*, 121: 785-88, 1996.

[86] A. Mills and F. C. Williams, "Chemical Influences on the Luminescence of Ruthenium

Diimine Complexes and Its Response to Oxygen," *Thin Solid Films*, 306: 163-70, 1997.

[87] X. Lu, I. Manners, and M. A. Winnik, "Polymer/Silica Composite Films as Luminescent Oxygen Sensors," *Macromolecules*, 34 (6): 1917-27, 2001.

[88] H. Nakagawa, K. Hasumi, J.-T. Woo, K. Nagai, and M. Wachi, "Generation of Hydrogen Peroxide Primarily Contributes to the Induction of Fe(II)-Dependent Apoptosis in Jurkat Cells by (−)-Epigallocatechin Gallate," *Carcinogenesis*, 25 (9): 1567-74, 2004.

[89] D. Yaffe and O. Saxel, "Serial passaging and differentiation of myogenic cells isolated from dystrophic mouse muscle," *Nature*, 270 (5639): 725-27, 1977.

[90] P. Mecocci, G. Fanó, S. Fulle, U. MacGarvey, L. Shinobu, M. C. Polidori, A. Cherubini, J. Vecchiet, U. Senin, and M. F. Beal, "Age-Dependent Increases in Oxidative Damage to DNA, Lipids, and Proteins in Human Skeletal Muscle," *Free Raical Biol. Med.*, 26: 303-08, 1999.

[91] A. Pagano and C. Barazzone-Argiroffo, "Alveolar Cell Death in Hyperoxia-Induced Lung Injury," *Ann. N. Y. Acad. Sci.*, 1010: 405-16, 2003.

[92] L. L. Mantell and P. J. Lee, "Signal Transduction Pathways in Hyperoxia-Induced Lung Cell Death," *Mol. Genet. Metab.*, 71: 359-70, 2000.

[93] J.J. Gille and H. Joenje, "Cell Culture Models for Oxidative Stress: Superoxide and Hydrogen Peroxide Versus Normobaric Hyperoxia," *Mutat. Res.*, 275 (3-6): 405–14, 1992.

[94] S. Kohin, C. M. Stary, R. A. Howlett, and M. C. Hogan, "Preconditioning Improves Function and Recovery of Single Muscle Fibers During Severe Hypoxia and Reoxygenation," *Am. J. Physiol. Cell Physiol.*, 281: C142-46, 2001.

[95] M. N. Sharikabad, K. M. Østbye, and O. Brørs, "Effect of Hydrogen Peroxide on Reoxygenation-Induced Ca^{2+} Accumulation in Rat Cardiomyocytes," *Free Radical Biol.*

Med., 37 (4): 531-38, 2004.

[96] L. S. Wong, M. S. Johnson, I. B. Zhulin, and B. L. Taylor, "Role of Methylation in Aerotaxis in *Bacillus Subtilis*," *J. Bacteriol.*, 177: 3985-91, 1995.

[97] A. Eschemann, M. Kühl, and H. Cypionka, "Aerotaxis in *Desulfovibrio*," *Environ. Microbiol.*, 1: 489-94, 1999.

[98] D. Emerson, R. M. Worden, and J. A. Breznak, "A Diffusion Gradient Chamber for Studying Microbial Behavior and Separating Microorganisms," *Appl. Environ. Microbiol.*, 60: 1269-78, 1994.

[99] U. Bandyopadhyay, D. Das, and R. K. Banerjee, "Reactive Oxygen Species: Oxidative Damage and Pathogenesis," *Current Science*, 77 (5): 658-66. 1999.

[100] D. Harman, "Aging: a Theory Based on Free Radical and Radiation Chemistry," *J. Gerontol.*, 11: 298–300, 1956.

[101] R. S. Balaban, S. Nemoto, and T. Finkel, "Mitochondria, Oxidants, and Aging," *Cell*, 120 (4): 483-95, 2005.

[102] B. J. Foth, "Phylogenetic Analysis to Uncover Organellar Origins of Nuclear-Encoded Genes," *Methods in Molecular Biology*, Clifton, N.J., 390: 467-88, 2007.

[103] A. Orient, A. Donko, A. Szabo, T. L. Leto, and M. Geiszt, "Novel Sources of Reactive Oxygen Species in the Human Body," *Nephrol. Dial. Transplant.*, 22 (5): 1281-88, 2007.

[104] M. K. Cathcart, "Regulation of Superoxide Anion Production by NADPH Oxidase in Monocytes/Macrophages: Contributions to Atherosclerosis," *Arterioscler Thromb. Vasc. Biol.*, 24 (1): 23-8, 2004.

[105] S. L. Linas, D. Whittenburg, and J. E. Repine, "Role of Xanthine Oxidase in Ischemia/Reperfusion Injury," *Am. J. Physiol. Renal Physiol.*, 258: F711-16, 1990.

[106] M. Geiszt and T. L. Leto, "The Nox Family of NAD(P)H Oxidases: Host Defense and Beyond," *J. Biol. Chem.*, 279: 51715–18, 2004.

[107] J. D. Lambeth, "NOX Enzymes and the Biology of Reactive Oxygen," *Nat. Rev. Immunol.*, 4: 181–89, 2004.

[108] G. Cheng, Z. Cao, X. Xu, E. G. van Meir, and J. D. Lambeth, "Homologs of gp91*phox*: Cloning and Tissue Expression of Nox3, Nox4, and Nox5," *Gene*, 269: 131-40, 2001.

[109] S. Miwa, K. B. Beckman, and F. L. Muller, *Oxidative Stress in Aging - From Model Systems to Human Diseases*, Humana Press, 2008.

[110] H. Sauer, M. Wartenberg, and J. Hescheler, "Reactive Oxygen Species as Intracellular Messengers During Cell Growth and Differentiation," *Cell. Physiol. Biochem.*, 11: 173-86, 2001.

[111] R. S. Arnold, J. Shi, E. Murad, A. M. Whalen, C. Q. Sun, R. Polavarapu, S. Parthasarathy, J. A. Petros, and J. D. Lambeth, "Hydrogen Peroxide Mediates the Cell Growth and Transformation Caused by the Mitogenic Oxidase Nox1," *PNAS*, 98 (10): 5550-55, 2001.

[112] B.-Y. Kim, M.-J. Han, and A.-S. Chung, "Effects of Reactive Oxygen Species on Proliferation of Chinese Hamster Lung Fibroblast (V79) Cells," *Free Radical Biol. Med.*, 30 (6): 686-98, 2001.

[113] H. Sauer, C. Ruhe, J. P. Muller, M. Schmelter, R. D'Souza, and M. Wartenberg, "Reactive Oxygen Species and Upregulation of NADPH Oxidases in Mechanotransduction of Embryonic Stem Cells," *Methods Mol. Biol.*, 477: 397-418, 2008.

[114] S. Cemerski, A. Cantagrel, J. P. M. van Meerwijk, and P. Romagnoli, "Reactive Oxygen Species Differentially Affect T Cell Receptor-Signaling Pathways," *J. Biol. Chem.*, 277: 19585-93, 2002.

[115] M. Geiszt, K. Lekstrom, S. Brenner, S. M. Hewitt, R. Dana, H. L. Malech, T. L. Leto, "NAD(P)H Oxidase 1, a Product of Differentiated Colon Epithelial Cells, can Partially Replace glycoprotein 91*phox* in the Regulated Production of Superoxide by Phagocytes," *J. Immunol.*, 171: 299-306, 2003.

[116] H.-U. Simon, A. Haj-Yehia, and F. Levi-Schaffer, "Role of Reactive Oxygen Species (ROS) in Apoptosis Induction," *Apoptosis*, 5: 415-18, 2000.

[117] R. Colavitti and T. Finkel, "Reactive Oxygen Species as Mediators of Cellular Senescence," *IUBMB Life*, 57 (4-5): 277–81, 2005.

[118] J. F. Passos and T. von Zglinicki, "Oxygen Free Radicals in Cell Senescence: Are They Signal Transducers?," *Free Radical Res.*, 40 (12): 1277-83, 2006.

[119] B. Matthew, "Reactive Oxygen Species in Immune Responses," *Free Radical Biol. Med.*, 36 (12): 1479-80, 2004.

[120] J. R. Gasdaska, M. Berggren, and G. Powis, "Cell Growth Stimulation by the Redox Protein Thioredoxin Occurs by a Novel Helper Mechanism", *Cell Growth Differentiation*, 6: 1643-50, 1995.

[121] M. Erden-Inal, E. Sunal, and G. Kanbak, "Age-Related Changes in the Glutathione Redox System," *Cell Biochem. Funct.*, 20: 61-66, 2002.

[122] J. H. Jackson, I. U. Schraufstatter, P. A. Hyslop, K. Vosbeck, R. Sauerheber, S. A. Weitzman, and C. G. Cochrane, "Role of Oxidants in DNA Damage. Hydroxyl Radical Mediates the Synergistic DNA Damaging Effects of Asbestos and Cigarette Smoke," *J. Clin. Invest.*, 80 (4): 1090–95, 1987.

[123] B. Balasubramanian, W. K. Pogozelski, and T. D. Tullius, "DNA Strand Breaking by the Hydroxyl Radical is Governed by the Accessible Surface Areas of the Hydrogen Atoms of

the DNA Backbone," *PNAS*, 95 (17): 9738-43, 1998.

[124] J. Cadet, T. Delatour, T. Douki, D. Gasparutto, J. P. Pouget, J. L. Ravanat, and S. Sauvaigo, "Hydroxyl Radicals and DNA Base Damage," *Mutat. Res.*, 424 (1-2): 9-21, 1999.

[125] R. L. Levine, "Carbonyl Modified Proteins in Cellular Regulation, Aging, and Disease," *Free Radical Biol. Med.*, 32: 790-96, 2002.

[126] R. Levine and E. Stadtman, "Oxidative Modification of Proteins during Aging," *Experimental Gerontology*, 36: 1495-502, 2001.

[127] J. F. Griveau, E. Dumont, P. Renard, J. P. Callegari, and D. Le Lannou, "Reactive Oxygen Species, Lipid Peroxidation and Enzymatic Defence Systems in Human Spermatozoa," *Journal of Reproduction and Fertility*, 103: 17-26, 1995.

[128] K. M. Hanson, E. Gratton , and C. J. Bardeen, "Sunscreen Enhancement of UV-Induced Reactive Oxygen Species in the Skin," *Free Radical Biol. Med.*, 41: 1205-12, 2006.

[129] H. M. Steinman, V. R. Naik, J. L. Abernethy, and R. L. Hill, "Bovine Erythrocyte Superoxide Dismutase. Complete Amino Acid Sequence," *J. Biol. Chem.*, 249 (22): 7326-38, 1974.

[130] A. C. Bowling, J. B. Schulz, and R. H. Brown Jr., M. F. Beal, "Superoxide Dismutase Activity, Oxidative Damage, and Mitochondrial Energy Metabolism in Familial and Sporadic Amyotrophic Lateral Sclerosis," *J. Neurochem.*, 61: 2322-25, 1993.

[131] R. A. Busuttil, A. M. Garcia, C. Cabrera, A. Rodriguez, Y. Suh, W. H. Kim, T.-T. Huang, and J. Vijg, "Organ-Specific Increase in Mutation Accumulation and Apoptosis Rate in CuZn-Superoxide Dismutase-Deficient Mice," *Cancer Res.*, 65: 11271-75, 2005.

[132] J. S. Beckman, A. G. Esetvez, L. Barbeito, and J. P. Crow, "CCS Knockout Mice Establish an Alternative Source of Copper for SOD in ALS," *Free Radical Biol. Med.*, 33: 1433-35,

2002.

[133] Y. Groner, O. Elroy-Stein, K. B. Avraham, M. Schickler, H. Knobler, D. Minc-Golomb, O. Bar-Peled, R. Yarom, and S. Rotshenker, "Cell Damage by Excess CuZnSOD and Down's Syndrome," *Biomed. Pharmacother.*, 48 (5-6): 231–40, 1994.

[134] H. W. Wiener, R. T. Perry, Z. Chen, L. E. Harrell, and R. C. Go, "A Polymorphism in SOD2 Is Associated with Development of Alzheimer's Disease, Genes, Brain, and Behavior," *Genes Brain Behav.*, 6 (8): 770-5, 2007.

[135] K. K. Nelson, A. C. Ranganathan, J. Mansouri, A. M. Rodriguez, K. M. Providence, J. L. Rutter, K. Pumiglia, J. A. Bennett, and J. A. Melendez, "Elevated Sod2 Activity Augments Matrix Metalloproteinase Expression: Evidence for the Involvement of Endogenous Hydrogen Peroxide in Regulating Metastasis," *Clin. Cancer Res.*, 9: 424-32, 2003.

[136] H. Sheng, T. C. Brady, R. D. Pearlstein, J. D. Crapo, and D. S. Warner, "Extracellular Superoxide Dismutase Deficiency Worsens Outcome from Focal Cerebral Ischemia in the Mouse," *Neurosci. Lett.*, 267: 13-16, 1999.

[137] A. Mauro, "Satellite Cell of Skeletal Muscle Fibers," *J. Biophys Biochem. Cytol.*, 9: 493-95, 1961.

[138] A. G. Reaume, J. L. Elliott, E. K. Hoffman, N. W. Kowall, R. J. Ferrante, D. F. Siwek, H. M. Wilcox, D. G. Flood, M. F. Beal, R. H. Brown Jr., R. W. Scott, and W. D. Snider, "Motor Neurons in Cu/Zn Superoxide Dismutase-Deficient Mice Develop Normally but Exhibit Enhanced Cell Death after Axonal Injury," *Nat. Genet.*, 13: 43-47, 1996.

[139] F. L. Muller, W. Song, Y. Liu, A. Chaudhuri, S. Pieke-Dahl, R. Strong, T. T. Huang, C. J. Epstein, L. J. Roberts, 2nd, M. Csete, J. A. Faulkner, and H. Van Remmen, "Absence of Cuzn Superoxide Dismutase Leads to Elevated Oxidative Stress and Acceleration of Age-

Dependent Skeletal Muscle Atrophy," *Free Radical Biol. Med.*, 40: 1993-2004, 2006.

[140] J. J. Marden, M. M. Harraz, A. J. Williams, K. Nelson, M. Luo, H. Paulson, and J. F. Engelhardt, "Redox Modifier Genes in Amyotrophic Lateral Sclerosis in Mice," *J. Clin. Invest.*, 117: 2913-19, 2007.

[141] S. Lee, H. S. Shin, P. K. Shireman, A. Vasilaki, H. Van Remmen, and M. E. Csete, "Glutathione-Peroxidase-1 Null Muscle Progenitor Cells are Globally Defective," *Free Radical Biol. Med.*, 41: 1174-84, 2006.

[142] S. Arnesen, S. Mosler, N. Larsen, N. Gadegaard, P. Purslow, and M. Lawson, "The Effects of Collagen Type I Topography on Myoblasts *In Vitro*," *Connect Tissue Res.*, 45 (4-5): 238-47, 2004.

[143] J. S. Campbell, M. P. Wenderoth, S. D. Hauschka, and E. G. Krebs, "Differential Activation of Mitogen-Activated Protein Kinase in Response to Basic Fibroblast Growth Factor in Skeletal Muscle Cells," *Proc. Natl. Acad. Sci. USA.*, 92: 870-74, 1995.

[144] L. Tong, S. Lee, and J. M. Denu, "Hydrolase Regulates NAD+ Metabolites and Modulates Cellular Redox," *J. Biol. Chem.*, 284: 11256-66, 2009.

[145] O. Moiseeva, V. Bourdeau, A. Roux, X. Deschênes-Simard, and G. Ferbeyre, "Mitochondrial Dysfunction Contributes to Oncogene-Induced Senescence," *Mol. Cell. Biol.*, 29 (16): 4495–07, 2009.

[146] D. J. R. Laurence, "A Study of the Adsorption of Dyes on Bovine Serum Albumin by the Method of Polarization of Fluorescence," *J. Biochem.*, 51(2): 168–80, 1952.

[147] Y. Kostov, Z. Gryczynski, and G. Rao, "Polarization Oxygen Sensor: a Template for a Class of Fluorescence-Based Sensors," *Anal. Chem.*, 74: 2167-71, 2002.

[148] J. M. Bedlek-Anslow, J. P. Hubner, B. F. Carroll, and K. S. Schanze, "Micro-heterogeneous

Oxygen Response in Luminescence Sensor Films," *Langmuir*, 16: 9137-41, 2000.

[149] M. M. F. Choi and D. Xiao, "Linear Calibration Function of Luminescence Quenching-Based Optical Sensor for Trace Oxygen Analysis," *Analyst*, 124: 695–98, 1999.

[150] N. Leventis, A.-M. M. Rawashdeh, I. A. Elder, J. Yang, A. Dass, and C. Sotiriou-Leventis, "Synthesis and Characterization of Ru(II) Tris(1,10-phenanthroline)-Electron Acceptor Dyads Incorporating the 4-Benzoyl-N-methylpyridinium Cation or *N*-Benzyl-*N'*-methyl Viologen. Improving the Dynamic Range, Sensitivity, and Response Time of Sol Gel-Based Optical Oxygen Sensors," *Chem. Mater.*, 16: 1493-506, 2004.

[151] Ingo Klimant and O. S. Wolfbeis, "Oxygen-Sensitive Luminescent Materials Based on Silicone-Soluble Ruthenium Diimine Complexes," *Anal. Chem.*, 67: 3160-66, 1995.

[152] L. J. Millet, M. E. Stewart, J. V. Sweedler, R. G. Nuzzo, and M. U. Gillette, "Microfluidic Devices for Culturing Primary Mammalian Neurons at Low Densities," *Lab Chip*, 7: 987-94, 2007.

[153] M. Liu and Q. Chen, "Characterization Study of Bonded and Unbonded Polydimethylsiloxane Aimed for Bio-Micro-Electromechanical Systems-Related Applications," *J. Micro/Nanolithogr. MEMS MOEMS*, 6: 023008, 2007.

[154] X. Q. Browna, K. Ookawa1, and J. Y. Wong, "Evaluation of Polydimethylsiloxane Scaffolds with Physiologically-Relevant Elastic Moduli: Interplay of Substrate Mechanics and Surface Chemistry Effects on Vascular Smooth Muscle Cell Response," *Biomaterials*, 26 (16): 3123-29, 2005.

[155] C. G. Granqvist, "Transparent Conductive Electrodes for Electrochromic Devices: A Review," *Appl. Phys. A*, 57 (1): 19-24, 1993.

[156] C. G. Granqvist and A. Hultåker, "Transparent and Conducting ITO Films: New

Developments and Applications," *Thin Solid Films*, 411 (1): 1-5, 2002.

[157] Y. Wang, W. P. Chen, K. C. Cheng, H. L. W. Chan, and C. L. Choy, "Effect of AC-Powered Water Electrolysis on the Structural and Optical Properties of Indium Tin Oxide Thin Films," *J. Am. Ceram. Soc.*, 88 (4): 1007–09, 2004.

[158] G. Knowles and S. Moncada, "Nitric Oxide as a Signal in Blood Vessels," *TIBS*, 17: 399-402, 1992.

[159] A. D. McGill, Y. Yang, J. Wang, L. Echegoyen, and P. G. Wang, "Redox-Sensitive Nitric Oxide Donors: Nitric Oxide Generation through Electrolysis," *Methods Enzymol.*, 301 (C): 235-42, 1999.

[160] C. M. Lo, C. R. Keese, and I. Giaever, "Monitoring motion of confluent cells in tissue culture," *Exp. Cell Res.*, 204 (1): 102-9, 1993.

[161] L. Charrier, Y. Yan, A. Driss, C. L. Laboisse, S. V. Sitaraman, and D. Merlin, "ADAM-15 Inhibits Wound Healing in Human Intestinal Epithelial Cell Monolayers," *Am. J. Physiol. Gastrointest Liver Physiol.*, 288: G346-353, 2005.

[162] N. K. Saxena, D. Sharma, X. Ding, S. Lin, F. Marra, D. Merline, and F. Anania, "Concomitant Activation of the JAK/STAT, P13K/AKT and ERK Signaling is Involved in Leptin-Mediated Promotion of Invasion and Migration of Hepatocellular Carcinoma Cells," *Cancer Res.*, 67 (6): 2497-507, 2007.

[163] C. R. Keese, J. Wegener, S. R. Walker, and I. Giaever, "Electrical Wound-Healing Assay for Cell *in Vitro*," *PNAS*, 101: 1554-59, 2004.